UNIVERSITY OF OKLAHOMA

GRADUATE COLLEGE

OBSERVING SYSTEM SIMULATION EXPERIMENT STUDIES ON THE USE OF SMALL UAV FOR BOUNDARY-LAYER SAMPLING

A THESIS

SUBMITTED TO THE GRADUATE FACULTY

in partial fulfillment of the requirements for the

Degree of

MASTER OF SCIENCE IN METEOROLOGY

By

ANDREW MOORE
Norman, Oklahoma
2018

OBSERVING SYSTEM SIMULATION EXPERIMENT STUDIES ON THE USE OF SMALL UAV FOR BOUNDARY-LAYER SAMPLING

A THESIS APPROVED FOR THE
SCHOOL OF METEOROLOGY

BY

_____
Dr. Frederick Carr, Chair

_____
Dr. Keith Brewster

_____
Dr. Phillip Chilson

© Copyright by ANDREW MOORE 2018

All Rights Reserved.

Acknowledgements

I first wish to thank my advisors Dr. Frederick Carr and Dr. Keith Brewster for their support both through the research process, allowing and encouraging me to pursue my professional goals, and working with me long distance. The work presented here would not have been possible without their assistance. Thanks are also given to Dr. Phillip Chilson for his expertise and guidance on the unmanned aerial systems described in this work and his enthusiasm for this research.

Additionally, I would like to extend gratitude to Dr. Ariel Cohen for his advice on numerical modeling, statistics, result interpretations, and continual encouragement.

Further thanks are given to my friends and family for their unwavering support through the research process.

Table of Contents

Acknowledgements……..iv

List of Tables……..viii

List of Figures……..ix

Abstract……..xix

Chapter 1……..1

1.1 Motivation……...1

1.2 Unmanned Aerial Vehicles (UAV) in Meteorology……...3

1.3 The University of Oklahoma CopterSonde and 3-D Mesonet……6

1.4 A Brief Review of Observing System Simulation Experiments (OSSEs).….7

Chapter 2……19

2.1 Numerical Modeling……..19

2.1.1 Advanced Regional Prediction System (ARPS)…….19

2.1.2 ARPS 3-Dimensional Variation System (ARPS3DVAR)….……19

2.1.3 ARPS Data Assimilation System (ADAS)…….21

2.1.4 Weather Research and Forecasting (WRF) Model…….23

2.1.5 WRF Data Assimilation Cycling……24

2.2 Simulated Observations…….26

2.2.1 Simulating Real Observing Networks…….……...26

2.2.2 Simulating 3-D Mesonet Observations……..31

Chapter 3……35

3.1 Case Study Selection…….35

3.2 Event Overview and Synoptic Setup…….35

3.3 ARPS Nature Run……..…40

3.4 Comparing the Nature Run to Reality……...41

3.5 WRF Control Run……..…48

3.6 Comparing the WRF Control and Nature Run……..…49

3.7 WRF OSSE Experiments……..50

3.8 Results……...54

3.8.1 Max Flight Altitude ……...54

3.8.1.1 Composite Reflectivity Comparison……...54

3.8.1.2 Surface RMSE Comparison……60

3.8.1.3 Vertical Profile Comparison……64

3.8.1.4 Cross Section Comparison……..67

3.8.1.4.1 Mixing Ratio Cross Sections……68

3.8.1.4.2 Equivalent Potential

Temperature Cross Sections…….……73

3.8.1.5 Convective Available Potential Energy Comparisons…76

3.8.2 Station Density ……..83

3.8.2.1 Composite Reflectivity Comparison……...…85

3.8.2.2 Surface RMSE Comparison……89

3.8.2.3 Vertical Profile Comparison……...90

3.8.2.4 Cross Section Comparison……..93

3.8.2.4.1 Mixing Ratio Cross Sections……93

3.8.2.4.2 Equivalent Potential

Temperature Cross Sections…….…97

3.8.2.5 Convective Available Potential Energy Comparisons..100

Chapter 4……..107

4.1 Summary and Conclusions……..107

4.1.1 Maximum Flight Altitude Summary……107

4.1.2 Network Density Summary……..109

4.1.3 General Conclusions…….…110

4.2 Future Work…….113

References……...……..116

Appendix……..….……126

List of Tables

Table 2.1: Correlation Length Scales used during the ADAS procedure……26

Table 2.2: Standard deviation values for Gaussian error distributions for each observation type……..….30

List of Figures

Figure 2.1: 110 3-D Mesonet simulated observation sites.....32

Figure 3.1: All severe weather reports from 20 May 2013 (SPC)……...…36

Figure 3.2: Surface objective analysis chart valid at 12 UTC 20 May 2013 (SPC)……37

Figure 3.3: Observed soundings from OUN at 12 UTC (A) and 17 UTC (B)……38

Figure 3.4: Observed surface dewpoints (fill, deg F) and 10 m wind vectors (barbs, knots) from the Oklahoma Mesonet valid at 17 UTC 20 May, 2013…….….39

Figure 3.5: Vertical levels of the ARPS (61 levels - black) and WRF (50 levels - red) models used in this study (A), and a closer look at distribution of model levels in the lowest 5 km (B)…….41

Figure 3.6: Comparison of the observed WSR-88D composite reflectivity radar mosaic (left) and the ARPS Nature Run composite reflectivity (right) at 12 UTC May 20, 2013…….....43

Figure 3.7: Comparison of the observed Oklahoma Mesonet dewpoint temperature (deg F, fill) and 10 m wind vectors (barbs, knots) (left) and the ARPS Nature Run 2 m dewpoint temperature (deg F, fill) and 10 m wind vectors (barbs, knots) (right) at 12 UTC May 20, 2013……43

Figure 3.8: Comparison of observed WSR-88D composite reflectivity mosaic (top) and ARPS Nature Run composite reflectivity (bottom) fields valid at 19 (A), 20 (B), and 21 (C) UTC 20 May 2013……44

Figure 3.9: Comparison of observed WSR-88D composite reflectivity mosaic (top) and ARPS Nature Run composite reflectivity (bottom) fields valid at 22 (A), 00 (B), and 02 (C) UTC on 20/21 May 2013 respectively……..45

Figure 3.10: Comparison between the 12 UTC observed sounding from Norman, OK (left) and the 12 UTC Norman sounding taken from the ARPS Nature Run (right)……...46

Figure 3.11: Comparison between the 12 UTC observed sounding from Norman, OK (left) and the 12 UTC Norman sounding taken from the ARPS Nature Run (right)……...48

Figure 3.12: Spatial coverage of the ARPS domain (black) and WRF domain (blue)...49

Figure 3.13: Comparison between modeled composite radar reflectivity in the Nature Run (top) and the WRF Control (bottom). Images are valid at 19 UTC (A) and 22 UTC (B) on 20 May, 2013…….50

Figure 3.14: RMSE values between 12 UTC 20 May 2013 to 06 UTC 21 May 2013 from the WRF Control run……..……51

Figure 3.15: A graphical interpretation of the UAV OSSE system……...52

Figure 3.16: Comparison between modeled composite radar reflectivity between the Nature Run (A), WRF Control (B), No UAV (C), UAV 400ft (D), UAV 1km (E), UAV 2km (F), and UAV 3km (G) at 1800 on 20 May 2013……...55

Figure 3.17: Comparison between modeled composite radar reflectivity between the Nature Run (A), WRF Control (B), No UAV (C), UAV 400ft (D), UAV 1km (E), UAV 2km (F), and UAV 3km (G) at 1830 on 20 May 2013……...56

Figure 3.18: Comparison between modeled composite radar reflectivity between the Nature Run (A), WRF Control (B), No UAV (C), UAV 400ft (D), UAV 1km (E), UAV 2km (F), and UAV 3km (G) at 1900 on 20 May 2013……...56

Figure 3.19: Comparison between modeled composite radar reflectivity between the Nature Run (A), WRF Control (B), No UAV (C), UAV 400ft (D), UAV 1km (E), UAV 2km (F), and UAV 3km (G) at 1930 on 20 May 2013……...57

Figure 3.20: Comparison between modeled composite radar reflectivity between the Nature Run (A), WRF Control (B), No UAV (C), UAV 400ft (D), UAV 1km (E), UAV 2km (F), and UAV 3km (G) at 2000 on 20 May 2013……...57

Figure 3.21: Comparison between modeled composite radar reflectivity between the Nature Run (A), WRF Control (B), No UAV (C), UAV 400ft (D), UAV 1km (E), UAV 2km (F), and UAV 3km (G) at 2030 on 20 May 2013……...58

Figure 3.22: Comparison between modeled composite radar reflectivity between the Nature Run (A), WRF Control (B), No UAV (C), UAV 400ft (D), UAV 1km (E), UAV 2km (F), and UAV 3km (G) at 2100 on 20 May 2013……...58

Figure 3.23: RMSE plots during the data assimilation cycling period (left of the vertical black line) and during the free forecast period (right of the black line) for surface pressure (upper left), 10 m U and V winds (upper right), 2 m mixing ratio (bottom left), and 2 m temperature (bottom right)……..62

Figure 3.24: Mean Sea Level Pressure (MSLP) comparisons between the Nature Run (A), WRF Control (B), No UAV (C), UAV 400ft (D), UAV 1km (E), UAV 2km (F), and UAV 3km (G) forecasts at 1800 UTC……...63

Figure 3.25: Vertical profiles below 500 hPa of dewpoint (upper left), temperature (upper right), wind direction (bottom left), and wind speed (bottom right) valid at the analysis time of 1800 UTC……65

Figure 3.26: Vertical analysis error profiles below 500 hPa valid at 1800 UTC for the Maximum Flight Altitude tests……66

Figure 3.27: The black line shown here on the WRF domain represents the sampling location for the cross-section analyses……68

Figure 3.28: Cross section plots of mixing ratio from 0 to 4 km above MSL for the Nature Run (A), WRF Control (B), No UAV (C), UAV 400ft (D), UAV 1km (E), UAV 2km (F), and UAV 3km (G) WRF analyses valid at 1800 UTC 20 May 201……...70

Figure 3.29: As in figure 20, except cross sections are valid at 1900 UTC……..…70

Figure 3.30: As in figure 20, except cross sections are valid at 2000 UTC……..…71

Figure 3.31: 1800 UTC analysis of 2m dewpoint for the Nature Run (A), WRF Control (B), No UAV (C), UAV 400ft (D), UAV 1km (E), UAV 2km (F), and UAV 3km (G)……...72

Figure 3.32: One hour 2m dewpoint forecast valid at 1900 UTC for the Nature Run (A), WRF Control (B), No UAV (C), UAV 400ft (D), UAV 1km (E), UAV 2km (F), and UAV 3km (G) forecasts……....73

Figure 3.33: Cross section plots of theta-e from 0 to 4 km above MSL for the Nature Run (A), WRF Control (B), No UAV (C), UAV 400ft (D), UAV 1km (E), UAV 2km (F), and UAV 3km (G) WRF analyses valid at 1800 UTC 20 May 2013……..74

Figure 3.34: As in figure 25 except representing a one hour forecast of theta-e cross section valid at 1900 UTC 20 May 2013……74

Figure 3.35: As in figure 25 except representing a two-hour forecast of theta-e cross section valid at 2000 UTC 20 May 2013……75

Figure 3.36: 1800 UTC analysis MUCAPE (fill) and MUCIN (contours) for the Nature Run (A), WRF Control (B), No UAV (C), UAV 400ft (D), UAV 1km (E), UAV 2km (F), and UAV 3km (G) model runs…….79

Figure 3.37: One hour forecast for MUCAPE (fill) and MUCIN (contours) for the Nature Run (A), WRF Control (B), No UAV (C), UAV 400ft (D), UAV 1km (E), UAV 2km (F), and UAV 3km (G) model runs valid at 1900 UTC…….79

Figure 3.38: Two hour forecast for MUCAPE (fill) and MUCIN (contours) for the Nature Run (A), WRF Control (B), No UAV (C), UAV 400ft (D), UAV 1km (E), UAV 2km (F), and UAV 3km (G) model runs valid at 2000 UTC…….80

Figure 3.39: 1800 UTC analysis MLCAPE (fill) and MLCIN (contours) for the Nature Run (A), WRF Control (B), No UAV (C), UAV 400ft (D), UAV 1km (E), UAV 2km (F), and UAV 3km (G) model runs…….80

Figure 3.40: One hour forecast for MLCAPE (fill) and MLCIN (contours)for the Nature Run (A), WRF Control (B), No UAV (C), UAV 400ft (D), UAV 1km (E), UAV 2km (F), and UAV 3km (G) model runs valid at 1900 UTC……..81

Figure 3.41: Two hour forecast for MLCAPE (fill) and MLCIN (contours)for the Nature Run (A), WRF Control (B), No UAV (C), UAV 400ft (D), UAV 1km (E), UAV 2km (F), and UAV 3km (G) model runs valid at 2000 UTC…….81

Figure 3.42: Four 3-D Mesonet configurations with varying station densities……...82

Figure 3.43: Composite Reflectivity forecast from the Nature Run (A) and WRF Control (B) and analysis fields from the No UAV (C), 110 Station (D), 75 Station (E), 50 Station (F), 25 Station (G), and 10 Station (H) experiments valid at 1800 UTC……86

Figure 3.44: Composite Reflectivity forecasts from the Nature Run (A), WRF Control (B), No UAV (C), 110 Station (D), 75 Station (E), 50 Station (F), 25 Station (G), and 10 Station (H) experiments valid at 1830 UTC……86

Figure 3.45: Composite Reflectivity forecasts from the Nature Run (A), WRF Control (B), No UAV (C), 110 Station (D), 75 Station (E), 50 Station (F), 25 Station (G), and 10 Station (H) experiments valid at 1900 UTC……87

Figure 3.46: Composite Reflectivity forecasts from the Nature Run (A), WRF Control (B), No UAV (C), 110 Station (D), 75 Station (E), 50 Station (F), 25 Station (G), and 10 Station (H) experiments valid at 1930 UTC……87

Figure 3.47: Composite Reflectivity forecasts from the Nature Run (A), WRF Control (B), No UAV (C), 110 Station (D), 75 Station (E), 50 Station (F), 25 Station (G), and 10 Station (H) experiments valid at 2000 UTC……88

Figure 3.48: RMSE plots during the data assimilation cycling period (left of the vertical black line) and during the free forecast period (right of the black line) for surface pressure (upper left), 10 m U and V winds (upper right), 2 m mixing ratio (bottom left), and 2 m temperature (bottom right)……..89

Figure 3.49: Vertical profiles of dewpoint (upper left), temperature (upper right), wind direction (bottom left), and wind speed (bottom right) analyses valid at 1800 UTC…….91

Figure 3.50: Vertical profiles of dewpoint (upper left), temperature (upper right), wind direction (bottom left), and wind speed (bottom right) analyses errors valid at 1800 UTC……92

Figure 3.51: 1800 UTC analysis mixing ratio cross sections from 0 to 4 km above MSL for the Nature Run (A), WRF Control (B), No UAV (C), 110 stations (D), 75 stations (E), 50 stations (F), 25 stations (G), and 10 stations (H)……..95

Figure 3.52: 1900 UTC forecast for mixing ratio cross from 0 to 4 km above MSL sections for the Nature Run (A), WRF Control (B), No UAV (C), 110 stations (D), 75 stations (E), 50 stations (F), 25 stations (G), and 10 stations (H)……..95

Figure 3.53: 2000 UTC forecast for mixing ratio cross sections from 0 to 4 km above MSL for the Nature Run (A), WRF Control (B), No UAV (C), 110 stations (D), 75 stations (E), 50 stations (F), 25 stations (G), and 10 stations (H)……..96

Figure 3.54: 925 hPa Dewpoint forecast and analysis for the Nature Run (left) and 10-station UAV test (right) respectively valid at 1800 UTC……96

Figure 3.55: Comparison of the Nature Run (black) and simulated UAV (green) dewpoint profiles sampled at 1800 UTC at the Waurika, OK (WAUR) Mesonet site……97

Figure 3.56: 1800 UTC analysis theta-e cross sections from 0 to 4 km above MSL the Nature Run (A), WRF Control (B), No UAV (C), 110 stations (D), 75 stations (E), 50 stations (F), 25 stations (G), and 10 stations (H)……98

Figure 3.57: 1900 UTC forecast theta-e cross sections from 0 to 4 km above MSL for the Nature Run (A), WRF Control (B), No UAV (C), 110 stations (D), 75 stations (E), 50 stations (F), 25 stations (G), and 10 stations (H)……98

Figure 3.58: 2000 UTC forecast theta-e cross sections from 0 to 4 km above MSL for the Nature Run (A), WRF Control (B), No UAV (C), 110 stations (D), 75 stations (E), 50 stations (F), 25 stations (G), and 10 stations (H)……99

Figure 3.59: 1800 UTC analysis of MUCAPE (fill) and MUCIN (contours) for the Nature Run (A), WRF Control (B), No UAV (C), 110 stations (D), 75 stations (E), 50 stations (F), 25 stations (G), and 10 stations (H)……...101

Figure 3.60: 1900 UTC forecast of MUCAPE (fill) and MUCIN (contours) for the Nature Run (A), WRF Control (B), No UAV (C), 110 stations (D), 75 stations (E), 50 stations (F), 25 stations (G), and 10 stations (H)…….....101

Figure 3.61: 2000 UTC forecast of MUCAPE (fill) and MUCIN (contours) for the Nature Run (A), WRF Control (B), No UAV (C), 110 stations (D), 75 stations (E), 50 stations (F), 25 stations (G), and 10 stations (H)……...102

Figure 3.62: 1800 UTC analysis of MLCAPE (fill) and MULIN (contours) for the Nature Run (A), WRF Control (B), No UAV (C), 110 stations (D), 75 stations (E), 50 stations (F), 25 stations (G), and 10 stations (H)...……102

Figure 3.63: 1900 UTC forecast of MLCAPE (fill) and MULIN (contours) for the Nature Run (A), WRF Control (B), No UAV (C), 110 stations (D), 75 stations (E), 50 stations (F), 25 stations (G), and 10 stations (H)……...103

Figure 3.64: 2000 UTC forecast of MLCAPE (fill) and MULIN (contours) for the Nature Run (A), WRF Control (B), No UAV (C), 110 stations (D), 75 stations (E), 50 stations (F), 25 stations (G), and 10 stations (H)……...103

Figure A.1: Mean bias plots during the data assimilation cycling period (left of the vertical black line) and during the free forecast period (right of the black line) for surface pressure (upper left), 10 m U and V winds (upper right), 2 m mixing ratio (bottom left), and 2 m temperature (bottom right)……126

Figure A.2: Mean bias plots during the data assimilation cycling period (left of the vertical black line) and during the free forecast period (right of the black line) for surface pressure (upper left), 10 m U and V winds (upper right), 2 m mixing ratio (bottom left), and 2 m temperature (bottom right)……127

Abstract

A long-desired component to the U.S. operational observing systems is the capability to measure vertical profiles of wind, temperature and moisture in the lower troposphere at high spatial and temporal resolution. This study proposes that such profiling could be done by small unmanned aerial vehicles (UAVs) assuming that autonomous flights at least through the depth of the boundary layer be permitted. Since we do not yet have FAA permission to test such an observing network, we examine the potential improvement that a UAV network could have on storm-scale numerical weather prediction using an Observation System Simulation Experiment (OSSE) approach.

An OSSE is performed over the state of Oklahoma in which we assume that a UAV could be launched from 110 Oklahoma Mesonet stations every hour, fly vertically to an assigned maximum altitude and return to its charging station, providing soundings at a roughly 35 km horizontal resolution. We begin with a case study of convective initiation (CI) as a compromise between a fair weather day and one with extensive ongoing convection. The OU ARPS model provides a nature run at high (1 km) resolution, while the control run and OSSE experiments are done with the WRF-ARW model at 3 km. To simulate the effect of data from dozens of observing systems already included in operational models, the nature run data volume is sampled at synoptic scales and inserted into the control run via a 6-hr data assimilation (DA) period. Simulated hourly UAV temperature, moisture and wind data, with expected errors, are then added to the DA, followed by 12-hr forecasts. The analyses and forecasts are examined to assess

the added value of UAV data. Tests are run to measure the impact of varying the maximum UAV altitude and the spatial density of UAV observations.

Initial results clearly show an improved boundary layer structure and subsequent CI location and timing when UAV data are added to the control experiment. Additionally, early findings indicate flight altitude and network density can play a role in the quality of the DA analysis and subsequent forecast of convective initiation. Although sensitivities to the quality of the moisture analysis are noted, the results here suggest that a real-world deployment of automated UAVs could have a positive impact on atmospheric analyses and short-term numerical weather prediction.

Chapter 1

1.1 Motivation

In their 2009 study *Observing Weather and Climate from the Ground Up: A Nationwide Network of Networks*, the National Research Council (NRC) discussed many of the ongoing challenges associated with atmospheric sensing, data collection, and data dissemination. The NRC proposed a "nationwide network of networks" (NNON) to increase and standardize lower-tropospheric data (NRC, 2009). Through this work, the NRC recommended improvements to augment current observing networks that could potentially lead to improvements in numerical weather prediction (NWP). A related recommendation is the need for mesoscale models to perform observing system experiments (OSEs) as well as observing system simulation experiments (OSSEs) to assess the value of adding new observing systems to the current networks (NRC, 2009). Through this, current observing networks could effectively become testbeds with the goal of identifying weak points in current observing strategies and finding optimal network configurations for available resources.

The NRC also reported that one of the most prominent regions of the atmosphere that requires improved sampling is the planetary boundary layer (PBL). In a 2013 article, Stalker et al. succinctly summarized this need for better sampling of the boundary layer by stating that existing observing networks severely lack the horizontal and vertical resolution to study and predict mesoscale processes, especially pertaining to profiles of the PBL.

Dabberdt et al. (2005) also discuss the need for high-frequency spatial and temporal sampling of the PBL, especially when forecasting convective weather. Even with the availability of convection allowing numerical weather prediction models, the lack of PBL observations assimilated into numerical simulations may diminish the value of convective forecasts. Dabberdt et al. (2005) argue that a PBL profiling network could convey information about the low-level environment, such as the strength of a capping inversion, into numerical models that could lead to improved forecasts. Furthermore, even aside from numerical modeling considerations, frequent thermodynamic and kinematic profiles observed within the PBL could be valuable for convective now-casting and allow for forecasters to deliver more timely and accurate warnings.

Currently, there are very few operational networks in place that can accurately observe processes in the PBL. The most well-known of these networks is the global radiosonde network. While this network undoubtedly provides valuable in-situ observations for both forecasters and NWP, radiosondes generally are released only twice daily with a very coarse spatial coverage. Additionally, radiosondes have uncontrolled ascent rates and are designed primarily to obtain a full atmospheric profile within a reasonable flight time to support forecast operations, not to take high resolution observations of the PBL. While there are other instruments capable of such high resolution PBL observations, such as Doppler Light Detection and Ranging (LiDAR) instruments and Atmospheric Emitted Radiance Interferometers (AERI) (Geerts et al. 2017)), these are primarily used for research rather than operational purposes. Additional observing networks, such as the National Weather Service's Weather Surveillance Radar 88 Doppler (WSR-88D) radars and their limitations in sampling the PBL are highlighted

by Dabberdt et al. 2005. They conclude that the biggest gap in our current in-situ observing network are temperature and moisture measurements in the PBL.

1.2 Unmanned Aerial Vehicles in Meteorology

It is proposed that unmanned aerial vehicles (UAVs) are a viable option to fill the sampling void within the PBL. The Collaboration Leading Operation UAS Development for Meteorology and Atmospheric Physics (CLOUD-MAP) initiative (Smith et al. 2017) was designed for this purpose. The goal of the project is to develop UAV technologies that can autonomously sample the PBL. Not only does this multi-university collaborative initiative promote the development of the UAV technologies, but also promotes the development of public policy that will allow UAVs to use additional airspace for atmospheric research and operational data sampling.

CLOUD-MAP is not the first initiative that has employed UAVs for PBL measurements. Bonin et al. (2013a) conducted an in-depth study of the early evening transition using temperature, humidity, and pressure profiles collected by the Small Multifunction Research and Teaching Sonde (SMARTSonde) that was developed at the University of Oklahoma (OU) Advanced Radar Research Center (ARRC). Estimates of sensible and latent heat fluxes were determined from the data collected by the SMARTSonde, giving an analysis of the evolution of the PBL during the early evening transition. The SMARTSonde was also used to test various GPS based methods for retrievals of the PBL wind profile (Bonin et al. 2013b). Wind retrievals gathered by the UAV were compared to retrievals collected by a nearby SoDAR (Sonic Detection and Ranging) and radiosonde releases and found to compare well to the other platforms, sampling the wind speed to within 1.25 ms^{-1} and direction within 16˚ of those determined

from the radiosonde. Additionally, Wainwright et al. used UAVs to collect high-frequency temperature observations within the boundary layer in order to develop methods for determining turbulent temperature fluctuations. The data collected by the UAV were found to adequately represent the boundary layer when compared to a co-located SoDAR, further demonstrating the value of UAV as a research instrument.

Further studies focused on using UAV in boundary layer measurements include the 2012 work of Dias et al. (2012) who adapted a small commercial UAV with a meteorological instruments package to take high resolution measurements of boundary layer virtual temperature and entrainment fluxes.

Typically, UAVs fall into one of two categories. Larger aircraft over 10 kg are considered Category I UAVs and are typically designed for longer duration, higher flight missions. These craft can carry a wide array of sensors and normally need a runway for takeoff and landing. However, such aircraft can become expensive to operate and equip (Elston et al. 2015). One example of a Category I UAV is the Aerosonde research UAV, which is capable of flight up to 6 km with a flight duration of 40 hours (Dias et al. 2012). Smaller, Category II UAVs are under 10 kg in mass, carry lighter payloads, have lower operating altitudes, and remain airborne for under an hour. Similar to the SMARTSonde, Dias et al. used a fixed-wing Category II UAV that was able to take measurements up to 1800 meters during a 15-minute flight. Despite their small size and limited flight capability, the relatively low price and ease of use make Category II aircraft popular among many research groups such as Dias et al. (2012), Bonin et al (2013a/b), and the CLOUD-MAP initiative (Elston et al. 2015).

Fixed-wing aircraft are not the only type of UAV that have been tested and used for PBL sampling and meteorological studies. Zhang, Dong, and Liu (2017) demonstrated how a six-rotor helicopter UAV, commonly known as a copter UAV, could be used for PBL measurements as an alternative to traditional towers, balloons, and radiosondes. One concern pertaining to copter UAVs is the impacts of rotor wash on instruments, especially pressure and temperature measurements. However, studies have quantified these errors and found them to be generally small (Guest, 2014) and can be mitigated by proper placement on the airframe. The work presented here focuses around these Category II copter UAVs.

UAVs have served other roles in meteorological applications as well. Duthoit et al. 2017 demonstrated the ability of UAV technology to assist in radar maintenance. Here rotor UAVs were used to inspect radome surfaces and help perform calibration of an X-band radar. The SMARTSonde developed at the ARRC has also been used to validate refractivity retrievals used by weather radars as described in Chilson et al. 2009. A review by Villa et al. (2016) validated the use of UAV for air quality studies, through several concerns were noted pertaining to future use of UAVs for such studies. These concerns included flight duration and payload capabilities as well as differing international regulations hindering the use of UAVs as a global research tool.

In the United States, Federal Aviation Agency (FAA) regulations prohibit any non-hobbyist UAV flights over 400 feet above ground level without a Certificate of Authorization (COA) as outlined in the FAA Memorandum AFS-400 [4] (FAA 2005) and recent rules for non-recreational UAV flight (FAA Small UAS Rule 14 CFR part 107, 2016). While hobbyists are free to fly any UAV under this ceiling restriction, state

and federal agencies must acquire a COA by the FAA before UAV flights at any altitude can take place. This restriction typically encompasses university research groups and is a hinderance to UAV research as acquiring COA can be a lengthy process. However, one work around to this regulation is to tether the UAV, which allows research groups to legally fly UAVs above 400 feet (Walker and Miller 2013). However, using tethered UAVs may not be ideal is all research applications that employ UAV technology. Despite these regulations, many groups, such as CLOUD-MAP, see UAV as the future of PBL sampling and research.

1.3 The University of Oklahoma CopterSonde and 3-D Mesonet

The OU Center for Autonomous Sensing Systems (CASS) has begun work on a new UAV designed for intensive sampling of the PBL. Initially designed for flight and instrument testing during the National Severe Storms Laboratory (NSSL) Environmental Profile and Initiation of Convection (EPIC) field project in fall 2016 (Koch et al. 2017), this aircraft, designated the CopterSonde, is a “hashtag” shaped, eight-rotor Pixhawk copter UAV that can carry an array of meteorological instruments. Equipped with the ArduPilot (APM) software, the CopterSonde can fly in manual or autopilot mode. An integrated inertial measurement unit (IMU) and differential global positioning system (GPS) allow the CopterSonde to maintain a positional accuracy of 2-8 cm in flight. The CopterSonde is designed with operational safety in mind such that in the event of a single propeller or motor failure, the UAV will maintain safe and stable flight. Since the CopterSonde is designed for the purpose of PBL measurements it is able to operate in wind speeds up to 25 ms^{-1} (approximately 50 knots). This capability was tested during

EPIC when the CopterSonde "performed exceptionally well" during flights that experienced wind gusts over 20 ms^{-1} (approximately 40 knots) (Koch et al. 2017). However, variations of the CopterSonde frame and motor configurations are being considered and tested after experience and data collected during the EPIC campaign.

The meteorological sensor package currently under testing on the CopterSonde is the Intermet Systems iMet-XF atmospheric sensor package. This instrument package is designed for rotary UAV platforms and contains a fast response bead thermistors for temperature and the IST hygrometer for relative humidity. The fast response thermistor has a 0.3 C precision and time constant of about 1 second. Both the thermistor and hygrometer have a sampling frequency of 5 – 10 Hz (Intermet Systems).

The CopterSonde has become the leading UAV candidate as the instrumentation package for a concept of operations known as the 3-D Mesonet, an observing network concept that employs UAVs to sample in situ-observations of the PBL on a spatial scale similar to current mesoscale surface observing networks. While the CopterSonde UAV is the observing platform for the 3-D Mesonet, it is not the only required component. Work is underway at CASS to develop an automated recharging station for the UAV as well as a system for remotely inspecting the condition of the CopterSonde prior to flight. Since the UAV will be sharing airspace with regional air traffic, a small radar system is being designed that will detect nearby aircraft and notify the CopterSonde of the approaching air traffic. The UAV will then be able to terminate its observation flight prematurely with a rapid descent back to the recharging station. This ensures that the 3-D Mesonet will not interfere with the safety and operation of regional air space. As an additional safety

measure, 3-D Mesonet sites will not be co-located with airports of any size due to the low operating altitudes of aircraft on approach or takeoff.

1.4 A Brief Review of Observation System Simulation Experiments

Observing System Simulation Experiments (OSSEs) are a set of numerical experiments designed to gauge the potential impacts new observing systems have on numerical weather prediction. In an OSSE, one atmospheric numerical model is assumed to represent the actual behavior of the atmosphere. This modeled atmosphere, often referred to as the Nature atmosphere, or the Nature Run, is then sampled in such a way as to mimic a real or proposed observing systems, the data from which are then used to perform a series of experiments to determine the usefulness of the observing networks (AMS Glossary). The opening paragraphs of Masutani et al. (2010) describe the benefits of OSSEs, noting that by performing an OSSE for the then-proposed National Polar-orbiting Environmental Satellite System (NPOESS) the instrumentation, modelling, and data assimilation communities will all be able to contribute to the design and specifications of the instrument package. This collaboration expedites the development process, mitigates long term costs, and maximizes the potential impact on numerical weather prediction. Despite the potential shortcomings of the OSSE methodology, such as the identical twin problem and misrepresented system capabilities and error assumptions (discussed later), the ability to experiment with simulated data from a proposed observing network prior to any instrument deployment is the true strength of an OSSE.

As described in Hoffman et al. (1990), OSSEs have three main components: 1) a long integrated, high resolution numerical model that represents the true atmosphere, often called the “Nature Run”. 2) A method for obtaining simulated observations for both operational observing systems and the proposed observing systems from the Nature Run. 3) A series of analyses and forecast experiments to gauge the impact of the new observing system. In addition, many OSSEs incorporate a calibration step to ensure that the results are realistic. Typically, this calibration step involves performing an OSSE with an observing system that is already in place in order to compare the impacts of the real system with those of the simulated system. A second run is made using real instead of simulated observations; i.e., an observing system experiment (OSE). If the two impacts are similar, it provides confidence that the results from an OSSE will fairly estimate the actual benefit of the new observing system. Although somewhat similar in experimental design, the fundamental difference between OSSEs and OSEs is that OSE typically consist of data denial tests of observing systems that already exist and are fully operational. Additionally, OSEs compare their results to the real atmosphere while OSSE use the Nature Run atmosphere for measuring the impact of observations on the forecast accuracy.

The history of OSSEs begins in the mid-1950s when Newton (1954) discussed the potential benefits of performing numerical experiments with simulated data. It was thought that these experiments could highlight optimal locations for new instruments or observing networks, the required accuracy of those observations, and the best way to assimilate the observations to give the best results in an objective analysis. These ideas were expanded upon by Bristor (1958) who constructed a “perfect” geopotential height

field and added random perturbations to represent a measured atmosphere. From this data set Bristor then simulated various observation network configurations and compared the forecast results from the different simulated networks to the forecast from the "true" atmosphere. Bristor's study was the first employ the OSSE methodology that has since been used in numerous studies.

In 1967 the Global Atmospheric Research Program (GARP) was initiated with one of the main objectives focusing on satellite data requirements for skillful NWP. This initiative prompted several OSSE efforts, including the work of Charney et al. (1969). The goal of Charney et al. was to demonstrate the value of analyzing temperature observations from the proposed Nimbus 3 satellite to yield other useful meteorological variables such as wind velocity. During this time, most of the observational data used by NWP came from rawinsonde data observed twice daily and surface data. This observing network left much of the mid and upper atmosphere relatively under sampled, especially if wind speeds were too high to accurately track weather balloons, and in the tropics where the number of surface and rawinsonde stations was sparse. The use of meteorological satellites was still in its infancy, and this work laid the foundation for further OSSEs to demonstrate the usefulness of proposed satellites for the next several decades. Following just a year later Halem and Jastrow (1970) used methods similar to Charney et al. to calculate the allowable root mean squared (RMS) observation errors for temperature, wind, and pressure in order to find the limits of predictability at various forecast times. Their findings revealed that the errors that were allowed under the GARP requirements for wind and pressure measurements would degrade an objective analysis despite having

higher quality temperature measurements. This finding was significant in that numerical modeling was able to identify a weakness in a proposed observing system.

In the early days of OSSEs, including the work of Charney et al. (1969) and Halem and Jastrow (1970), the same model that was used to create the Nature Run was also used to create the OSSE forecast experiments. This type of experimental design was known as an "identical twin" OSSE (Atlas 1997). However, it was soon discovered by Williamson and Kasahara (1971) that due to the similarity in model errors between the Nature Run and the experiment forecasts that OSSE results were typically over-optimistic. Further limitations of identical twin OSSEs were identified by Jastrow and Halem (1973) who argued that even different model physical parameterizations were not sufficiently different when compared to the differences between real-world physical processes and model physics. Additionally, they found that incorrect assumptions about the capabilities of the observing system would yield optimistic results. Williamson (1973) went further to show that the only source of forecast error between the Nature Run and forecast experiments resulted from differences in the initial conditions of the two model runs in identical twin OSSEs.

In order to avoid the identical twin problem Williamson and Kasahara (1971) suggested using a different model for the forecast experiments than is used to create the Nature Run. The model used for the forecast experiments is typically of lower resolution and employs different physical parameterizations than the nature run. This allows the model differences between the experiments and Nature Run to mirror the differences between a "state of the art" forecast model and the true atmosphere (Atlas 1997). These types of OSSEs are commonly referred to as "fraternal twin" OSSEs.

After the GARP experiment, the number of studies focused on OSSEs decreased until the 1980s when work was done by Cane et al. (1981) to find the impact on NWP of marine surface wind observations as simulated from a satellite. One notable finding from this study was the suggestion of allowing five days of model integration in an identical twin experiment in order for forecast statistics to be sufficiently different to be considered independent. However, since the authors performed an identical twin OSSE many following studies were skeptical of this result (Arnold and Dey 1986).

In 1983, prior to the launch of the Doppler wind LiDAR sounding system satellite program (WINDSAT), the National Meteorological Center (NMC), Goddard Laboratory for Atmospheric Sciences (GLAS), and the European Centre for Medium Range Weather Forecasts (ECMWF) collaborated to define guidelines for performing and interpreting OSSEs. Efforts were made to create a Nature Run that could be collaboratively used for WINDSAT related OSSEs. The ECMWF was chosen to create a single 20-day Nature Run, allowing the other agencies to run fraternal-twin simulations with their own models (Arnold and Dey 1986).

Several notable papers resulted from this collaboration on the WINDSAT project, the first was Atlas et al. (1984), which was the first study to suggest the need for calibration of OSSE results with a corresponding OSE. Atlas et al. also reinforced the need for fraternal twin OSSEs in order to avoid unrealistically positive results. Along with testing model response times to various simulated observations, Halem and Dlouhy (1984) compared identical twin and fraternal twin experiments. They found that, contrary to previous studies, the identical and fraternal twin experiments gave similar results. However, the study is regarded as highly idealized bringing the validity of the study's

results into question (Atlas et al. 1985, Arnold and Dey 1986). A more complete, fraternal-twin OSSE was conducted as a companion experiment to Halem and Dlouhy (1984) where wind fields from a space-based LiDAR were simulated with multiple realistic sources of error, including the effects of clouds and atmospheric aerosols on LiDAR observations (Halem and Dlouhy 1984).

Studies on the WINDSAT project continued into the late 1980s. One such study is Hoffman et al. 1990 where investigators simulated the potential impacts of wind, temperature and moisture retrievals on global numerical prediction. The investigation revealed that while there was a net positive effect on global forecasts, the main impacts were found in the Southern Hemisphere where RMS error in the moisture field was decreased by 5% and the 500 hPa height forecast was improved by 12 hours. A calibration OSE was performed and verified that while the instrument would likely have little impact in the Northern Hemisphere, the positive results found in the Southern Hemisphere were realistic, giving high confidence to the findings.

By the early to mid-1990s OSSE work was focused primarily on the proposed Laser Atmospheric Wind Sounder (LAWS) and the NASA Scatterometer (NSCAT). For these OSSEs a more accurate Nature Run with higher resolution was developed by ECMWF (Atlas 1997). Rohaly and Krishnamurti (1993) investigated the impacts of assimilating simulated LAWS observations from two different orbital inclinations. As might be expected, they found that the orbit with the higher inclination were able to resolve features in the polar regions while the lower inclined orbit accurately resolved the tropics. Besides these differences the overall impacts of the LAWS observations were similar for both orbits. Woods et al. (1991) and Emmitt and Woods (1991) simulated

LAWS observations to demonstrate the potential impacts of cirrus clouds, water vapor, and other aerosols on wind vector estimates and forecasts. Hoffman (1993) performed experiments with NASA's ERS-1 Scatterometer and found that the simulated observations had little to no impact on forecasts in the Northern Hemisphere, and only slightly positive impacts on the Southern Hemisphere.

Although work on global satellite OSSEs continued into the early 2000s (Lord et al. 2001), a number of OSSEs focusing on mesoscale observing networks and assimilation techniques emerged. One such study is Tong and Xue 2004 where a new Ensemble Kalman Filter (EnKF) data assimilation method is employed to assimilate radar observations into storm scale atmospheric simulations. More specifically, the study sought to observe the impacts on the analysis of a supercell storm by assimilating different classes of microphysical variables as well as the effects of incorporating reflectivity and radial velocity. It was found that the EnKF radar assimilation method performed well to recreate the model supercell storm after a number of assimilation cycles. While no extended forecasts were made, nor any calibration performed, this study laid the foundation for future radar OSSEs.

Similar methods to Tong and Xue 2004 were employed in Xue et al. 2005, which focused on the impacts of assimilating CASA (Center for Collaborative Adaptive Sensing of the Atmosphere) radar observations of supercells into regional numerical models. The smaller X-band CASA radars were tested as gap filling radars to sense the lower atmosphere and lowest portions of severe storms - regions that are not well covered by the operational WSR-88D network. Emphasis was placed on using a new Ensemble Square Root Kalman Filter (EnSRF) radar assimilation method to realistically simulate

and assimilate data from the smaller, faster CASA radars. It was found that the CASA radars did add noticeable value to the analysis in the lowest levels of the atmosphere, and the improvements to the analysis increased as more simulated CASA radars were assimilated. Although this study paid great detail to incorporating realistic errors in the data assimilation stage, no calibration step was performed. This was likely due to the limited number of observational networks that the proposed CASA network could be compared against.

The use of OSSEs for testing new data assimilation methods continued with the work of Wang et al. 2008 and Liu et al. 2009 who used the WRF-ARW model to perform data assimilation tests with hybrid ETKF-3DVAR and En4DVAR schemes respectively. While satellite and global NWP OSSE work was still carried out into the 2010s (Masutani et al. 2010, Atlas et al. 2015, Jones et al. 2013, Bruscantini et al. 2012), more studies emerged focusing on surface-based observing systems (Yussouf and Stensrud 2010, Gasperoni et al. 2012, Hartung et al. 2011). This period of OSSE work not only demonstrates the versatility of OSSEs, but also marks the transition from larger, planetary observing systems on large spatio-temporal scales to testing a variety of smaller observing systems and data handling methods on smaller spatio-temporal scales. These smaller, shorter OSSEs are now commonly referred to as “quick OSSEs”.

Quick OSSEs were mentioned by Atlas et al. 2015 as a valid method for testing impacts of observations systems on modeling smaller scale events such as hurricanes. These quick OSSEs are typically performed over a ten-day period and have Nature Runs that were created by regional models embedded within global Nature Runs. This more rigorous Nature Run suggestion allows for the discernment between the impacts of

regional vs. global data assimilation procedures (Zhang et al. 2010). Although this suggestion is followed by many OSSE studies (Nolan 2013, Miller et al. 2008), it is not a requirement for a complete OSSE. Some studies have created their own Nature Runs with lone regional models, such as Aksoy et al. 2012 and Leidner et al. 2016.

In the Leidner et al. study, observations from Global Navigation Satellite System (GNSS) Radio Occultations (ROs) are simulated for a quick OSSE (Atlas 2015) for the May 31, 2013 severe weather event. This study is unique in that it combines simulated satellite observations with smaller spatial and temporal scales. The inner domains covered by both the Nature Run and the experiment forecasts were both on the mesoscale and were run for only a 30-hour forecast in order to capture the entirety of the severe weather event. Although the authors acknowledged the weaknesses in their experimental design, such as using the WRF for both the Nature Run and forecast experiments, this study of a single severe weather event is still substantiated as a valid application of the quick OSSE methodology.

Another relevant quick OSSE is Zack et al. (2011). In this study a quick OSSE is conducted to find the optimal configuration of meteorological towers and SoDAR instruments in the Mid-Columbia River Valley that provide the most accurate wind forecasts for wind energy purposes. Zack et al. performed a fraternal-twin OSSE, employing the Advanced Regional Prediction System (ARPS) (Xue et al. 2000, Xue et al. 2001) to produce a high resolution (1 km) 9-day long Nature Run and using the WRF-ARW to produce the experiments. In order to simulate the high-resolution SoDAR observations, wind speed data were vertically interpolated every 10 meters from 30-200 meters above ground level (AGL). Meteorological tower, radiosonde, and surface

observation networks were also simulated in a similar manner based on errors associated with each observation type. In order to help decrease the similarities between the nature run and the experiments, all experiments were initialized at an earlier time than the Nature Run. This allowed for model error to grow enough that once the Nature run and experiment forecast were valid at the same time there were substantial differences between the two. By doing this, the impact of the simulated observations became more apparent and easier to quantify. Through this OSSE configuration Zack et al. were able to identify the optimal placement for their instruments and saw forecast improvements up to five hours from the initial time during the warm season.

Despite the benefits that can be gained from OSSEs, critics often point out weaknesses of OSSEs that must be taken into consideration during the experimental design. These criticisms are often centered on the identical twin problem as discussed previously. Hoffman et al. (1990), Atlas (1997), Arnold and Dey (1986), and Masutani et al. (2008) all stress the importance performing fraternal twin OSSEs. By making appropriate and sufficiently different model selections to be used as the nature run and experiment model, problems associated with similarities between model errors can be easily mitigated, thus eliminating one of the leading causes for overly optimistic OSSE results. Another common critique is that the precise error characteristics and capabilities of the instruments may not be explicitly known or appropriately modeled in the OSSE (Arnold and Dey, 1986). On a similar note, Atlas et al. 1985 points out that OSSE results can often be model dependent and the assignment of random errors is often incorrect. Additionally, Hoffman et al. 1990 points out that one of the biggest shortcomings of OSSEs is the assumption of uncorrelated errors. These incorrect error assumptions can

lead to overly optimistic results and make interpretation of results difficult (Hoffman et al. 1990). Finally, it is often noted that it is difficult to create a comprehensive set of simulated observations for all current observing networks in use today, making it difficult to precisely gauge the current state of operational NWP capabilities. Furthermore, OSSEs are only able to simulate the total observing systems in use today but are not able to account for all possible future observing systems that will be operational by the time the tested network is deployed.

Regardless of this caveat, both full OSSEs and quick OSSEs are still used today to study and develop the next generation of observing platforms. After more than fifty years of refinement the OSSE methodology remains a powerful tool to demonstrate the potential of new instrumentation and data assimilation methods. Although critics of OSSEs may point out the shortcomings of the process, such as the identical twin problem, inappropriate system capability assumptions, and inaccurate system error specifications, there remains no better way to test the value of an observing platform prior to expensive deployments.

Chapter 2

2.1 Numerical Modeling

2.1.1 Advanced Regional Prediction System (ARPS)

One of the key components to a successful OSSE is the creation of a Nature Run that is representative of the real atmosphere. In this study the Advanced Regional Prediction System (ARPS) was chosen to create the Nature Run. ARPS is a fully compressible, non-hydrostatic model developed by the Center for Analysis and Prediction of Storms (CAPS). The model uses a terrain-following vertical coordinate, a second-order-leap-frog scheme, and a user-selectable stretching option for the vertical spacing. Although it is scalable to meso and synoptic scales, the ARPS model was developed for modeling convection on storm scales (Xue et al. 2001a, 2001b). The ARPS model has been used to simulate a variety of meteorological phenomena such as tropical storms (Zhao and Xue 2009) and convective squall lines (Dawson et al. 2009) and has also seen been employed to create the nature run for mesoscale OSSEs (Zach et al. 2011, Gasperoni 2013). This study uses Version 5.4.2 of ARPS.

2.1.2 ARPS 3-Dimensional Variational System (ARPS 3DVAR)

The ARPS 3DVAR system is one of two data analysis programs that were developed specifically with the ARPS model by Gao et al. (2004). As with all 3DVAR techniques, the ARPS 3DVAR seeks to minimize a cost function J(x) defined by:

$$J(x) = \frac{1}{2}(x - x_b)^T \boldsymbol{B}^{-1}(x - x_b) + \frac{1}{2}[H(x) - y_o]^T \boldsymbol{R}^{-1}[H(x) - y_o] + J_c$$

The first term is the background constraint term and represents the difference between the state (x) and background (x_b) vectors weighted by the inverse of the background error covariance matrix (**B**). The second term represents the adjustment from the observed value (y_o) and the state vector projected to the observation space by the forward operator (H(x)), and weighted by the inverse of the observation error covariance matrix, **R**. The third term, J_c, is a mass continuity constraint term.

The specifications of **B** and **R** are important to the 3DVAR process, and in this study, **R** is assumed to be a diagonal matrix under the assumption that all observation errors are uncorrelated. The specification of the background matrix **B** involves using a recursive filter to create Gaussian and isotropic spatial correlations. Different decorrelation length scales can be applied to multiple passes of the filter such that **B** can change for different observation types. However, the background error matrix does not account for cross-correlations between different variable types.

In this study, the Incremental Analysis Updating (IAU) scheme (Bloom et al. 1996) is used in conjunction with ARPS 3DVAR. The IAU scheme takes the analysis increments from the background field created in the analysis step and inserts them into the ARPS model as a forcing term over a user specified time window. The increments are applied according to the equation:

$$\frac{dX(t)}{dt} = F(X) + \propto_{IAU} (X_a - X_b)$$

Where X represents the model variable, F represents the model forcing term, and $\propto_{IAU}$ is the IAU weighting coefficient acting on the analysis increment (X_a – X_b). These increments are applied to the model field as specified by the user at discrete time intervals.

A triangular shape is used in this study such that the maximum of the increment is applied in the middle of the time window. In this way the increments match the observation time more closely while gradually transitioning to a free forecast to reduce noise after the assimilation time window. Studies show that using IAU can help reduce noise in model fields immediately following data assimilation and has been shown to improve strength and maintenance of convective storms (Brewster 2003, Brewster 2015).

2.1.3 ARPS Data Assimilation System (ADAS)

The second data analysis package within ARPS is the ARPS Data Assimilation System (ADAS). Unlike ARPS 3DVAR, ADAS employs the Bratseth successive correction scheme (Bratseth 1986) that iteratively analyzes measurements of wind velocity, pressure, potential temperature, and specific humidity from a wide variety of sources. At the end of the iterations the solution converges to that of Optimal Interpolation. ADAS's ability to easily incorporate observations from numerous and often disparate instrument platforms (such as surface observing networks, soundings, aircraft measurements, profilers, radar, and satellites) makes it a valuable data assimilation system that has seen use in several research applications (Brewster, 2003b, Watson, 2010).

In ADAS several passes of the successive correction are performed, each with a different correlation scale length such that widely-spaced observations can be applied first to correct for synoptic scale errors before including higher density observations such as radar reflectivity and velocity. The scheme can be described by the equations:

$$s_x(n) = s_x(n-1) + \sum_{j-1}^{nobs} \propto_{xj} [s_j^o - s_j(n-1)]$$

$$s_i(n) = s_i(n-1) + \sum_{j-1}^{nobs} \propto_{ij} [s_j^o - s_j(n-1)]$$

Where the variable (s) at the grid point (x) and observation point (i) is analyzed using the observations (s_j^o) weighted by the weighting factors ($\propto_{xj}$, $\propto_{ij}$) during the nth iteration. Background and observation error variance are incorporated into the weighting factor by the equation:

$$\propto_{ij} = \frac{(\rho_{ij} + \sigma_n^2 \delta_{ij})}{m_j}$$

Here σ_n^2 is the ratio of the observation and background error variance and δ_{ij} is the Kronecker delta tensor, and ρ_{ij} represents spatial correlations. These spatial correlations contained in ρ_{ij} are assumed to be Gaussian and are weighted by the horizontal and vertical separation between the grid point and observation point.

A unique aspect of ADAS is the Complex Cloud Analysis, a module within ADAS that employs surface, radar, and satellite observations to estimate moisture and hydrometeor fields as well as apply temperature increments to account for latent heating (Zhang et al. 1998, Brewster 2002). Additionally, ADAS (and ARPS 3DVAR) have a quality control module that automatically rejects any observation that is over a set error threshold when compared to neighboring observations. This threshold is dependent on observation type and is determined by the specified observation error variance and a

quality multiplier for each source. As with ARPS 3DVAR, ADAS increments can be assimilated in the model using the IAU scheme.

With the use of the additional software packages, wrf2arps and arps4wrf, ADAS can act as the data assimilation program for initializing forecast runs of the Weather Research and Forecasting (WRF) model, as described in Watson (2010) and Case et a. (2006). ADAS will be used in this study to assimilate synthetic observations and perform data assimilation cycling for the WRF experimental forecasts and will be discussed in section 2.1.5.

2.1.4 Weather Research and Forecasting (WRF) Model

The WRF model was developed by NCAR as community mesoscale model that could fill both research and operational numerical modeling roles. As a multipurpose model, including use in many OSSEs (e.g., Jones et al. 2013, Zach et al. 2011, Liu et al. 2009), the WRF provides a common building block that allows easy transition from the research to operational applications. The WRF model is fully compressible and has two dynamical cores, the Advanced Research WRF (ARW) maintained by the National Center for Atmospheric Research (NCAR), and the Nonhydrostatic Mesoscale Model (NMM) used by the National Center for Environmental Prediction (NCEP). In the WRF-ARW (Version 3.8) used here, a staggered Arkawa C-grid is employed along with a user-selectable vertical grid. Positive-definite advection options for moisture and turbulent kinetic energy are available and use 2nd to 6th order horizontal and vertical advection options with Runge-Kutta 2nd or 3rd order timesteps. Grid nesting is available but is not used in this study. In a typical WRF simulation or forecast, the WRF Preprocessing System (WPS) unpacks the Gridded Binary (GRIB) data from an external model, creates

the WRF grid, and creates the initial and boundary condition files that WRF requires for a full model integration. While WPS is used to create the WRF control run (see section 3.5), the creation of initial and boundary condition files can be performed instead by the arps4wrf program, as is done with the WRF experiment forecasts (outlined in section 2.1.5).

2.1.5 WRF Data Assimilation Cycling

Following the examples of Watson (2010) and Case et al. (2006), the ADAS program is used for data assimilation cycling of the WRF OSSE forecasts. This procedure begins by using the 12Z WRF output file from the WRF Control Run (to be described in section 3.5) as the initial background file. Since the ADAS program works in the ARPS framework the WRF background file must be converted to an ARPS format. This is done by processing the WRF background file through the ARPS program wrf2arps to convert the WRF gridded data into an ARPS format grid of the same dimensions. Synthetic observations extracted from the ARPS Nature Run are then assimilated with ADAS on the ARPS grid. The resultant analysis is then converted back into a WRF-usable format through the program arps4wrf. During this conversion the exact WRF model vertical levels are given as output by the program arps4wrf, allowing for consistent vertical grid dimensions between the conversion steps.

Six passes of the Bratseth successive correction scheme are applied during the ADAS step to incorporate the simulated observations into the background fields. Correlation length scales were chosen based on the experimental ADAS configuration used for high resolution convective forecasting. An initially large spatial correlation length scale is used for the first two passes with decreasing correlation length scales for

each successive pass (Table 2.1). Additionally, the background error file is updated every two hours during the 6-hour DA cycle. Background error values for pressure, relative humidity, temperature, and U and V wind components were reduced to account for the increasing confidence a high-resolution model gains through the DA cycle. Initial background error values from the Rapid Update Cycle (RUC) 3-hour forecast error were used and reduced by 66% during each update. Additional fine tuning of the second and third background error files was incorporated to give realistic results for the WRF experiment that incorporated the simulated observations from current observing networks only, ensuring that this experiment compared well to current operational NWP performance. These background error files and correlation length scales are held constant for all experiments.

Lateral boundary conditions provided by the GFS (see section 3.5) are also processed through these conversion steps to allow for the same number of vertical levels in the boundary condition files as in the initial condition files. Once the initial boundary condition and lateral boundary condition files are created, a 1-h WRF forecast is produced. The output from this 1-h forecast is used as the background file for the next data assimilation step. This procedure is repeated for the duration of the data assimilation cycling period.

Table 2.1: Correlation Length Scales used during the ADAS procedure.

Pass Number	Correlation Length Scale (km)
1	**200**
2	**150**
3	**120**
4	**80**
5	**65**
6	**50**

2.2 Simulated Observations

One key aspect of OSSEs is the generation of synthetic observation data from both current and proposed observation networks. Whether the observations are in-situ or collected via remote sensing, proper creation of synthetic observations includes realistic spatio-temporal frequency of observations as well as accurate error characteristics. In this OSSE both the current operational observing suite (i.e., all the observations used to initialize the GFS), and the proposed 3-D Mesonet network are simulated. Incorporating the complete operational observing networks ensures that OSSE results will not be overly optimistic and give a representative measure of the impacts the 3-D Mesonet observations could have on operational NWP.

2.2.1 Simulating Real Observing Networks

In most traditional OSSEs, such as Atlas 2015, all current observing systems (such as satellites, radars, LiDARs, surface, and upper air observations) are individually

simulated. These are highly detailed simulated observations complete with appropriate instrument errors characteristics. However, creating the necessary hundreds of millions of such observations from all observing networks, especially satellite and radar networks, is highly time intensive. To expedite this OSSE experiment, not all observing systems are explicitly simulated. Instead, Final Analyses from the Global Forecast System (GFS FNL) are simulated and used as a proxy for implicitly simulating all observing networks.

At the National Center for Environmental Prediction (NCEP) the GFS is run every six hours, and global observations used in the GFS are collected up to one hour after the model start time. For example, data for the 12 UTC initialization of the GFS will include observations up to 13 UTC. Although the GFS forecast is begun earlier to meet time-critical forecast needs, the late observations are still used in the Global Data Assimilation System (GDAS), which is also used by the GFS. These additional observations are assimilated into a GFS FNL analysis that is used as the initial background field at the beginning of the data assimilation cycle for the next GFS run. Typically, FNL analyses contain ten percent more observations than the GFS analyses used to initialize each run of the GFS (Peng 2014). These FNL analyses represent the accumulation of all global observing networks and are assimilated into the GFS as a gridded 1-degree-by-1-degree network of data at the surface and 26 pressure surfaces in the vertical from 1000 hPa to 10 hPa (NCEP 2000).

Psuedo-observations, hereafter FNL obs, representing the FNL analyses are extracted from the ARPS Nature Run data and are assimilated into the WRF experiments as a network of soundings on a 1-degree-by-1-degree grid with temperature, dewpoint, pressure, geopotential height, wind speed and wind direction available at the surface and

twenty-six pressure levels. FNL obs from the Nature Run are created using linear interpolation on a logarithmic pressure scale to the twenty-six pressure levels and the surface level. Since the ARPS Nature Run only extends to 50 hPa, linear extrapolation on a logarithmic pressure scale is used to find data on the 10 hPa pressure surface. One notable difference is that while the real GFS FNL analyses are assimilated every six hours into the operational GFS, here they are assimilated every three hours in order to account for the more frequent data assimilation cycles used by mesoscale models. Errors for each variable of the FNL obs were randomly sampled by a non-biased Gaussian distribution. These distributions were characterized by standard deviations that were determined by the average RMS error of the operational GFS for the 0-24 hour forecast period during the month of May 2017 (provided by the Earth System Research Laboratory (ESRL)). Since the average RMS error from the GFS varied with height, the standard deviations, and hence the Guassian error distributions, varied with height for each variable. Additionally, the standard deviations for the error distributions were increased slightly for pressure levels greater than 850 hPa to replicate decreased observational accuracy within the PBL. These standard deviation values used for the FNL observations are given in Table 2.2.

Although the GFS FNL analyses are intended to act as a proxy for most current observing networks, one exception is the surface data from the Oklahoma Mesonet (Brock et al. 1995). This was done in order to allow a comparison of the impacts of large scale observations (GFS final analysis soundings) versus mesoscale observations and to act as a rough calibration of a current observation system on the OSSE. Mesonet observations were simulated by extracting 1.5-m temperature and dewpoint, 2-m wind

speed, surface pressure, 10-m wind speed and direction, and 9-meter air temperature from the Nature Run.

For the Oklahoma Mesonet, errors for each observation type were found by randomly sampling from a Gaussian distribution with each instruments' accuracy set as the standard deviation of the distribution. When appropriate, the instrument accuracy, and thus the Gaussian distribution, varied based upon other environmental factors. For example, the thermistor used for nine-meter air temperature is non-aspirated and therefore the instrument accuracy is sensitive to changes in wind speed. This sensitivity is reflected in the generation of simulated errors by using ten-meter wind speed as a proxy for nine-meter wind speed and adjusting the accuracy of the thermistor as necessary (Oklahoma Mesonet, McPherson et al. 2006).

Table 2.2: Standard deviation values for Gaussian error distributions for each observation type.

Variable	Standard Deviation Value	Variable Dependencies
GFS FNL		
U & V wind (m/s)		Press (hPa)
	4.5	< 100
	4.5	199 – 100
	4.0	399 – 200
	3.25	699 – 400
	3.0	850 – 700
	4.0	> 850
Temp (C)		
	1.5	< 100
	1.75	199 – 100
	1.5	399 – 200
	1.0	699 – 400
	1.25	950 – 700
	5.5	> 950
RH (%)		
	14.0	< 100
	20.0	299 – 100
	14.0	799 – 300
	13.5	950 – 600
	15.0	> 950
Geopotential Height (m)		
	55.0	< 200
	35.0	299 – 200
	25.0	499 – 300
	23.0	699 – 500
	17.0	950 – 700
	20.0	> 950
Mesonet		
1.5 m Temp (C)		-
	0.5	
9 m Temp (C)		Wind Speed (m/s)
	0.5	>= 6.0
	1.0	3.0 – 5.9
	1.5	2.0 – 2.9
	3.0	0.0 – 1.9
1.5 m RH (%)		RH (%)
	2.0	<= 90
	3.0	> 90

Wind Speed (m/s)		-
	0.3	
Wind Direction (degrees)		-
	3.0	
Pressure (hPa)		-
	0.4	
UAV (CoperSonde)		
Temp (C)		Press (hPa)
	0.2	> 100
	0.3	<= 100
RH (%)		-
	5.0%	
Wind Speed		Press (hPa)
	0.5	> 100
	1.0	<= 100
Wind Direction (degrees)		-
	5.0	
Pressure (hPa)		-
	1.0	

2.2.2 Simulating UAV Observations

For the proposed UAV system, observations were extracted in a manner similar to the processing for the GFS final analysis soundings with a few additional steps. For simplicity, each 3-D Mesonet UAV site was assumed to be co-located with an Oklahoma Mesonet site. Oklahoma Mesonet sites that were near or co-located with an airport were excluded from being eligible 3-D Mesonet sites. All eligible 3-D Mesonet locations are shown in Figure 2.1. The flight path of each UAV is assumed to follow a vertical ascent and descent, a realistic assumption considering most copter UAV's, including the OU CopterSonde, have the ability to adjust for wind speed and direction to maintain a set flight plan. Observations were simulated for the ascent portion of the flight only. This was done to represent the idea that once a UAV has completed its observation gathering

ascent it can make a much quicker descent back to the landing site to conserve battery life. The vertical ascent of the CopterSonde is designed to be a constant 3 ms^{-1} with height, pressure, temperature, humidity, wind speed and wind direction measurements taken every ten meters. By this standard, a routine flight to 400 feet (or nearly 122 meters) would take roughly twelve measurements in just over forty seconds and a flight to 3 km AGL would take just under 17 minutes to collect 300 measurements.

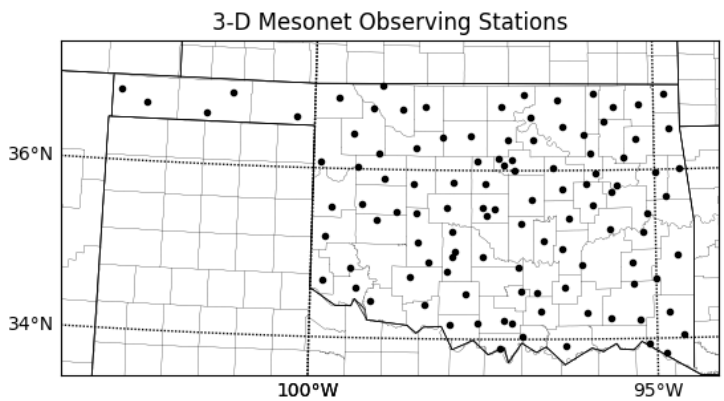

Figure 2.1: 110 3-D Mesonet simulated observation sites.

Extracting the UAV observations from the Nature Run begins by finding the ARPS Nature Run grid point closest to the 3-D Mesonet location. Since the Nature Run has a high 1 km resolution, the maximum theoretical distance between a grid point and 3-D Mesonet site is roughly 0.71 km. However, it was found that the average grid-to-observation point distance was only 0.32 km with a maximum distance of around 0.45 km and a minimum distance less than 0.1 km. This average distance is short enough to be considered representative of the 3-D Mesonet location and yet can account for representativeness error in the extracted observations. ARPS Nature Run data is collected at the determined grid point from every vertical level. A simulated UAS vertical profile

up to 3km AGL was then created by performing vertical linear and Lagrangian interpolation on a logarithmic pressure scale for the first and subsequent CopterSonde observation levels respectively. The vertical interpolation schemes are similar to those outlined by Shen et al. (1985). Since the Nature Run atmospheric data are available in five-minute increments, the simulated CopterSonde data are time adaptive; after every five minutes of simulated flight time a new Nature Run file is used for sampling. This is done to replicate changing atmospheric conditions while the CopterSonde is in flight, particularly for simulated flights longer than five minutes (or in other words, flights up to 900 m or greater).

Additionally, UAV observations are constricted by cloud cover. In order to comply with FAA visual flight rules (FAA 2005, 2016) if the CopterSonde encounters a region of high humidity (96% or greater) or a combined value of cloud water vapor and cloud ice mixing ratio greater than 10^{-6} kg/kg (Arbizu-Barrena et al. 2015) then it is assumed a cloud layer has been detected and the observation flight is ended. One aspect of the 3-D Mesonet that is not modeled in this study is the capability of the CopterSonde to avoid air traffic. Although a system is being designed by CASS and the Advanced Radar Research Center (ARRC) to end CopterSonde flights with the approach of a commercial or private aircraft, the amount and average altitude of air traffic over each Oklahoma Mesonet site is relatively unknown and presumed to be sparse.

Instrument errors are modeled after the RS92 NGP Viasala radiosonde package since the instrument error goals of the CopterSonde are designed to mirror this instrument package. Error values are assumed to be unbiased and follow a Gaussian distribution with the Vaisala instrument error range set as the standard deviation of the distribution (Vaisala

2013). As with the simulated FNL and Oklahoma Mesonet errors, simulated CopterSonde errors take into account changes in instrument behavior based on environmental conditions such as extreme temperatures, wind speed, and altitude. However, these errors do not account for instrument drift after prolonged and repeated use, a known problem with radiosonde hygrometers that the developers of the CopterSonde are seeking to mitigate. Errors are added to each interpolated Nature Run data point through random sampling of the distribution. As mentioned, additional unknown representativeness errors are introduced due to the nearest-neighbor grid point selection method. But these errors are considered to be small compared to the instrumentation errors added intentionally to the simulated observations.

Chapter 3

3.1 Case Study Selection

Similar to the NSSL EPIC campaign in fall 2016 (Koch et al. 2017), one of the primary foci of the 3-D Mesonet concept is to help improve current numerical forecasting of severe convection, especially convective initiation. Because of this goal, case selection was limited to convective events with clear initiation of discrete convective storms. Additionally, selection was limited to daytime events to allow for sampling of the evolving daytime PBL prior to initiation. Events with weak synoptic forcing, such as initiation off a dryline, were preferred as prediction of these events may be more sensitive to differences in observational coverage. Based on these criteria, the severe weather event that occurred on 20 May 2013 was selected, as discrete convection occurred along a dryline during the early afternoon hours in central Oklahoma.

3.2 Event Overview and Synoptic Setup

May 20th, 2013 is perhaps best known for the violent EF-5 tornado that struck Moore, Oklahoma. However, the severe weather outbreak on this day was widespread, resulting in over 400 severe weather reports, 37 of which were tornadoes (Figure 3.1). For the purposes of this study, attention will be focused on the convective events that unfolded across central Oklahoma. The severe weather that occurred on the 20th followed the severe events that occurred on May 19th across the Southern Plains in a two-day severe weather outbreak. This outbreak was associated with a strong, but slow moving mid-level longwave trough moving across the western United States. By 12 UTC on 20 May the mid-level wave had begun to deepen and slowly move northeastward across the Central Plains. This placed much of Oklahoma under a southwesterly 22-25 ms^{-1} (45-50

kt) flow aloft. The surface low associated with the upper level trough can be seen in 12 UTC surface observations in southeastern South Dakota, vertically stacked underneath the upper level low. A weak, stationary surface frontal boundary was draped southward from the surface low through Iowa, eastern Kansas, and down the Interstate 35 corridor in central Oklahoma (Figure 3.2).

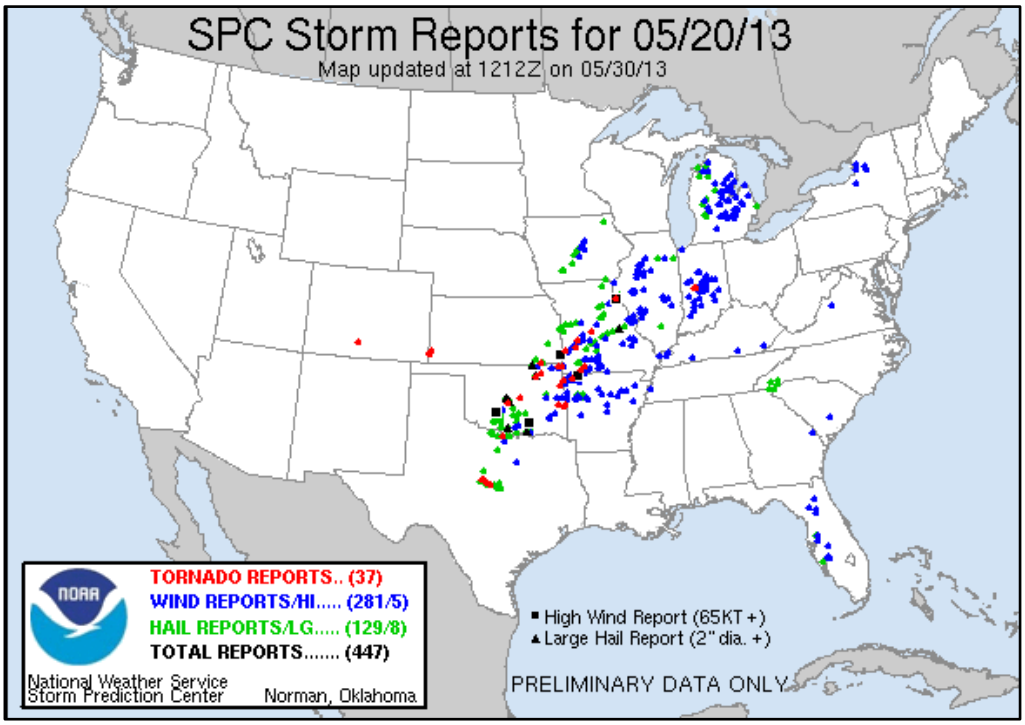

Figure 3.1: All severe weather reports from 20 May 2013 (SPC).

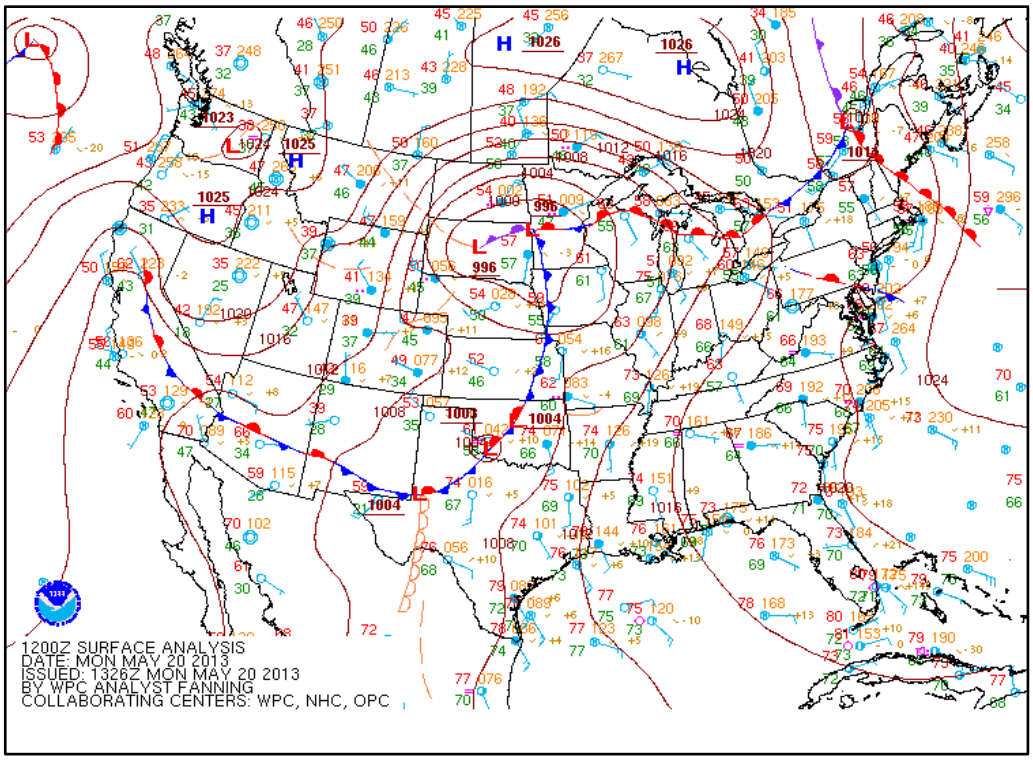

Figure 3.2: Surface objective analysis chart valid at 12 UTC 20 May 2013 (SPC).

While this boundary would become the focus for convection later in the day, a few additional features should be noted in the 12 UTC surface observations. The most notable is the weak surface low present over western Oklahoma. Just to the east-northeast of this low is a weak warm frontal boundary separating warm, southerly return flow with temperatures in the 20-25 C (70 to 75 F) range from cooler air to the north. During the morning hours a few elevated thunderstorms occurred along this boundary but were quickly advected to the northeast into a less favorable environment. A 17 ms^{-1} (35 kt) southwesterly 925 hPa wind was overriding the warm sector across eastern Oklahoma, allowing for a strong meridional flux of low level moisture. A distinct dryline was present to the south-southwest of the surface low with a more diffuse dewpoint gradient present

to the west of the low. These features are all illustrated in the composite analysis in Figure 3.2.

The 12 UTC upper air sounding released from Norman, Oklahoma (OUN) (Figure 3.3a) revealed a thermal profile with a deep elevated mixed layer extending from 850 hPa to 500 hPa. This layer of nearly dry-adiabatic lapse rates helped support over 2300 J/kg of mixed layer Convective Available Potential Energy (CAPE), which was held-back by a capping inversion with -199 J/kg of Convective Inhibition (CIN). Additionally, the environmental winds were supportive of severe organized convection with surface to 6-km bulk wind shear of 50 knots and surface to 1-km Storm Relative Helicity (SRH) of 308 m^2s^{-2}.

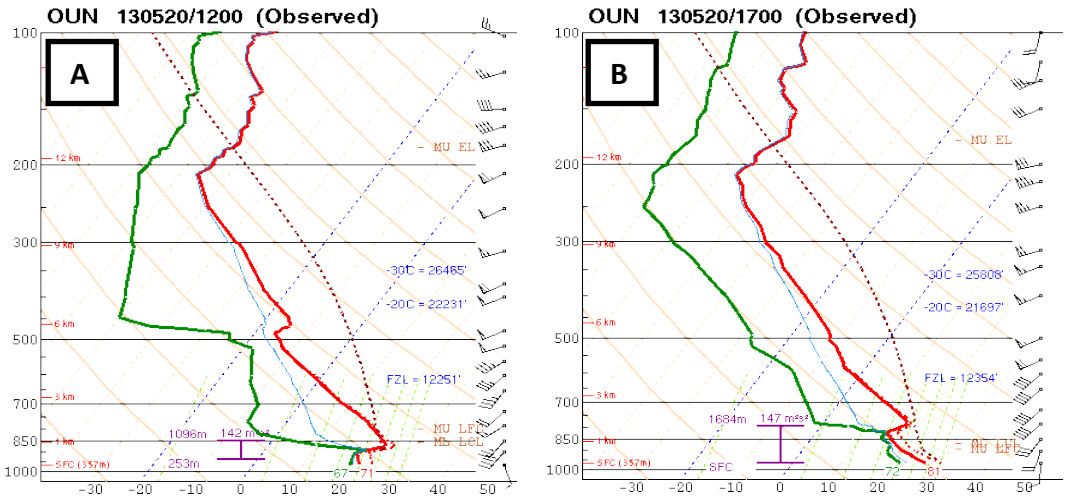

Figure 3.3: Observed soundings from OUN at 12 UTC (A) and 17 UTC (B).

By 18 UTC vertical mixing of strong low-level winds strengthened the surface wind field and allowed for steeper low-level lapse rates as observed by a special 17 UTC upper air sounding from Norman, Oklahoma (OUN) (Figure 3.3b). Surface observations

from this time show a dryline bulge across southern Oklahoma to the southwest of Norman, OK (Figure 3.4). This dryline bulge would act as the forcing mechanism to initiate convection across southern Oklahoma, including the supercell that would eventually spawn the Moore tornado. Further to the north in north central Oklahoma and southeastern Kansas, convective initiation commenced along the stationary boundary shortly after the onset of convection to the south. During the first few hours of the event, the mean cloud layer flow orthogonal to the dryline and stationary boundary allowed for storms to remain discrete. However, by 00 UTC cells began to congeal into a broken line. This line of storms continued to produce severe weather as it propagated into northwestern Arkansas and southwestern Missouri. By 06 UTC the initial round of convection had propagated well into Arkansas and Missouri with only elevated convection lingering across central and eastern Oklahoma.

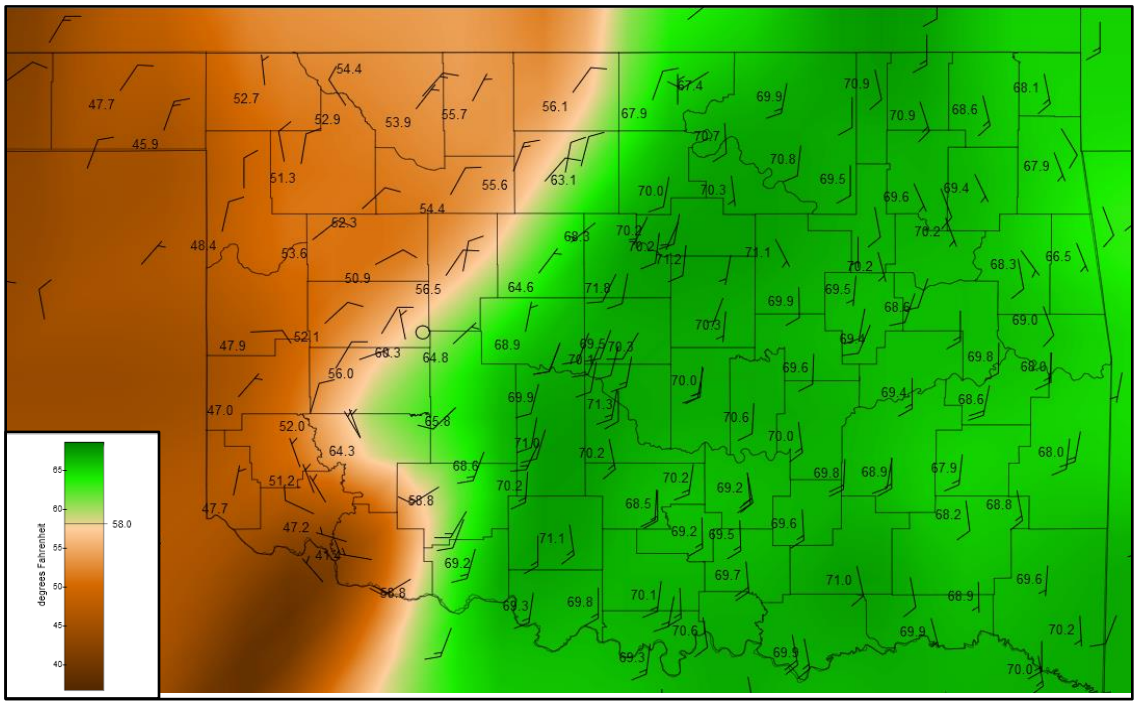

Figure 3.4: Observed surface dewpoints (fill, deg F) and 10 m wind vectors (barbs, knots) from the Oklahoma Mesonet valid at 17 UTC 20 May 2013.

3.3 ARPS Nature Run

The Nature Run for this study was created using the ARPS model over a 900 by 900 km domain centered over the state of Oklahoma with a 1 km horizontal resolution. The 61 vertical levels were determined by the cubic vertical stretching function within the ARPS program (Xue et al. 2000a) with the lowest vertical spacing being 20 m (first level at 10 m AGL) and the model top at a height of 20.5 km AGL (around 50 hPa) (Figure 3.5a). Parameterization schemes included a two-moment bulk microphysics parameterization with a fixed spectral shape parameter (Milbrandt and Yau 2005a, 2005b), a staggered atmospheric radiation transfer parameterization scheme, built off the work of Chou (1990,1992) and Chou and Suarez (1994) (Xue et al. 2000b). Surface fluxes were calculated from stability-dependent surface drag coefficients, surface temperature and water content, and the boundary layer parameterization was the 1.5 turbulent kinetic energy mixing scheme developed by Moeng (1984). Since the horizontal grid length is 1 km, this classifies as a convection resolving model, therefore no cumulus parametrization was employed.

Initial condition and lateral boundary condition inputs for the Nature Run were supplied by the operational North American Model (NAM) beginning at 06 UTC on May 20th. Surface observations from the Oklahoma Mesonet, as well as METAR locations, upper air, infrared satellite, and regional radar observations were assimilated into ARPS every two hours between 06UTC and 12UTC using ARPS 3DVAR increments applied by the IAU-VDT scheme. At 12UTC a free forecast was run until 06 UTC on May 21, when all convection had exited the area of study. Output from this free forecast was archived every 5 minutes.

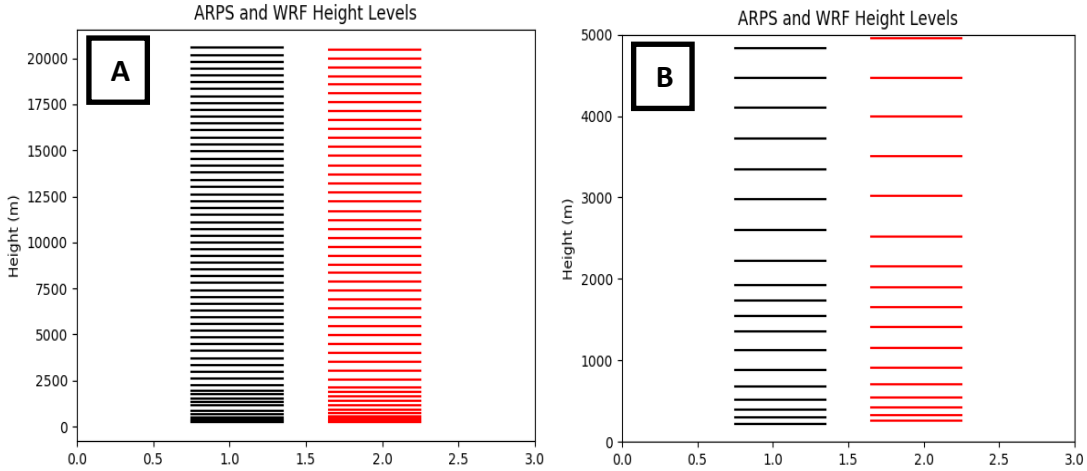

Figure 3.5: Vertical levels of the ARPS (61 levels - black) and WRF (50 levels - red) models used in this study (A), and a closer look at distribution of model levels in the lowest 5 km (B).

3.4 Comparing the Nature Run to Reality

One of the components of a valid OSSE is to have the modeled atmosphere in the Nature Run accurately represent the real atmosphere (hereafter called Reality). Typically, in larger scale OSSEs where the Nature Run is integrated for multiple days to months this is done by computing model climatology statistics and comparing these to real climatological statistics (Masutani et al. 2010). However, because this OSSE focuses on an 18 h period, a modified criterion will be set. Since one of the main goals of this study is to reproduce the convective initiation across south central Oklahoma, a qualitative comparison is made to determine if the Nature Run accurately captures this convection and its subsequent evolution. Additionally, other surface fields are analyzed for comparison. It should be noted that an exact recreation of the actual meteorological events, such as exact placement of individual supercell storms, is not required for a valid Nature Run. What is required is a meteorologically sound representation and evolution

of the mesoscale environment as a whole, following the precedent set by Tong and Xue (2005) and Gasperoni et al. (2013) whose nature runs contained realistic initiation and evolution of convective storms. For comparison in this study, Nature Run plots of composite reflectivity are compared to composite WSR-88D radar mosaics from the Southern and Central Plains while surface dewpoint and wind fields are compared to objectively analyzed Mesonet surface observations.

Plotting and comparing composite reflectivity from the Nature Run to Reality gives an idea of how accurate the ARPS model integration represents the convective evolution on May 20th. Beginning at 12 UTC it can be seen that as a whole, the ARPS Nature Run captures the morning set up relatively well. Storms that were ongoing in southeastern Kansas and southwestern Missouri are present in the Nature Run, through storm intensity and coverage is higher in the Nature Run (Figure 3.6). This is likely due to stronger convergence in the Nature Run along the warm front than was occurring in Reality as suggested by the surface dewpoint plot in Figure 3.7. Here it can also be seen that the overall mesoscale environment is recreated accurately with a dryline present across western Oklahoma. At first glance the small-scale wave features present in the surface dewpoint plot in the Nature Run appears to be too noisy when compared to Reality. However, this is misleading as the average station spacing for the Oklahoma Mesonet is roughly 35 km (Brock et al. 1995) and therefore is not able to fully resolve smaller scale features that may have been present in Reality.

By mid-morning at 15 UTC, the initial convection present in the Nature Run has grown upscale and moved eastward into southern Missouri. While this convection had dissipated in Reality, there is a secondary line of storms along the Kansas/Missouri border

that is present in Reality. Additionally, the light precipitation that was occurring over northwest Oklahoma and south-central Kansas is accurately captured by the Nature Run. The biggest discrepancy comes from the spotty rain showers in southeast Oklahoma and southwest Arkansas that persisted through the morning hours in the Nature Run but not in Reality.

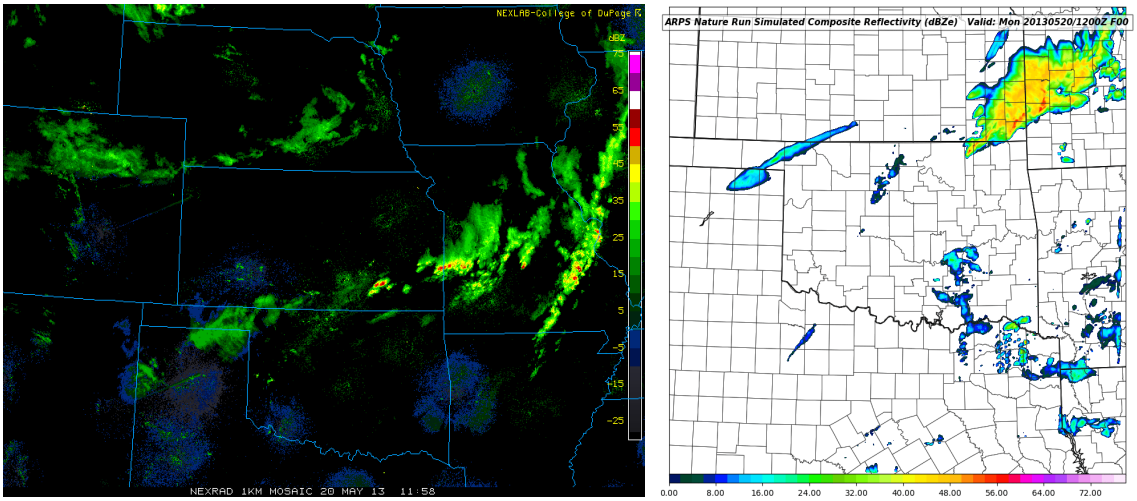

Figure 3.6: Comparison of the observed WSR-88D composite reflectivity radar mosaic (left) and the ARPS Nature Run composite reflectivity (right) at 12 UTC May 20, 2013.

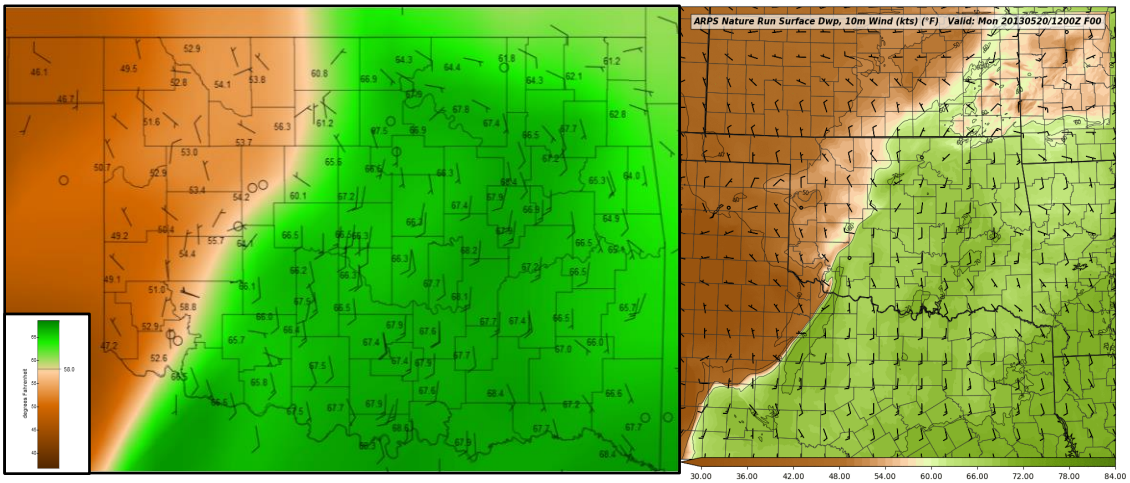

Figure 3.7: Comparison of the observed Oklahoma Mesonet dewpoint temperature (deg F, fill) and 10 m wind vectors (barbs, knots) (left) and the ARPS Nature Run 2 m dewpoint temperature (deg F, fill) and 10 m wind vectors (barbs, knots) (right) at 12 UTC May 20, 2013.

By 18 UTC the Nature run begins to show the first signs of convective initiation in south central Oklahoma and parts of northern Texas. In Reality, convective initiation began between 18 and 19 UTC along the Interstate 44 corridor to the north and west of the Nature Run's convection. Figure 3.8a shows the similarity between the Nature Run and reality with regards to this convective initiation as both show growing discrete storms in south central Oklahoma at 1900 UTC, through the Nature Run's storms are displaced slightly to the east and south. Storms initiating along the stationary boundary in north central Oklahoma and southeast Kansas in Reality are replaced by convection along a warm frontal boundary in the Nature Run. This is likely the result of a northward displacement of the surface low and stronger frontal boundary in the Nature Run. However, by 20 UTC the Nature Run does show convective initiation along the stationary boundary in eastern Kansas/southwest Missouri (figure 3.8b).

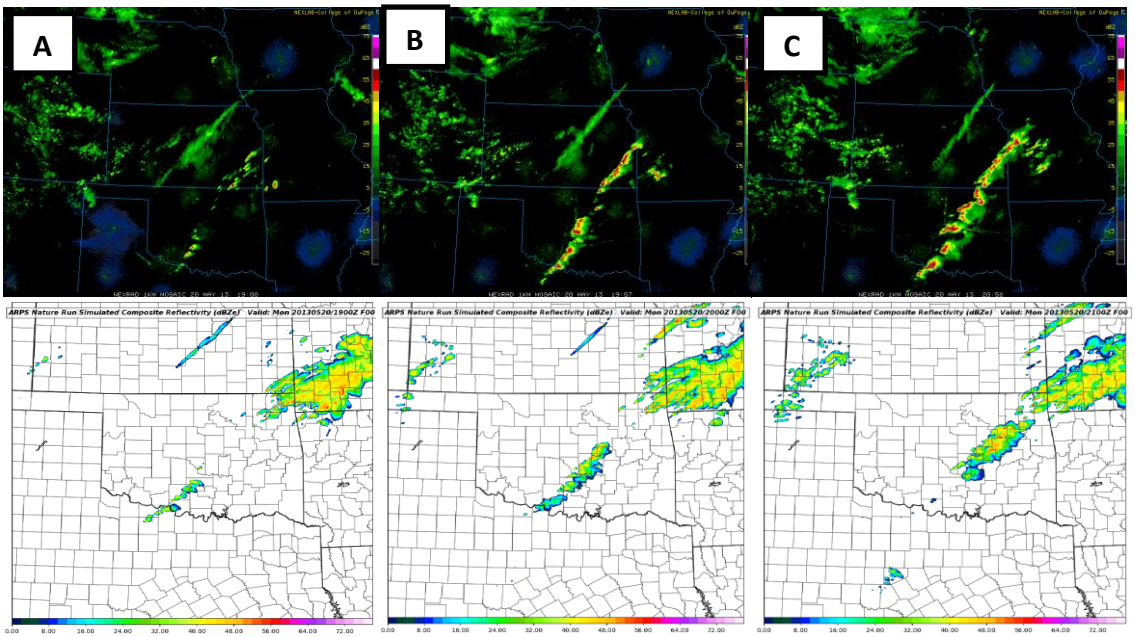

Figure 3.8: Comparison of observed WSR-88D composite reflectivity mosaic (top) and ARPS Nature Run composite reflectivity (bottom) fields valid at 19 (A), 20 (B), and 21 (C) UTC 20. May 2013.

From this point on the evolution of the Nature Run continues to follow Reality, through a considerable time lag begins to develop. By 22 UTC the initial storms that began in south central Oklahoma have moved off to the northeast in both the Nature Run and Reality. However, a secondary round of convection occurs in south central Oklahoma in the Nature Run whereas Reality shows a broken line of storms that began in north central Texas and moved to the northeast into south central Oklahoma. But the Nature Run continues to follow Reality as the broken line of storms eventually begin to grow upscale into a more linear structure and move to the east into western and northwestern Arkansas. There is a slight time lag in the Nature Run as the eastward progression of the convective line is slower than Reality. Figure 3.9 shows this lag as the observed storms are well into western Arkansas while the southern end of the Nature Run line is still partially in southeastern Oklahoma. However, even with this phase shift, similar bow-echo storm structures can be observed in both Reality and the Nature Run.

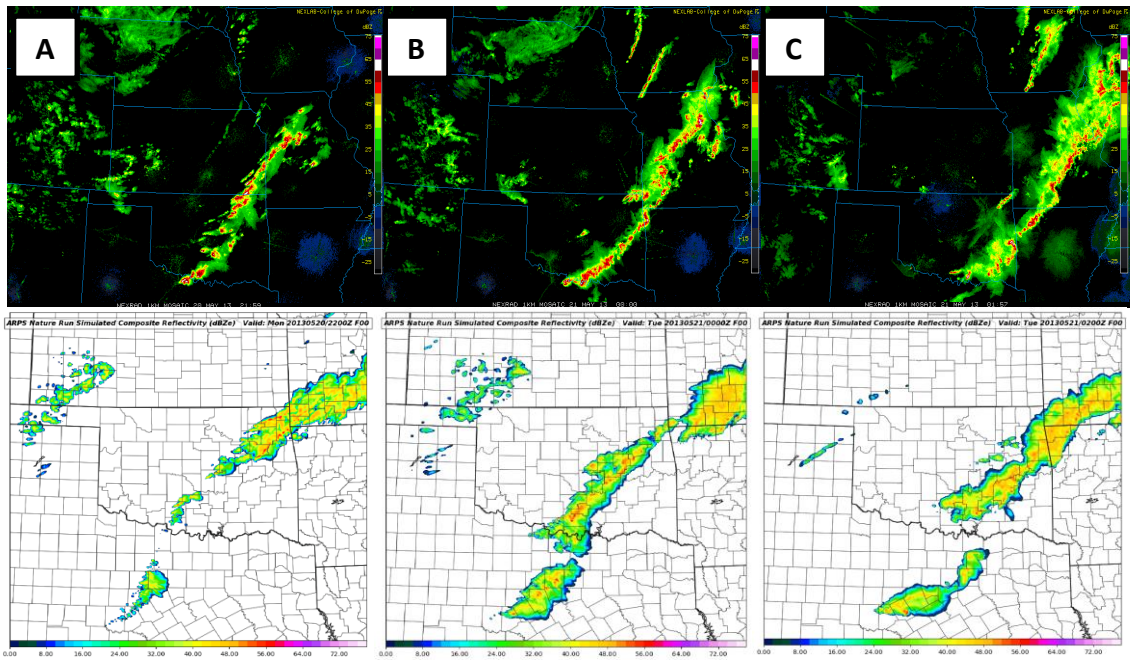

Figure 3.9: Comparison of observed WSR-88D composite reflectivity mosaic (top) and ARPS Nature Run composite reflectivity (bottom) fields valid at 22 (A), 00 (B), and 02 (C) UTC on 20/21 May 2013 respectively.

Another method for validating the Nature Run is to compare upper air soundings between the Nature Run and Reality. Overall, the sounding extracted from the Nature Run at 12 UTC OUN compares well with Reality's observed sounding (figure 3.10). Both show a notable inversion with a temperature maximum near 850 hPa with an elevated mixed layer with nearly dry adiabatic lapse rates to just below 500 hPa. Additionally, the mid to low level moisture profile is captured well in the Nature Run when compared to Reality. The two thermal profiles also support very similar values of surface-based CAPE and similar magnitudes of CIN. It is noted that the Reality sounding does possess a warmer surface temperature and dewpoint, which accounts for the differences in CAPE and CIN values. The one notable difference between the two is the observed cloud layer with a shallow surface boundary layer with conditionally unstable lapse rates. This is not present in the Nature Run sounding, which does not have this shallow boundary layer.

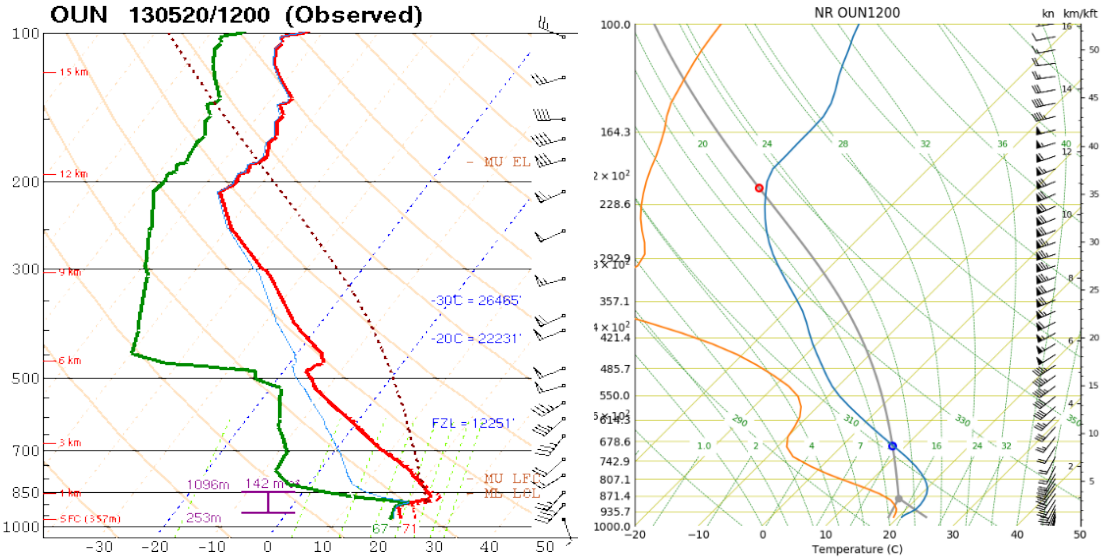

Figure 3.10: Comparison between the 12 UTC observed sounding from Norman, OK (left) and the 12 UTC Norman sounding taken from the ARPS Nature Run (right).

As mentioned, a special sounding was launched from OUN at 17 UTC to support forecasting operations that day (Figure 3.3b). This additional sounding allows for a comparison of the warm sector environment shortly before convective initiation. The 17 UTC OUN sounding shows a thermal profile conducive to severe convection with nearly 5000 J/kg of surface-based CAPE and no surface based CIN. There is a slight capping inversion still in place as quantified by the small amount of mixed layer CIN. Although many of the small-scale details of the corresponding extracted sounding are smoother, the Nature Run 17 UTC extracted sounding at OUN sounding shows very similar features with a dry adiabatic layer underneath a slight capping inversion, and low-level moisture extending to nearly 850 hPa (Figure 3.11). As in the observed OUN sounding, the Nature Run profile shows ample amounts of surface-based CAPE with no surface based CIN. The amount of CAPE in the Nature Run sounding is less than in Reality; this is likely due to the fact that the Reality profile has a slightly higher surface temperature and dewpoint.

These comparisons of composite reflectivity, surface fields, and upper air soundings all demonstrate that, despite a few differences, the Nature Run is capturing the general mesoscale environment and evolution. The Nature Run was able to correctly capture the convective initiation across south central Oklahoma and the subsequent convective evolution from discrete storms into a linear complex. This gives high confidence that the Nature Run satisfies the requirements that the simulated atmosphere in this OSSE is representative of reality. Thus, it can be expected that the experiments performed in this environment will give realistic results that will apply to operational numerical weather prediction.

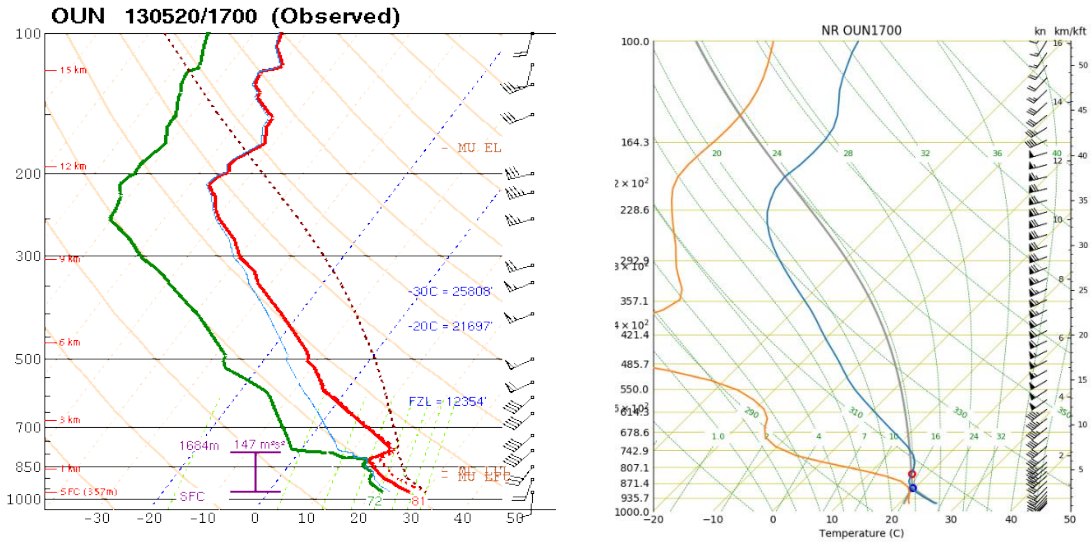

Figure 3.11: Comparison between the 12 UTC observed sounding from Norman, OK (left) and the 12 UTC Norman sounding taken from the ARPS Nature Run (right).

3.5 WRF Control Run

In order to examine the impacts of assimilating synthetic observations a Control Run of the forecast model is performed in which no observations are assimilated. Ideally, this control run uses a different numerical model from the Nature Run to avoid the "identical twin" problem and is sufficiently different enough from the Nature Run so that meaningful results can be obtained from the forecast experiments. If the control run and Nature Run are too similar, then drawing meaningful conclusions becomes very difficult. For this OSSE, the WRF-ARW is used for both the control run and the forecast experiments. To create the control run, a 237 by 201 grid-point, 3 km grid is placed over the state of Oklahoma (Figure 3.12) with 50 vertical levels (figure 3.5b). Thompson microphysics (Thompson et al. 2008), the MYNN planetary boundary layer scheme (Nakanishi and Niino 2006), Dudhia shortwave radiation scheme (Dudhia 1986), and the

Rapid Radiative Transfer Model long wave radiation scheme (Mlawer et al. 1997) are selected, as these are commonly-used WRF physics options. Initial and boundary conditions for the control run, and all subsequent experiment forecast, are provided by the GFS forecast initialized on 12 UTC May 19, 24 hours prior to the Nature Run. This also marks the beginning of the WRF Control Run. The reason for this is to ensure that the control run is sufficiently different from the Nature Run, as discussed in section 3.6. The Control Run is then run for 42 hours until May 21, 06:00 UTC.

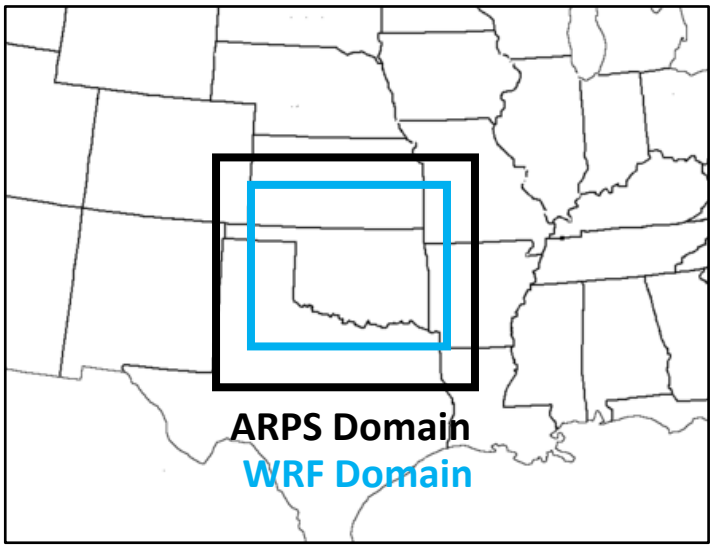

Figure 3.12: Spatial coverage of the ARPS domain (black) and WRF domain (blue).

3.6 Comparing the Control Run and Nature Run

An adequate control run will have a few key differences from the nature run. Since this study focuses on the initiation of convection across Southern Oklahoma, then an important key difference between the Control Run and Nature Run will be the placement, timing, and coverage of convective initiation. As previously discussed, the Nature Run contains discrete convective initiation between 1800 and 1900 UTC across southern

Oklahoma south and west of Oklahoma City. This convection is largely absent in the Control Run (figure 3.13a) with convective initiation not occurring until 2200 UTC to the north and east of Oklahoma City (figure 3.13b). The ability of the simulated observations to correct these spatial and temporal errors regarding CI will be a key area to watch in evaluating the OSSE.

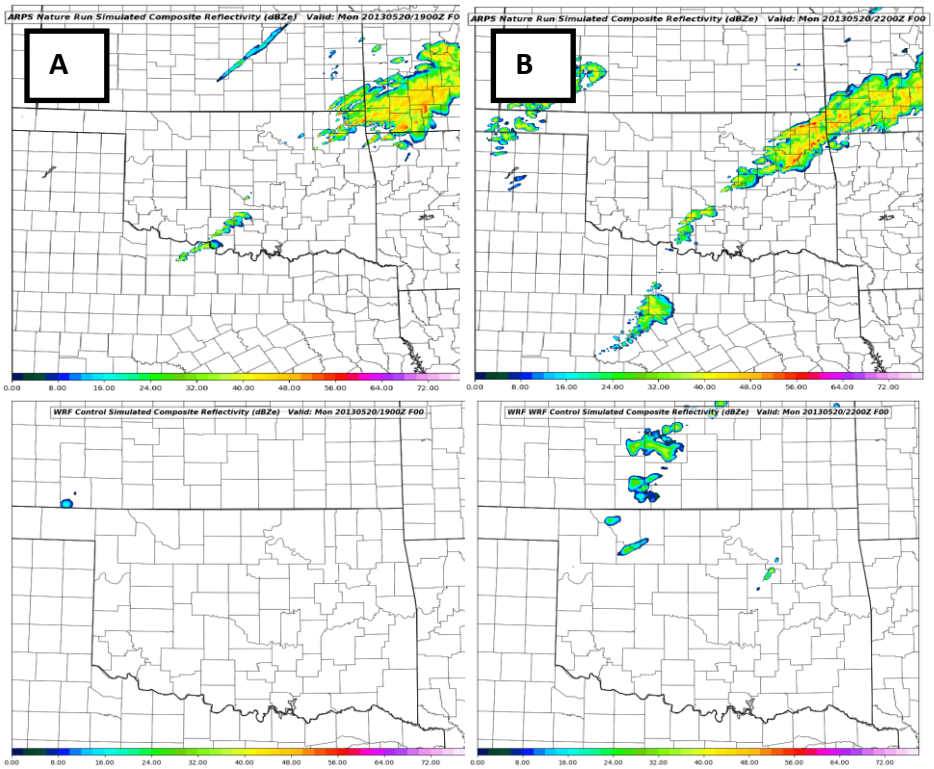

Figure 3.13: Comparison between modeled composite radar reflectivity in the Nature Run (top) and the WRF Control (bottom). Images are valid at 19 UTC (A) and 22 UTC (B) on 20 May, 2013.

A qualitative metric for assessing the difference between the Nature Run and the Control Run involves using the root mean squared error (RMSE). Figure 3.14 shows RMSE for surface pressure, temperature, dewpoint, and both wind components. These RMSE values indicate sufficient differences between the Nature Run and Control Run based off control RMSE values used in previous mesoscale OSSE studies (Gasperoni et al. 2013, Liu et al. 2009, Tong and Xue 2005). With a control run that is sufficiently different from the Nature Run any improvements in the OSSE forecast experiments can be attributed to the impacts of the synthetic observations.

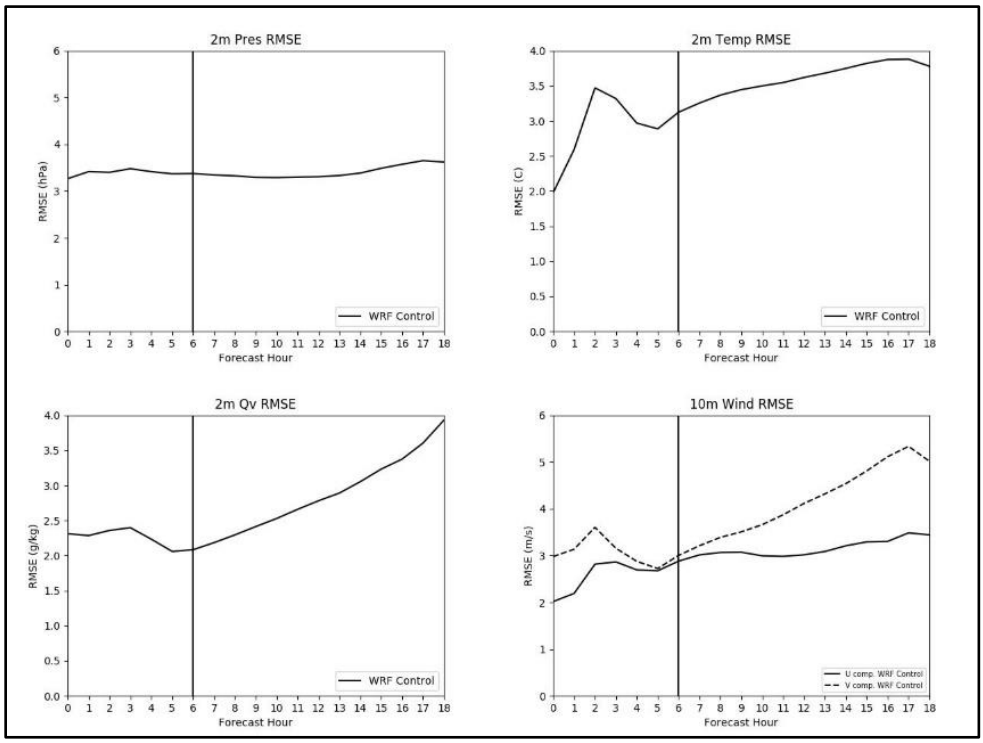

Figure 3.14: RMSE values between 12 UTC 20 May 2013 to 06 UTC 21 May 2013 from the WRF Control run.

3.7 WRF OSSE Experiments

In most OSSEs, the design and characteristics of the proposed observing system have already been established, but occasionally there is opportunity to investigate the characteristics and configuration of an observing system that, if implemented, could result in significant forecast improvements. In this study, experiments are not only performed on the current vision of the 3-D Mesonet but are also carried out to identify the optimal configuration of the network that will yield the most significant improvements to a short term convective forecast. A graphical interpretation of the OSSE system described here is given in Figure 3.15.

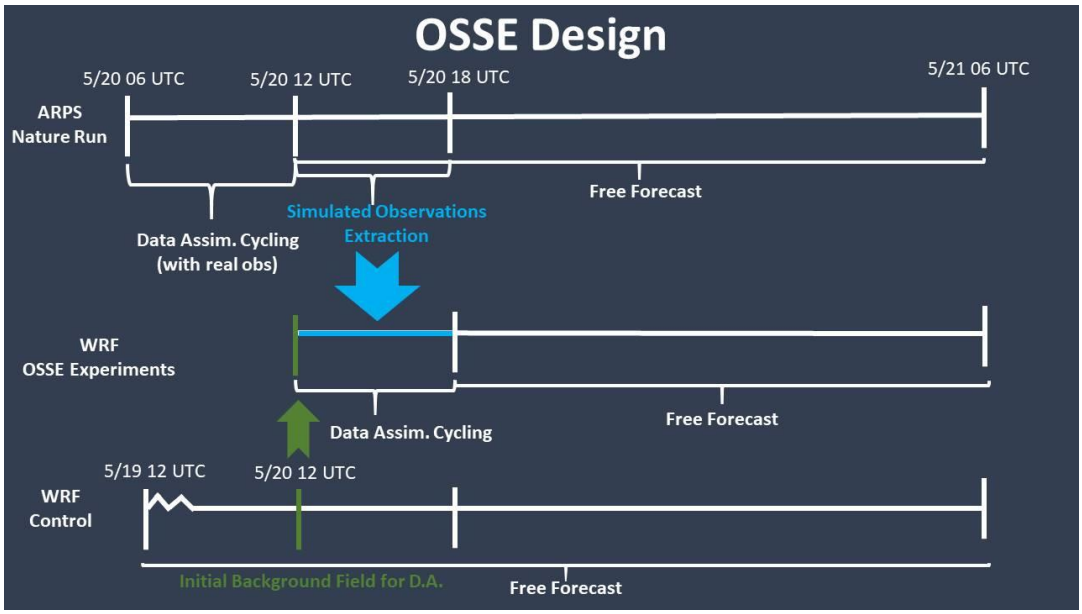

Figure 3.15: A graphical interpretation of the UAV OSSE system.

Prior to performing any experiments with the simulated CopterSonde observations, an initial experiment is performed where only the simulated FNL and

Oklahoma Mesonet observations are input into the WRF forecast. This serves two purposes. The first is to investigate the impact of assimilating simulated observations from the current observing network. Ideally, the impacts from assimilating synthetic observations from current observing networks should result in a positive adjustment from the Control Run toward the Nature Run and mimic the impacts of assimilating real observations into an operational data assimilation system. This would indicate that the data assimilation system is giving realistic results. The second purpose is to provide a baseline for comparing experiments containing the UAV observations. Since comparing the results from the OSSE experiments to the Control Run would lead to overly optimistic conclusions, the results are instead compared to a WRF based on today's complete suite of available observations. Making improvements to this forecast is much more challenging and provides a more realistic assessment of the magnitude 3-D Mesonet observations could have on NWP.

In order to allow for this comparison, each of the 3-D Mesonet OSSE experiments contains the synthetic observations from current observing networks (FNL and Mesonet). The first series of 3-D Mesonet experiments will focus on identifying the optimal maximum flight level for the UAV. In these experiments, hourly flights from 110 Mesonet sites (Figure 2.1) are launched to a designated flight level. These flights begin prior to the top of the hour according to the expected flight duration (for example, a flight that is expected to last 15 minutes will launch 15 minutes prior to the top of the hour so that, as in the tradition of radiosonde launches, the data are considered valid at the top of the hour. These experiments do not take into account the time needed for the transmission of data from the launch site to the central data collection site. Experiments at designated

maximum flight altitude (MFA) begin at 3 km AGL, stepping down to 2 km, 1 km, and 400 feet (123 m), the currently allowed MFA.

Once the most impactful UAV MFA is identified, the second series of experiments will use this ideal flight level and begin varying the number of stations to identifying the minimum number of stations necessary to maintain the same impact on the forecast. While initially all 110 3-D Mesonet sites are included, this number is reduced with each experiment to 75, 50, 25, and 10 sites. It could be argued that this set of experiments holds the most value for designing and building a UAV network. Identifying the required number of stations prior to the implementation of the UAV network could save a considerable amount of money that would have otherwise been placed into stations that added little additional value to the forecast. Initial conditions for each of the OSSE forecast experiments comes from the 24-hour forecast output field from the WRF Control run at May 20 at 12:00 UTC. Lateral boundary conditions for each experiment come from the same GFS forecast used in the WRF Control run with a 3-hourly interval.

Through these experiments the ideal UAV observing network configuration can be identified. The benefits from this information not only include saving money, time and other resources, but will play a role in planning future UAV network configurations. However, since this “ideal” system ignores several regulatory and technological limitations (such as data transmission and quality checks processes), it must be acknowledged that the forecast impacts from the idealized system are likely an optimistic outcome. But, this will give a benchmark for which the UAV network can aspire to during implementation and can help highlight the need for adjustments in current UAV technology and regulation.

3.8 Results

3.8.1 Maximum Flight Altitude

3.8.1.1 Composite Reflectivity Comparison

Composite reflectivity is used in order to reveal all convective precipitation generated by the numerical models and give a better estimate of when convective initiation began. Figures 3.16 through 3.22 compare composite reflectivity fields from both the Nature Run, WRF Control run, and all OSSE experiments from 18 UTC through 21 UTC in half hour increments. This time period is highlighted since capturing the convective initiation observed in the Nature Run is one of the primary goals of this OSSE.

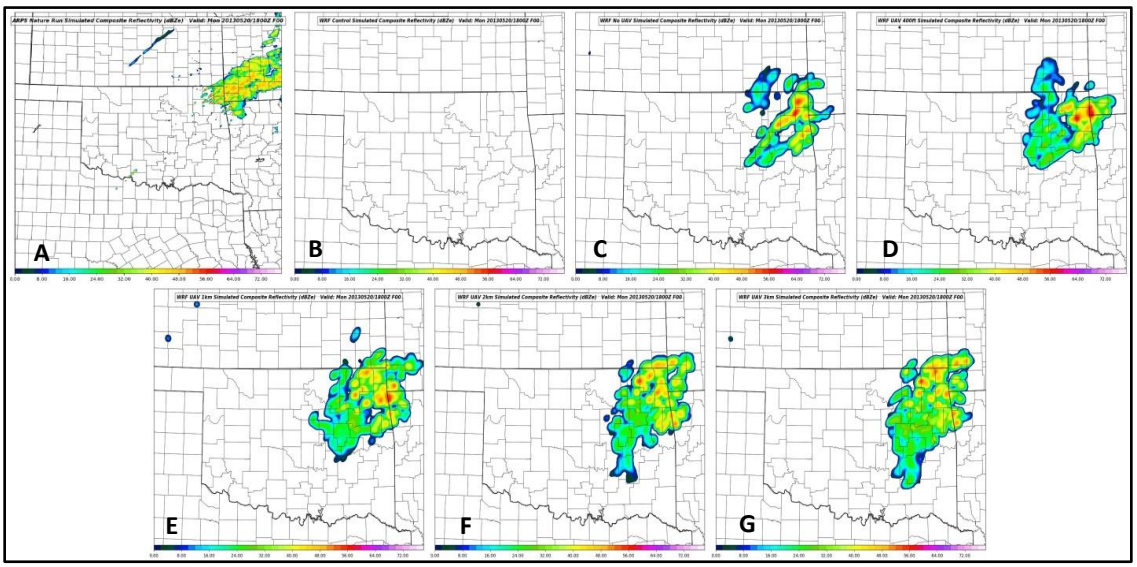

Figure 3.16: Comparison between modeled composite radar reflectivity between the Nature Run (A), WRF Control (B), No UAV (C), UAV 400ft (D), UAV 1km (E), UAV 2km (F), and UAV 3km (G) at 1800 on 20 May 2013.

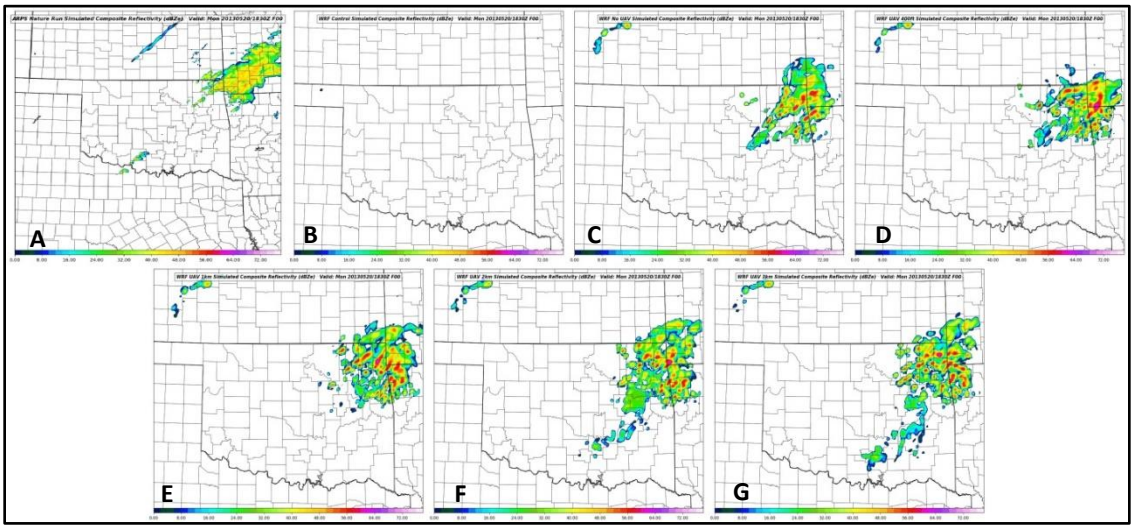

Figure 3.17: Comparison between modeled composite radar reflectivity between the Nature Run (A), WRF Control (B), No UAV (C), UAV 400ft (D), UAV 1km (E), UAV 2km (F), and UAV 3km (G) at 1830 on 20 May 2013.

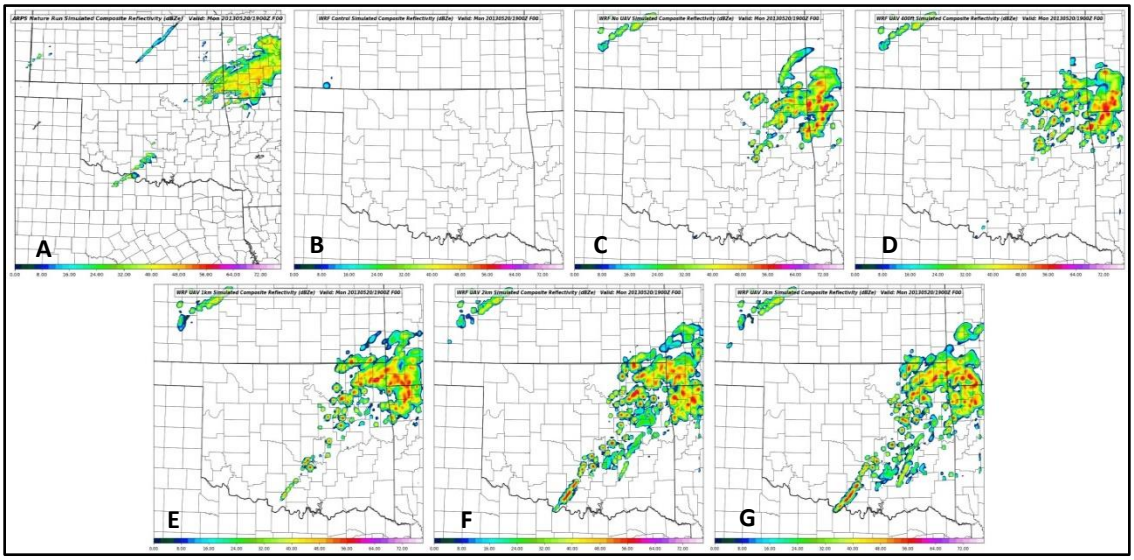

Figure 3.18: Comparison between modeled composite radar reflectivity between the Nature Run (A), WRF Control (B), No UAV (C), UAV 400ft (D), UAV 1km (E), UAV 2km (F), and UAV 3km (G) at 1900 on 20 May 2013.

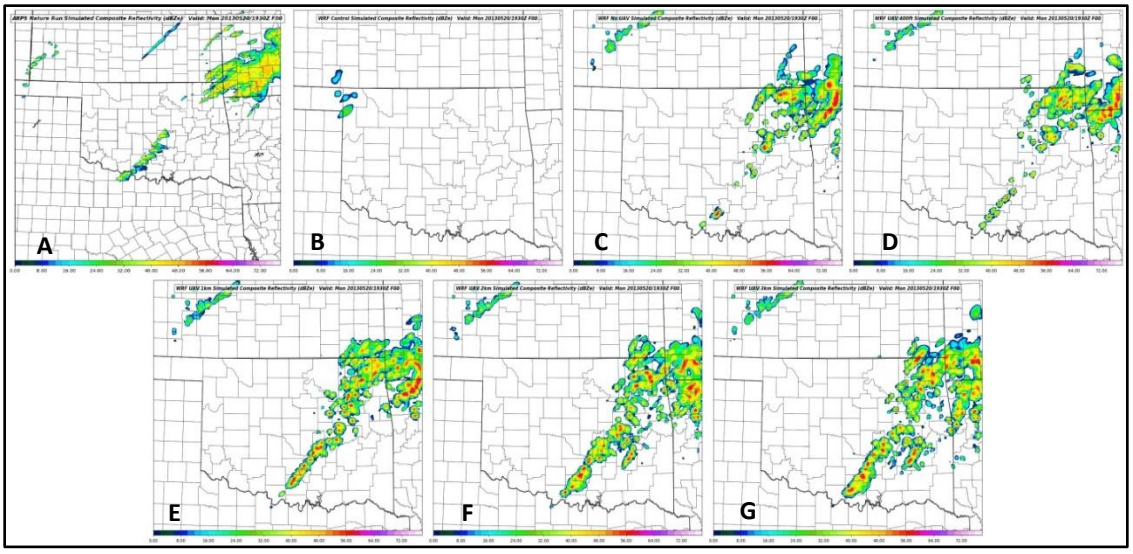

Figure 3.19: Comparison between modeled composite radar reflectivity between the Nature Run (A), WRF Control (B), No UAV (C), UAV 400ft (D), UAV 1km (E), UAV 2km (F), and UAV 3km (G) at 1930 on 20 May 2013.

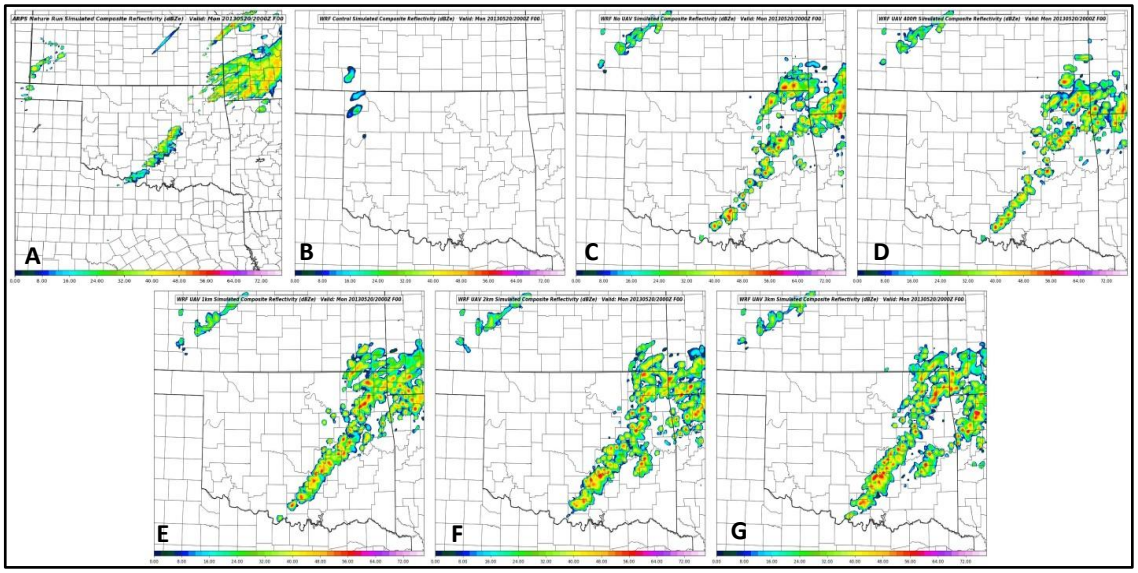

Figure 3.20: Comparison between modeled composite radar reflectivity between the Nature Run (A), WRF Control (B), No UAV (C), UAV 400ft (D), UAV 1km (E), UAV 2km (F), and UAV 3km (G) at 2000 on 20 May 2013.

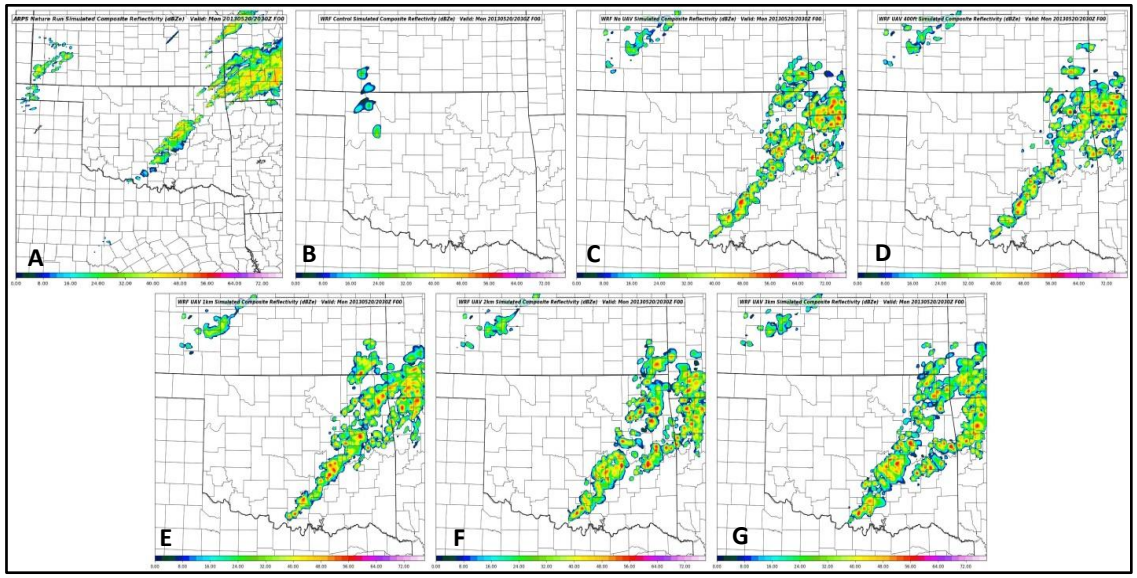

Figure 3.21: Comparison between modeled composite radar reflectivity between the Nature Run (A), WRF Control (B), No UAV (C), UAV 400ft (D), UAV 1km (E), UAV 2km (F), and UAV 3km (G) at 2030 on 20 May 2013.

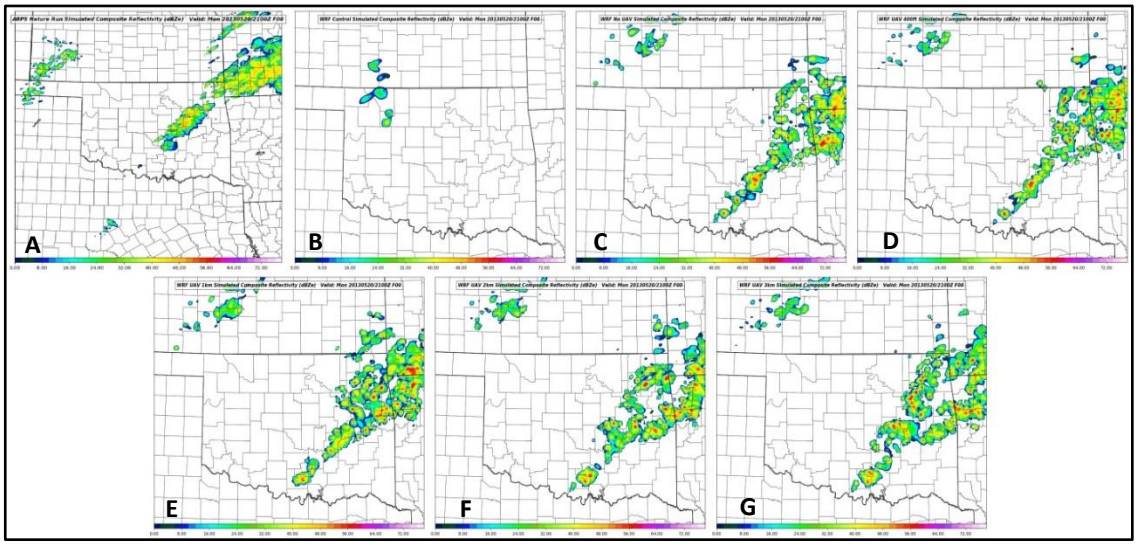

Figure 3.22: Comparison between modeled composite radar reflectivity between the Nature Run (A), WRF Control (B), No UAV (C), UAV 400ft (D), UAV 1km (E), UAV 2km (F), and UAV 3km (G) at 2100 on 20 May 2013.

At 18 UTC the value of assimilating data from the current observing networks can be observed as warm frontal convection and precipitation across northeast Oklahoma that is largely missing from the WRF Control is restored in this simulation. This is a positive indicator that the OSSE design is functioning properly as the addition of simulated observations from the current observing network produces an impact that is similar to what is observed in operational short-term NWP. This region of precipitation is similarly input into the WRF simulations with the inclusion of all UAV data sets.

Noticeable differences between the UAV and "No UAV" forecast start to become apparent one hour into the free forecast at 1900 UTC (Figure 3.18) when convective initiation begins across south central Oklahoma in the 1, 2, and 3 km UAV forecasts. This CI follows closely with the Nature Run, which also shows CI across south central Oklahoma just 30 minutes prior at 1830 UTC. One notable difference between the three UAV forecasts producing CI is that the 2 km and 3 km forecasts initially produce storms with a linear structure. The 1 km forecast produces more discrete convection, but this appears less robust than the convection present in the 2 km and 3 km forecasts as well as the Nature Run.

The 400 ft UAV and "No UAV" forecast follows suit 30 min later at 1930 UTC (Figure 3.19). However, the "No UAV" forecast is only able to produce a single dominant cell with areas of weaker reflectivity in the vicinity across south central Oklahoma. At this time the 1-, 2-, and 3-km MFA UAV forecasts show their convection growing as they propagate northeastward. It should be noted that the convective storms in the 2 and 3 km forecasts now take on a more discrete appearance such as the storms present in the Nature Run.

By 2000 UTC all WRF forecasts except for the WRF Control run show convective storms across south central Oklahoma similar to those present in the Nature Run (Figure 3.20). Unlike the UAV experiments, the "No UAV" experiment shows the fewest convective cells and least development in those cells. While this is likely due in part to its later initiation of convection, it contains weaker convection than the similarly-timed 400 ft experiment. This suggests that the addition of even low-level UAV data can have a positive impact on the short term forecast. However, it should be noted that the 1-, 2-, and 3-km MFA UAV forecasts show a nearly continuous line of precipitation interspersed with small convective cells. This is in contrast to the Nature Run, which shows a distinctive gap between the convective cells across south central Oklahoma that initiated along the dryline and the region of warm frontal precipitation to the north east. Similar trends can be observed in the "No UAV" and 400 ft forecasts during the 2030 and 2100 UTC periods. By 2100 UTC (Figure 3.22) there is little differentiation between all WRF forecast experiments besides the exact placement of individual convective elements, and it is very hard to draw decisive conclusions on the improvements of the WRF forecasts from any experiment beyond 3 h of free forecast.

But this should not undermine the significance of the short-term value added by the UAV observations to the WRF forecast. Assimilating at least 1 km of UAV data or more allowed for better timing of CI as well as a quicker convective growth as compared to the "No UAV" and 400 ft experiments.

3.8.1.2 Surface RMSE Comparison

Figure 3.23 shows the root mean squared error (RMSE) associated with four different surface fields (surface pressure, 2m temperature, 2m mixing ratio, and 10 m U

and V wind components) (mean surface bias plots can be found in the appendix). In all fields except surface pressure, the value of the UAV data can be observed. For example, the surface mixing ratio RMSE shows a noticeable decrease during the data assimilation period as the UAV data are assimilated. Similar benefit can be seen in the temperature field as the addition of the UAV observations helps generate not only a better surface temperature analysis but also a better short-term forecast. A few hours into the free forecast the impacts of different convective processes becomes apparent as the RMSE values begin to diverge somewhat.

Although not as clear as the temperature and mixing ratio signals, surface U and V wind components demonstrate some improvement to the analysis as well as the first 1 to 2 hours of the free forecast. However, the impacts of convection on these fields is much higher than the thermodynamic fields and is apparent after the first few hours of the free forecast as the RMSE spread beings to increase. Additionally, the low-level winds are more susceptible to influence by the WRF's PBL scheme selection. The MYNN scheme may induce more vertical mixing of the PBL winds and allow for higher surface winds than in the ARPS. This point is discussed further in section 4.1.2.

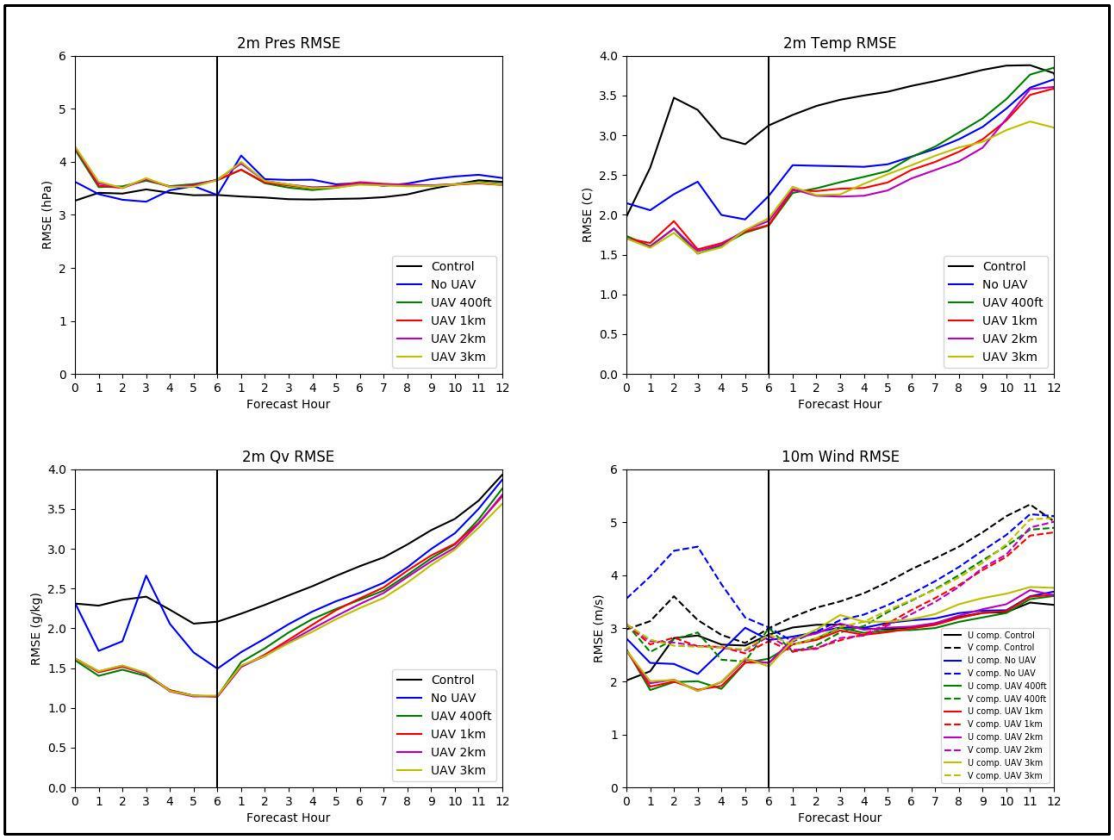

Figure 3.23: RMSE plots during the data assimilation cycling period (left of the vertical black line) and during the free forecast period (right of the black line) for surface pressure (upper left), 10 m U and V winds (upper right), 2 m mixing ratio (bottom left), and 2 m temperature (bottom right).

The surface pressure field is the only variable to not demonstrate an improvement to the analysis, though this result may be misleading. Upon closer inspection of the surface pressure field at 1800 UTC (figure 3.24) the Nature Run contains a well-defined surface trough that is largely over-deepened in the WRF control run. While the addition of current observing network data helps correct this low-pressure bias considerably, the "No UAV" analyzed surface pressure field lacks the clear structure of the Nature Run. Some of this trough structure information is brought back into the analysis by the UAV

observations. However, in some areas of the UAV analysis the surface pressure is analyzed too high compared to the Nature Run such as in northwest Oklahoma and in far southeast Oklahoma. So even though the overall structure of the surface trough is improved with the assimilation of UAV observations, over correction of the WRF Control low bias results in worse than expected RMSE values.

It is also apparent that the additional depth of UAV observations have little impact on the surface analysis. The RMSE results from all four surface fields show that there is little difference between the addition of 400ft or 3 km of UAV observations. This result is not surprising since only data in the lowest few hundred feet will cause any impact to the surface analysis. The depth of observations that impact the surface analysis can be adjusted by selecting a larger vertical influence radius in the data assimilation step of the OSSE. While adjusting this parameter may reveal a more meaningful impact of the 1, 2, and 3 km UAV observations, it is not explored here.

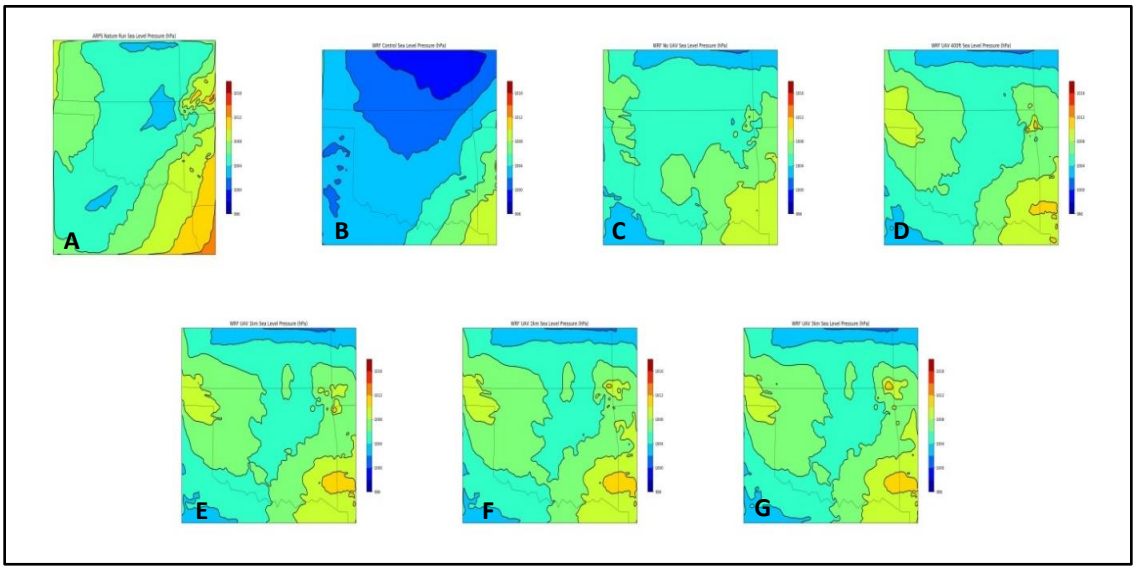

Figure 3.24: Mean Sea Level Pressure (MSLP) comparisons between the Nature Run (A), WRF Control (B), No UAV (C), UAV 400ft (D), UAV 1km (E), UAV 2km (F), and UAV 3km (G) forecasts at 1800 UTC.

3.8.1.3 Vertical Profile Comparison

In order to see the impact of the 1-, 2-, and 3-km MFA UAV observations vertical profiles of temperature, dewpoint, wind speed and direction are investigated. Vertical profiles below 500 mb were taken from the Nature Run, the WRF Control run, and all WRF experiments from the OUN radiosonde release location in Norman, Oklahoma. This location was chosen due to its close proximity to the convective initiation present in the Nature Run (as well as WRF experiments) and because this location is in between nearby UAV launch sites and GFS FNL insertion points (note that the Norman, OK Mesonet site was not used as a UAV launch location due to its co-location with an airport). Choosing a location for profile sampling too close to a UAV or FNL data point would likely skew the profiles in favor of one dataset or the other.

These vertical profiles of the MFA experiment analyses are given in Figure 3.25 with vertical analysis errors displayed in figure 3.26. In both figures the impacts of adding UAV moisture observations to the DA process can be observed as the 3 km analysis captures the Nature Run's moisture profile the best below 800 hPa. While the 400 ft UAV experiment does show improvements to the low-level moisture field, the profile quickly returns to the "No UAV" profile as data from the current observing networks dominates the analysis. Adding additional UAV observations incrementally improves the quality of the moisture profile analysis particularly in the low to mid-levels of the boundary layer with the addition of 2 or 3 km of UAV data. This can be seen as the 1 and 2 km gradually drift away from the Nature Run and toward the "No UAV" moisture plot.

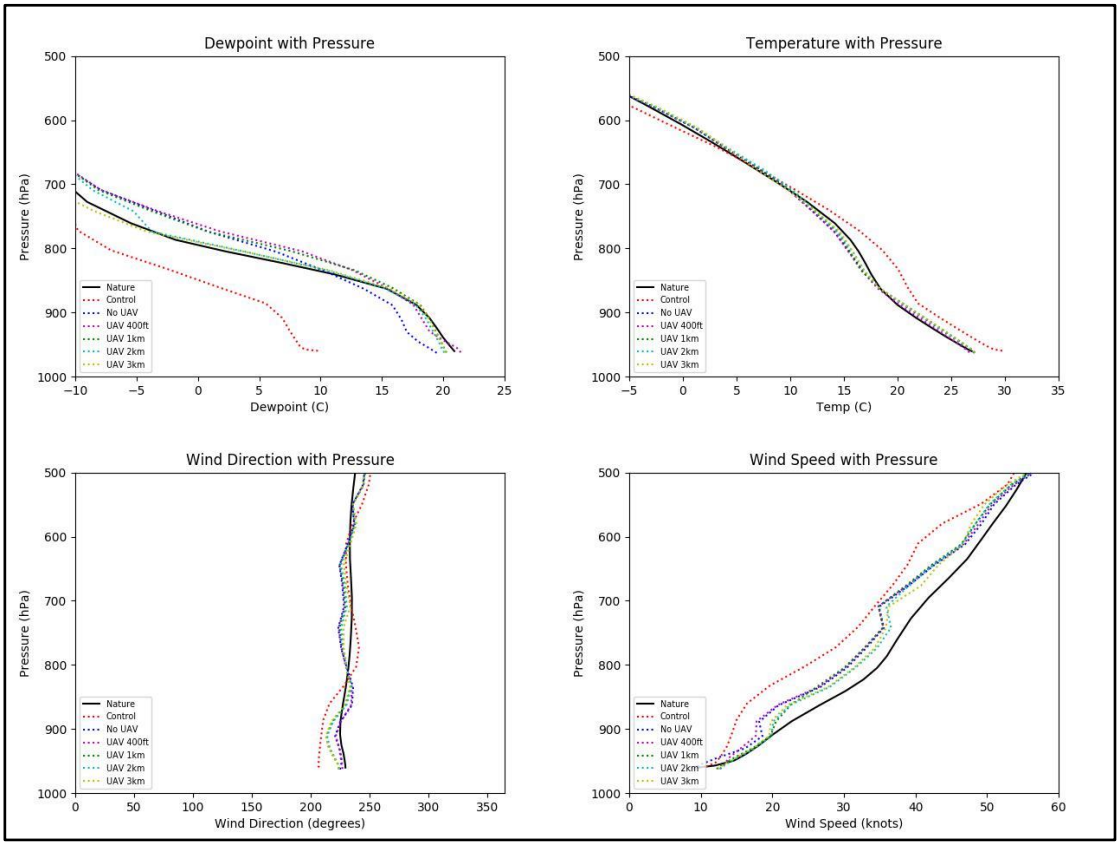

Figure 3.25: Vertical profiles below 500 hPa of dewpoint (upper left), temperature (upper right), wind direction (bottom left), and wind speed (bottom right) valid at the analysis time of 1800 UTC.

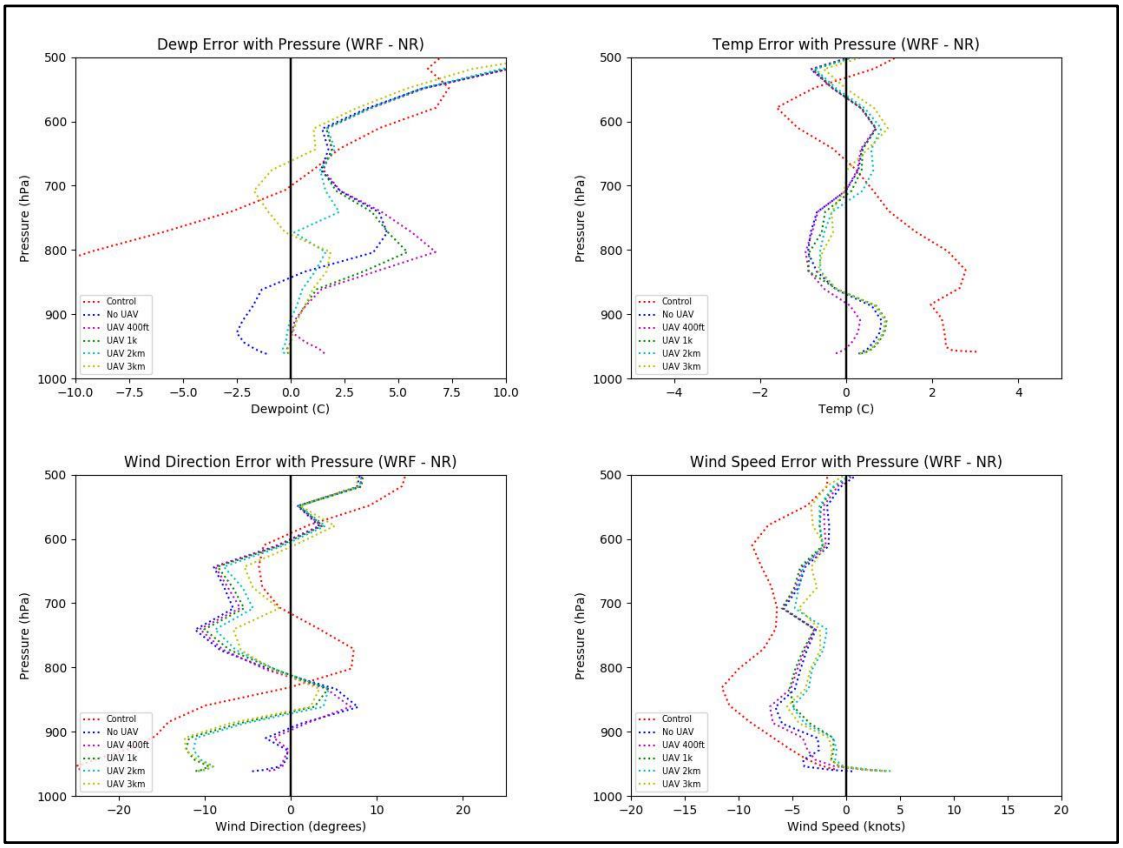

Figure 3.26: Vertical analysis error profiles below 500 hPa valid at 1800 UTC for the Maximum Flight Altitude tests.

Improvements to the 1800 UTC analysis can also be readily observed in the wind speed profiles (figure 17). Besides a nearly 2.6 ms^{-1} (5 kt) high bias in the near surface wind speed, the value of the UAV observations is seen in the low- to mid-levels and the wind analyses are brought closer to the Nature Run. As in the moisture profiles, the wind speed profiles quickly revert back to the "No UAV" experiment profiles as the FNL upper air observations dominate above the top of the UAV flight level. This directly shows the benefit of the extra depth of UAV observations. However, this benefit does not appear to carry over in the wind direction analysis as the addition of UAV data does not show any

strong signals of height dependency and only improves the analysis near the 850 – 700 hPa layer.

Assimilating UAV observations allows for only slight improvements in the temperature profile analysis when compared to the “No UAV” experiment. While the considerable improvement over the WRF Control run is a signal that increases confidence in the validity of using the Mesonet and GFS FNL observations as proxies for all current observing networks, the impact of the UAV observations is confined to a small layer near 800 mb during the 3-km UAV experiment. The reason for this limited improvement is likely because the “No UAV” experiment already creates a close representation of the Nature Run with low level temperature errors near +/- 1 C. This shows that there is less error to correct as compared to the other fields. The main improvement gained by adding UAV observations comes from better resolving the mid-level lapse rates. Figure 3.26 shows this improvement well as the 3-km UAV analysis has less analysis error than the other experiments in the 850 – 750 layer. Although the 400-ft UAV analysis appears to have a better handle on the low level lapse rates, it is not clear if this is a true signal or due to noise in the low-level temperature fields.

3.8.1.4 Cross Section Comparison

One of the main objectives of the 3-D Mesonet is not only to improve observations of the boundary layer, but to also promote better analysis of the boundary layer in NWP. Added benefit from the addition of the UAV data can be determined through inspection of cross sections through the PBL. The cross section line (Figure 3.27) was chosen such that dryline details can be observed in each model run. Only the bottom 4 km AGL of the boundary layer are displayed since the deepest UAV dataset only extends up to 3 km

AGL. While a few minor variations may exist above 4 km due to vertical influence of the 3 km UAV data, all substantial differences between the forecast fields are expected below this 4 km ceiling. Cross sections of mixing ratio and equivalent potential temperature (theta-e) are taken since both variables are conserved values for an air mass (assuming no phase changes occur to influence the mixing ratio values).

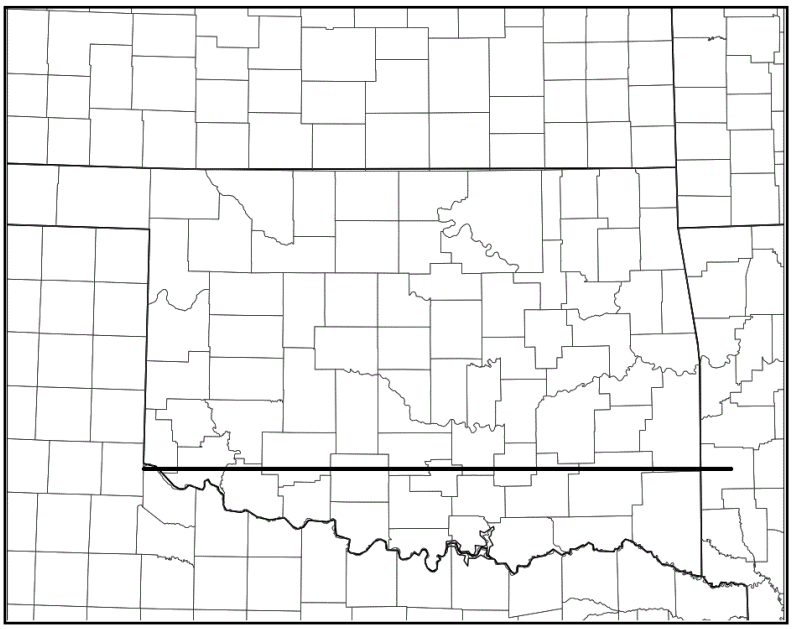

Figure 3.27: The black line shown here on the WRF domain represents the sampling location for the cross-section analyses.

3.8.1.4.1 Mixing Ratio Cross Section Comparison

The cross sections of mixing ratio at the analysis time of 1800 UTC show distinguishing differences between the WRF experiment forecasts (Figure 3.28). Cross sections of mixing ratio through the Nature Run reveal a dome-like moist layer beneath 2 km characterized by mixing ratios of 12 g/kg or greater with a maximum of 16 – 18 g/kg below 1.2 km and centered across southern Oklahoma (approximately between -95.4˚ and -97.5˚). Although a dryline can be seen between roughly -97.4˚ and -98.0˚

degrees, the tightest moisture gradient is observed above the surface dryline between 1 and 2 km MSL. The WRF control run, and similarly the “No UAV” experiment, analyzed a layer of boundary layer moisture that is much shallower compared to the Nature Run with mixing ratio values of 12 g/kg found well below 1.5 and 2 km MSL respectively. However, the “No UAV” experiment did improve the analysis by capturing the “dome” shape of the richer boundary layer moisture below 2 km.

Further improvements to the boundary layer moisture analysis are made with the addition of the UAV observations. The 400 ft UAV experiment introduces more moisture into the analysis with a region of mixing ratios in the 16 – 18 g/kg range in roughly the same location as the Nature Run. This improvement is likely due to the higher spatial frequency of the UAV observations that were able to capture this moist layer better. However, the overall depth of the moisture layer (here defined as where mixing ratios are 12 g/kg or greater) does not change significantly. This is an expected result from the 400 ft experiment since the low-level observations do not sample the full depth of this moist layer, and therefore mirror the “No UAV” analysis above the lower levels.

However, the 1-, 2-, and 3-km UAV experiments do sample most, if not all, of this moist layer, and this added information is reflected in the analyses. The 1-km UAV analysis begins to show a more “dome” like shape to the region of higher mixing ratios as in the Nature. These details are further refined is the 2- and 3-km UAV analysis as the moist layer takes on more characteristics of the moist layer in the Nature Run including removing a region of dry air and increasing the moisture gradient between 1 – 2 km MSL (Figure 3.28). One notable difference between the 2- and 3-km UAV experiments are the slight ripples in the tight moisture gradient between 1 and 2 km MSL. It is difficult to

determine if this is due to noise accumulation through the data assimilation cycling or if it is due to analyzed precipitation ongoing in the vicinity of the cross section at 1800 UTC as seen in figure 3.18.

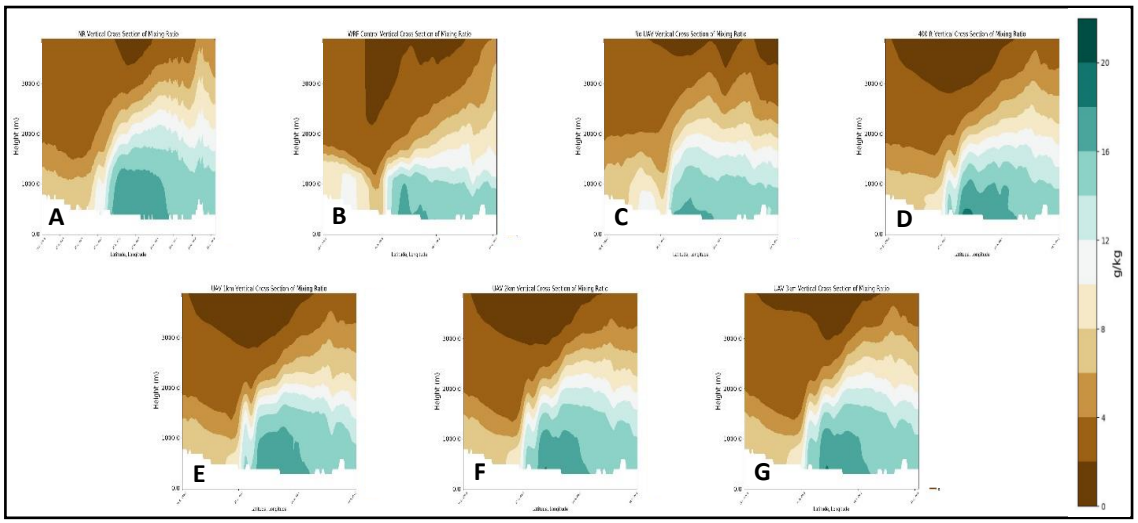

Figure 3.28: Cross section plots of mixing ratio from 0 to 4 km above MSL for the Nature Run (A), WRF Control (B), No UAV (C), UAV 400ft (D), UAV 1km (E), UAV 2km (F), and UAV 3km (G) WRF analyses valid at 1800 UTC 20 May 2013.

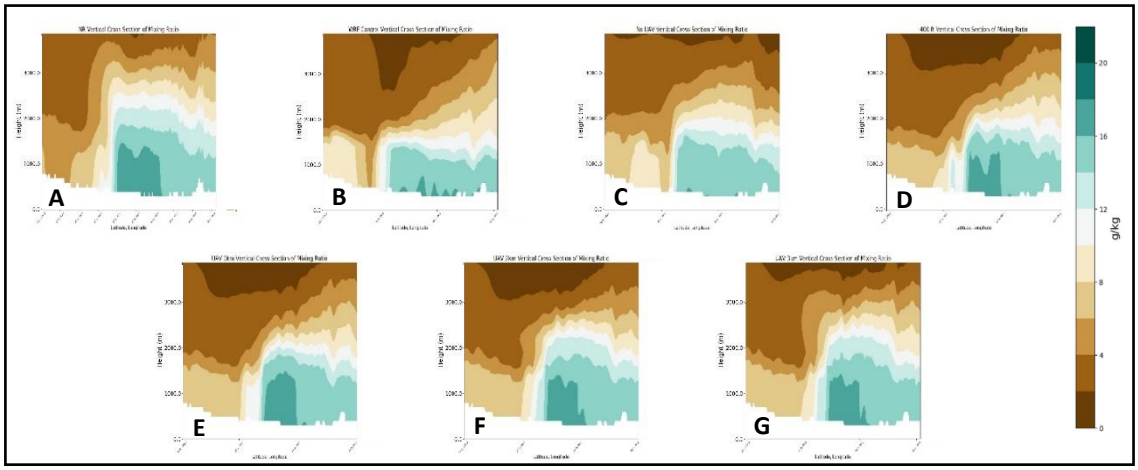

Figure 3.29: As in figure 20, except cross sections are valid at 1900 UTC.

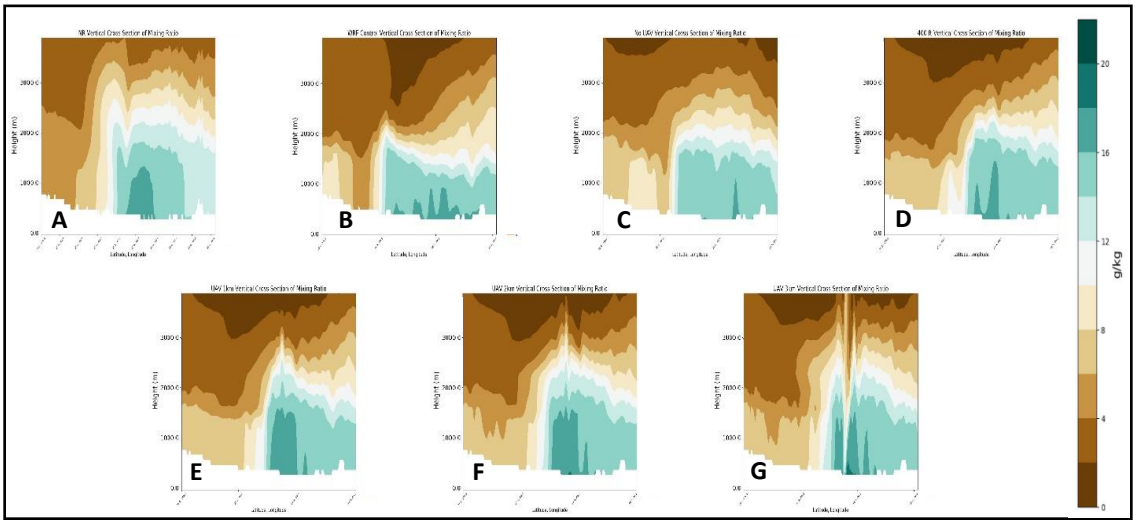

Figure 3.30: As in figure 20, except cross sections are valid at 2000 UTC.

One hour into the WRF experiments' free forecasts the impacts of the UAV observations can still be observed (Figure 3.29). While the "No UAV" forecast has lost all mixing ratios greater than 16 g/kg, all UAV forecasts maintain higher moisture values in accordance with the Nature Run. This loss of moisture can also be observed in surface dewpoint fields at 1800 and 1900 UTC (Figures 3.31 and 3.32). Although all analyses begin with similar dewpoint fields at 1800 UTC, one hour into the free forecast the No UAV forecast dries out across south central Oklahoma while moisture is maintained in this region with the addition of more UAV observations. The greater low- to mid-level moisture added by the UAV observations is likely helping keep surface dewpoints high as boundary layer mixing occurs.

Additionally, broad lifting can be observed in the Nature Run as the moist layer begins to deepen above 2 km MSL. This lifting can also be observed in the 2- and 3-km UAV experiments as their respective moist layers increase in height above the 2 km MSL level. This effect can also be observed to a lesser degree in the 1 km UAV forecast. This

result is consistent with the early CI that begins around 1900 UTC in the 1, 2, and 3 km UAV forecasts.

By 2000 UTC the lift can be observed in the WRF Control and "No UAV" experiment, while convective processes begin to dominate in the Nature Run and UAV forecasts (Figure 3.30). This is readily apparent in the 2- and 3-km UAV forecasts as narrow upward (downward) plumes of moist (dry) air are seen indicating potential updrafts (downdrafts). However, the increased moisture inserted by the UAV observations maintains through the first two hours of all UAV forecasts as in the Nature Run. It should also be noted that the 400 ft UAV experiment does compare fairly well to the moist layer structure observed in the Nature Run in both the first and second hours of the free forecast (1900 and 2000 UTC). While this may be an encouraging sign, it is not clear whether this is a strong indicator of forecast skill.

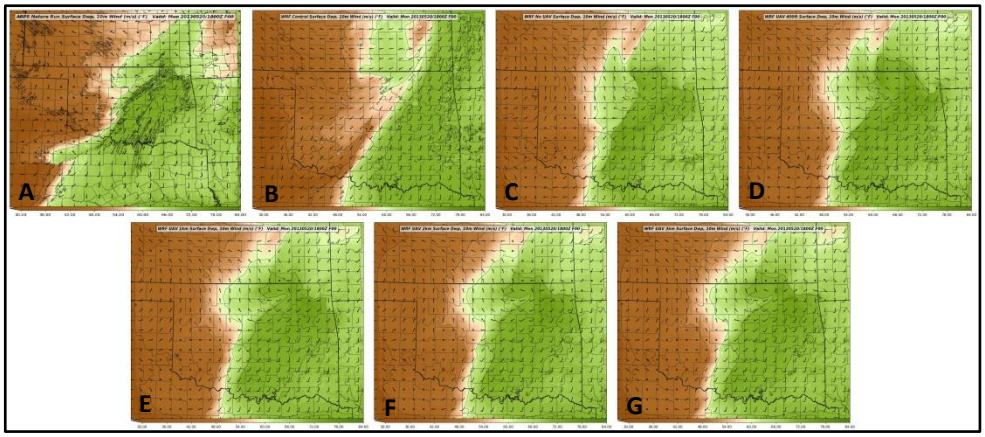

Figure 3.31: 1800 UTC analysis of 2m dewpoint for the Nature Run (A), WRF Control (B), No UAV (C), UAV 400ft (D), UAV 1km (E), UAV 2km (F), and UAV 3km (G).

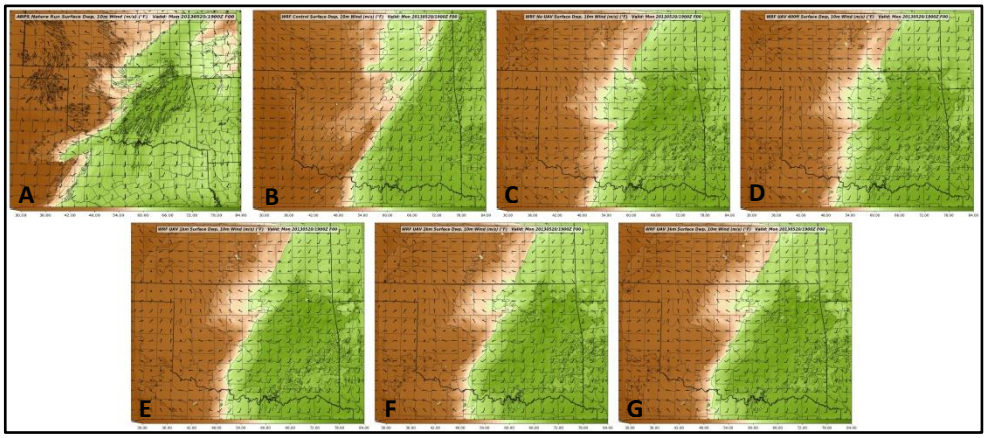

Figure 3.32: One hour 2m dewpoint forecast valid at 1900 UTC for the Nature Run (A), WRF Control (B), No UAV (C), UAV 400ft (D), UAV 1km (E), UAV 2km (F), and UAV 3km (G) forecasts.

3.8.1.4.2 Equivalent Potential Temperature Cross Section Comparison

Similar to the cross sections of mixing ratio, cross sections of theta-e are used to analyze and highlight improvements in the final analysis of the WRF experiments at 1800 UTC and through the first two hours of the free forecast through CI. Since theta-e is dependent on moisture content the cross sections of theta-e are similar to the mixing ratio cross sections but highlight subtle differences in the boundary layer temperature and structure (Figure 3.33).

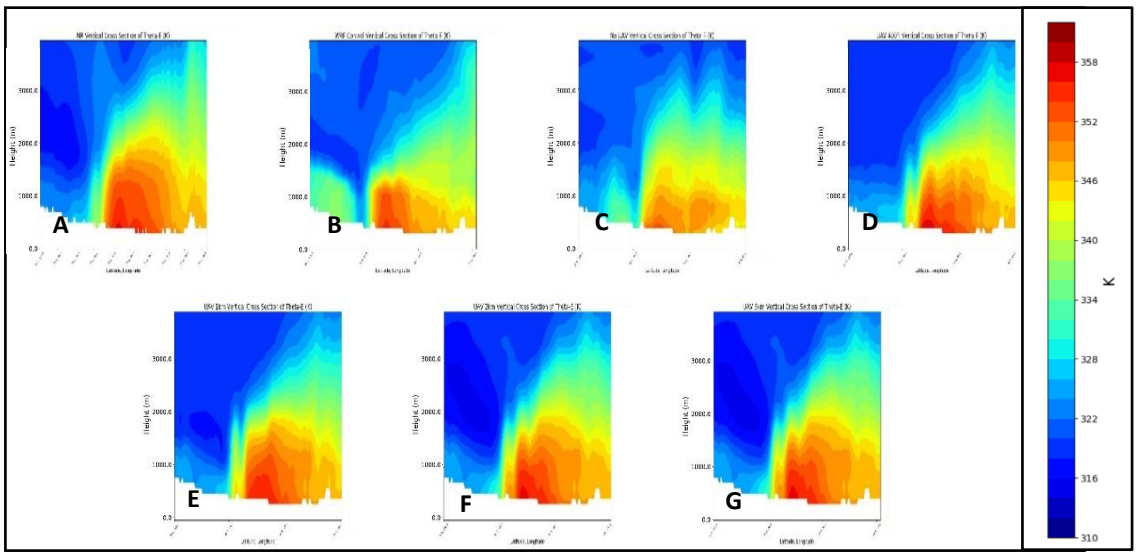

Figure 3.33: Cross section plots of theta-e from 0 to 4 km above MSL from 0 to 4 km above MSL for the Nature Run (A), WRF Control (B), No UAV (C), UAV 400ft (D), UAV 1km (E), UAV 2km (F), and UAV 3km (G) WRF analyses valid at 1800 UTC 20 May 2013.

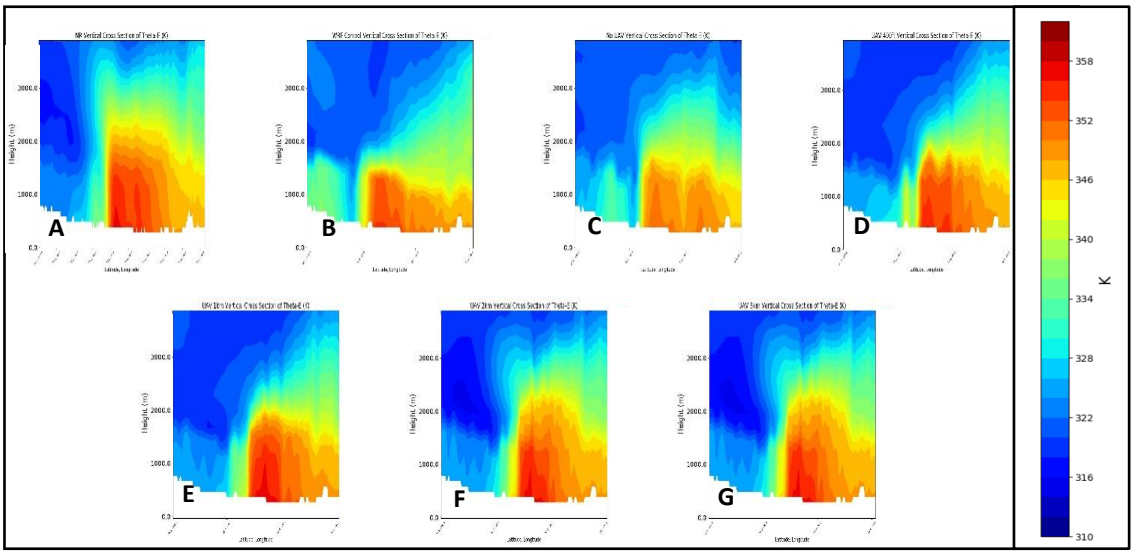

Figure 3.34: As in figure 25 except representing a one hour forecast of theta-e cross section valid at 1900 UTC 20 May 2013.

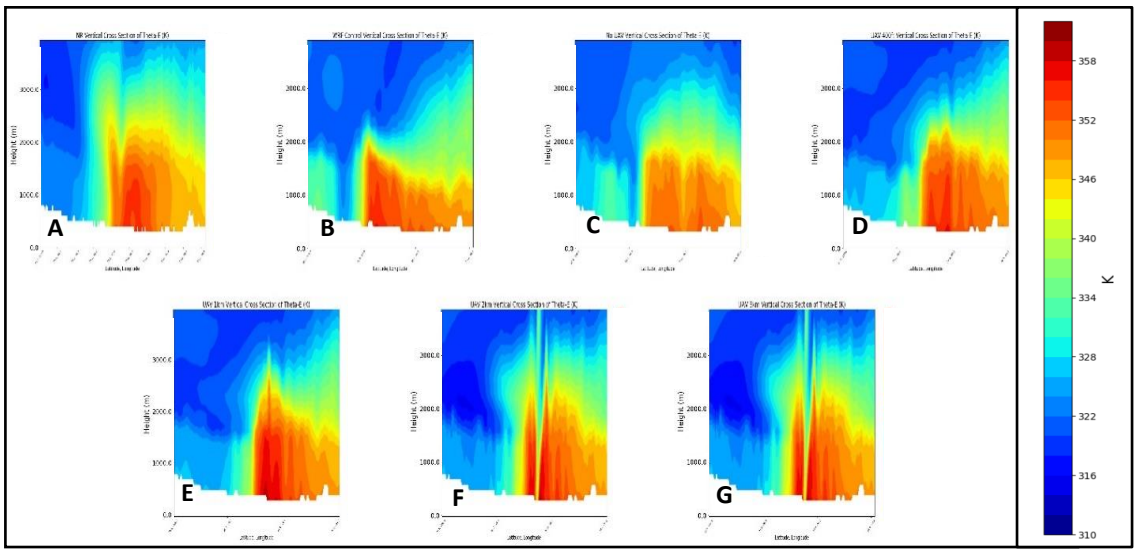

Figure 3.35: As in figure 25 except representing a two-hour forecast of theta-e cross section valid at 2000 UTC 20 May 2013.

For example, the Nature Run theta-e cross section at 18 UTC reveals a similar "dome" appearance to the higher theta-e air mass beneath 2 km MSL, but also reveals a small, secondary vertical plume of 354 K theta-e values as well as better detail in the thermal structure above the higher theta-e values at the surface. As in the mixing ratio cross sections, the WRF Control run captures the higher theta-e values near the surface but maintains a shallow layer of richer boundary layer air. The addition of data in the "No UAV" experiment corrects this shallow boundary layer but washes out the higher values near the surface. However, this data information is captured by the UAV observations and re-inserted into the 1800 UTC analysis. The inclusion of all UAV data helps resolve the Nature Run's "dome" shape as well as re-introduces the subtle secondary elongation of higher theta-e values near the surface in all UAV analyses except for the 1 km UAV analysis. The added benefit of the UAV observations is further demonstrated by comparing the 400-ft and 2-km analyses. In the Nature Run, the 344 K isotherm extends

2 km MSL. This information is not captured well by the 400-ft UAV analysis as the 344 K isotherm only reaches to nearly 1.5 km MSL but including 2- or 3-km UAV observations helps bring the 344 K isotherm to just under the 2 km MSL mark.

The higher theta-e air inserted into the analysis by the UAV observations maintains through the first hour of the free forecast and produces better boundary layer structure than the WRF Control and "No UAV" experiment by 1900 UTC (Figure 3.34). As with the mixing ratios, there is evidence of boundary layer lift as higher theta-e values begin to stretch upward in both the Nature Run and all WRF experiments. However, the UAV experiments, particularly the 3-km UAV experiment, demonstrate greater vertical elongation than the "No UAV" forecast. Although the theta-e gradient present in the Nature Run is not resolved well by any WRF forecast this is likely due to coarser WRF grid spacing. By 2000 UTC (Figure 3.35) the impacts of CI are evident in the 1-, 2-, and 3-km UAV forecasts as discussed with the mixing ratio cross sections. Although the higher theta-e values are maintained in all UAV forecasts, it is also noted that a warm bias is present near the surface in all UAV forecasts. By 2100 UTC convective influences begin to dominate in many of the cross sections, making comparisons difficult beyond this point.

3.8.1.5 Comparison of Convective Available Potential Energy (CAPE)

In order to gauge the value of the UAV observations on the analysis and short-term forecast over the entire domain as a whole it is beneficial to investigate meteorological parameters that encompass multiple components of the numerical environment. Two such parameters are convective available potential energy (CAPE) and convective inhibition (CIN) due to the fact that they incorporate information on both the

low-level temperature and moisture fields as well as information on lapse rates through the atmosphere. In this study, two forms of CAPE and CIN are inspected. The first is CAPE/CIN generate by lifting the most unstable parcel of air at each grid point (MUCAPE/MUCIN), and the second is mixed layer CAPE and CIN (MLCAPE/MLCIN). Here MLCAPE/MLCIN is calculated by averaging the CAPE/CIN values of all parcels within the lowest 100 hPa of the atmosphere at each grid point. Although MLCAPE/CIN is typically found by lifting a parcel using layer-averaged theta-e and q_v values, the formulation described here is substituted as a proxy for quick comparative purposes.

Figure 3.36 compares the MUCAPE field of the Nature Run to the WRF control and all WRF experiment 1800 UTC analyses. In the Nature Run's MUCAPE field this is a plume of higher MUCAPE values of 3.5 – 4.5 kJ/kg extending from central Oklahoma south/southwestward into northern Texas. This plume marks the edge of the most unstable air in close proximity to the dryline to the west where MUCAPE values decrease rapidly to zero and MUCIN increases. This zone of instability is present in a muted form in the WRF Control run with only 2 – 3 kJ/kg of MUCAPE and increased amounts of MUCIN across the domain. The assimilation of non-UAV observations improves this field across the domain as MUCAPE values increase to levels similar to the Nature Run. However, the highest MUCAPE values are displaced to the north and east with an additional region of higher MUCAPE across southeastern Oklahoma. Furthermore, the plume extending into Texas present in the Nature Run is not analyzed properly in the "No UAV" analysis. While this demonstrates that adding the current observing networks helps improve the analysis as in current operations, there is still room for improvement.

This improvement is provided by the assimilation of UAV observations. The addition of the 400-ft UAV observations begins to reduce the erroneous region of high MUCAPE across southeastern Oklahoma as well as slightly extending the plume of higher MUCAPE values southward as in the Nature Run, though this is not as complete as in the other UAV analyses. Beginning with the 1 km UAV analysis, the southward extension of the plume of higher MUCAPE values becomes apparent. These plumes do not extend as far southward into Texas as the Nature Run, but this is simply because there are no UAV observing stations positioned across Texas, thus limiting the value added outside of Oklahoma. It can be noted that the 1-, 2-, and 3-km UAV analyses all contain similar values of MUCAPE across the domain, suggesting that the most unstable layer lies somewhere in the lowest 1 km. Additionally, it can be noted that there is a general high bias in the MUCAPE fields across southcentral Oklahoma. This is likely due to the low- to mid-level lapse rates present in the WRF UAV analyses. Looking back at Fig. 3.33 the region of the cross section above 3 km MSL appears to be colder in the WRF analyses than in the Nature Run while the near-surface theta-e values are roughly similar. This suggests that the low- to mid-level lapse rates are slightly steeper in the UAV analyses and therefore generate higher MUCAPE values.

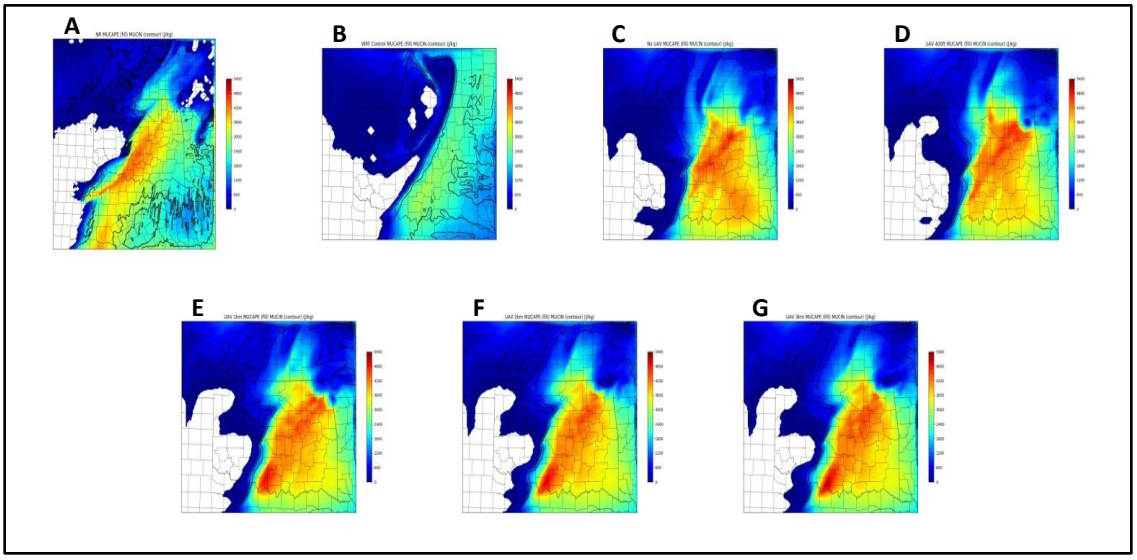

Figure 3.36: 1800 UTC analysis MUCAPE (fill) and MUCIN (contours) for the Nature Run (A), WRF Control (B), No UAV (C), UAV 400ft (D), UAV 1km (E), UAV 2km (F), and UAV 3km (G) model runs.

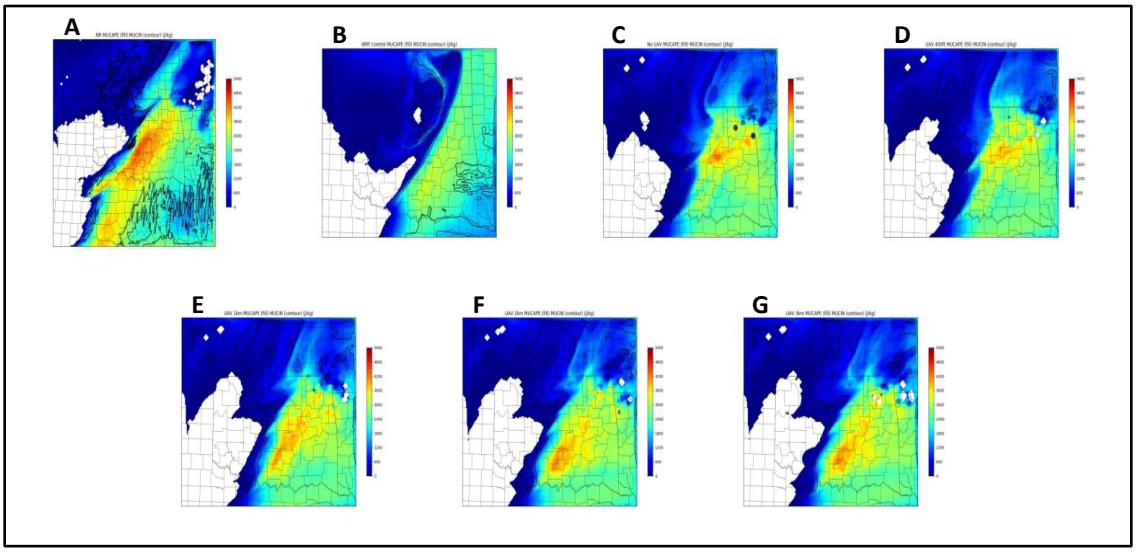

Figure 3.37: One hour forecast for MUCAPE (fill) and MUCIN (contours) for the Nature Run (A), WRF Control (B), No UAV (C), UAV 400ft (D), UAV 1km (E), UAV 2km (F), and UAV 3km (G) model runs valid at 1900 UTC.

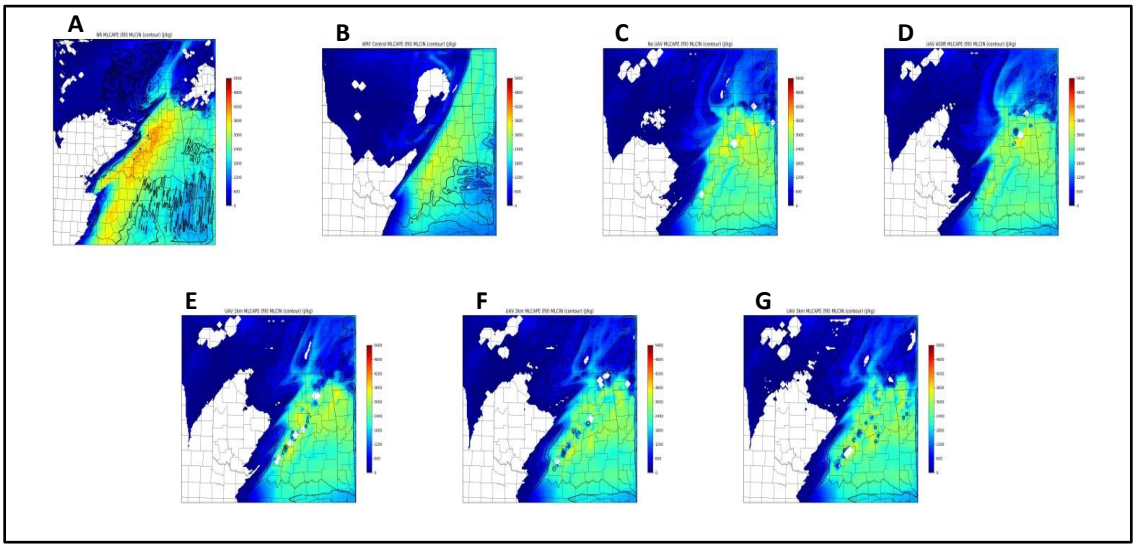

Figure 3.38: Two hour forecast for MUCAPE (fill) and MUCIN (contours) for the Nature Run (A), WRF Control (B), No UAV (C), UAV 400ft (D), UAV 1km (E), UAV 2km (F), and UAV 3km (G) model runs valid at 2000 UTC.

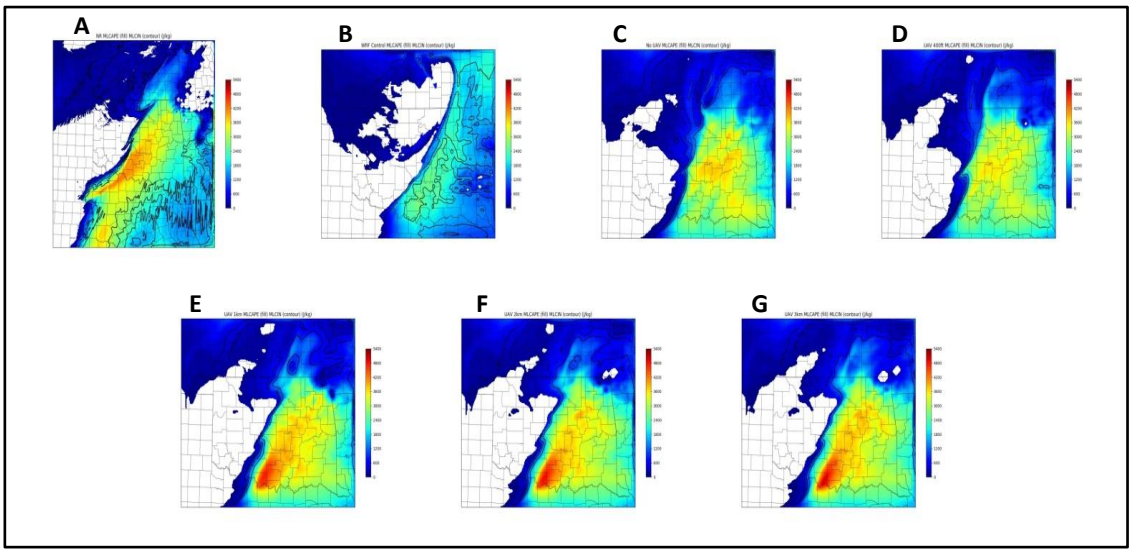

Figure 3.39: 1800 UTC analysis MLCAPE (fill) and MLCIN (contours) for the Nature Run (A), WRF Control (B), No UAV (C), UAV 400ft (D), UAV 1km (E), UAV 2km (F), and UAV 3km (G) model runs.

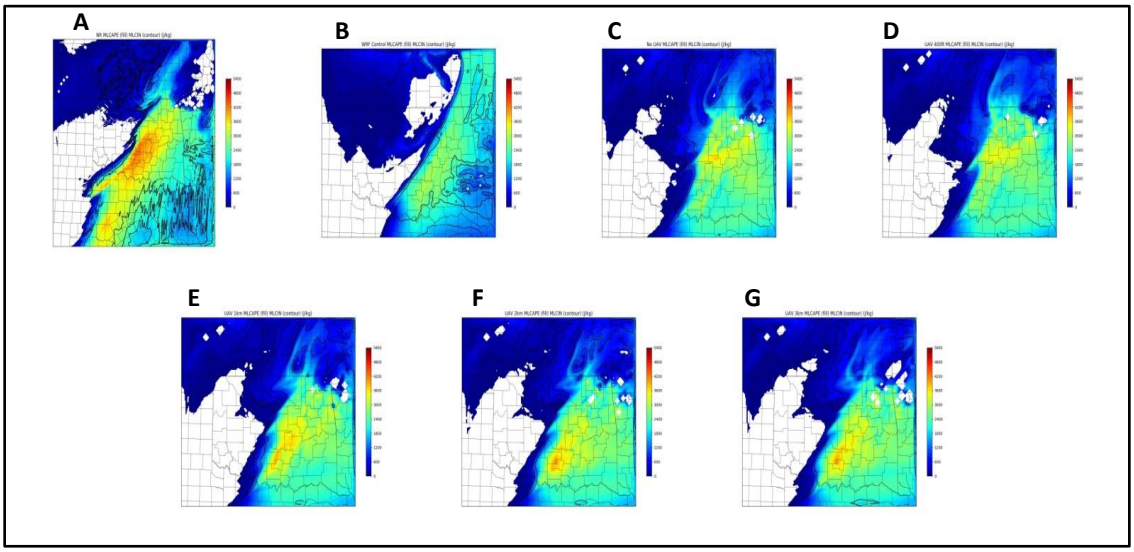

Figure 3.40: One hour forecast for MLCAPE (fill) and MLCIN (contours)for the Nature Run (A), WRF Control (B), No UAV (C), UAV 400ft (D), UAV 1km (E), UAV 2km (F), and UAV 3km (G) model runs valid at 1900 UTC.

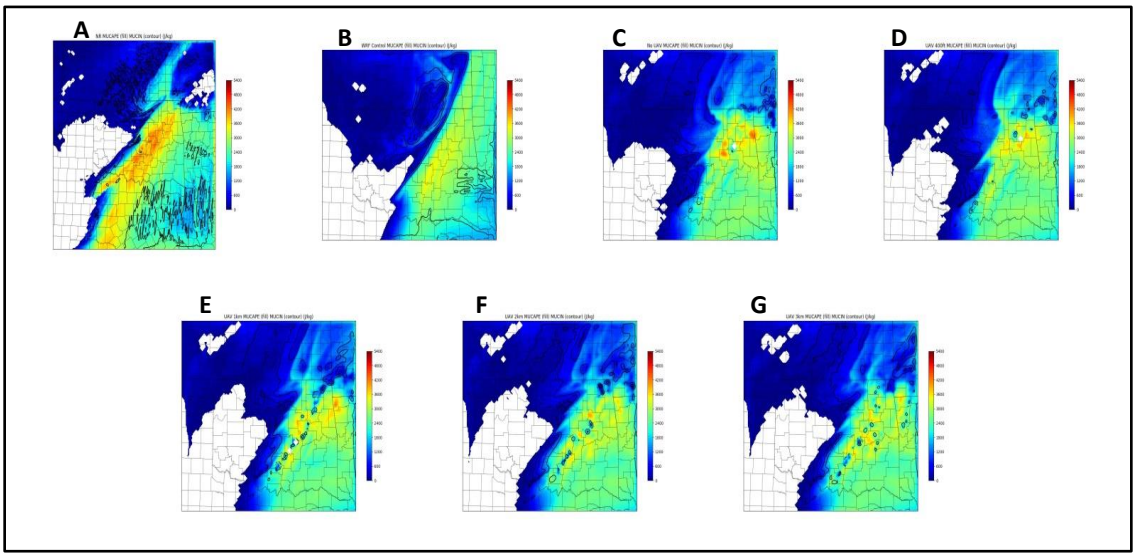

Figure 3.41: Two hour forecast for MLCAPE (fill) and MLCIN (contours)for the Nature Run (A), WRF Control (B), No UAV (C), UAV 400ft (D), UAV 1km (E), UAV 2km (F), and UAV 3km (G) model runs valid at 2000 UTC.

One hour into the WRF free forecasts MUCAPE values across the domain decrease for all WRF experiment forecasts (Figure 3.37). However, the 1, 2, and 3 km

forecasts maintain higher MUCAPE values across southern Oklahoma in accordance with the Nature Run at 1900 UTC. This trend continues through 2000 UTC (Figure 3.38) as ongoing convection begins to contaminate the MUCAPE and MUCIN fields. Despite the convection, the 1-, 2-, and 3-km forecasts continue to support higher MUCAPE across southern and central Oklahoma compared to the "No UAV" forecast, suggesting value added to the short-term forecast by the UAV observations.

WRF experiment analyses rank very similar when comparing MLCAPE/MLCIN (Figure 3.39). As with MUCAPE, the Nature Run exhibits a plume of higher MLCAPE values extending from central Oklahoma south/southwestward into north Texas characterized by MLCAPE values in the 3.5 – 4 kJ/kg range. Although the WRF Control run captures a meridionally oriented plume of instability, it does not capture these MLCAPE values well and shows the warm sector capped with MLCIN values of 50 to 100 J/kg. While the addition of data in the "No UAV" experiment eliminates this capping, it does not adequately capture the MLCAPE plume to the south and generates too much MLCAPE across the southeastern portion of Oklahoma.

As with MUCAPE, the addition of UAV observations in the 400 ft UAV experiment does alter the MLCAPE field slightly towards the Nature Run, but the greatest benefits are not observed until at least 1 km of UAV data is added. Figure 3.39 shows this improvement to the analysis. As with the MUCAPE field, MLCAPE differs only slightly among the 1-, 2-, and 3-km UAV analyses and there is a slight over production of MLCAPE along the instability plume near the Oklahoma/Texas border, likely again due to lapse rate differences. Since MLCAPE considers only parcels in the lowest 100 hPa of the atmosphere, these similarities between the 1-, 2-, and 3-km analyses are not surprising

as the additional data above the lowest 100 hPa will only indirectly influence the near-surface thermodynamic profile and will adjust only the lapse rate profile above the surface.

Similar to the MUCAPE forecasts, MLCAPE one and two hour forecasts (Figures 3.40 and 3.41) show the quick reduction in instability in the "No UAV" experiment as well as the 400 ft UAV experiment. However, higher MLCAPE value are maintained in the 1-, 2-, and 3-km UAV forecasts. Although these values are not as high as those present in the Nature Run, this result demonstrates a prolonged adherence to the Nature Run that is quickly lost in the No UAV and 400 ft experiments. This rapid loss of instability is likely related to the loss of higher theta-e air near the surface as observed at 1900 and 2000 UTC in Figures 3.33 and 3.34 in the No UAV and 400-ft UAV cross section forecasts.

3.8.2 Station Density

One of the more beneficial aspects of an OSSE is the ability to identify the network density that will give the best results with the least number of observation points. This information has the potential to save both up-front costs on instruments and equipment, but would also help reduce long-term maintenance cost. For this experiment, tests were performed using networks consisting of 75, 50, 25, and 10 stations. Station selection for the 75-station network were taken from the original 110 Mesonet sites based on station density (i.e. regions with high station density were reduced while regions with station scarcity were maintained) with the goal of keeping a uniform station distribution. Additionally, select stations were removed to incorporate a better sense of realism. For

example, stations near the Oklahoma City metro were removed first to account for the likelihood that UAVs would not be allowed to fly near highly-populated areas.

Station selection for the 50-station network removed stations from the 75-station network with the same goal of maintaining a relatively uniform station distribution while keeping station consistency between experiments. Each of these networks can be seen in Figure 3.42.

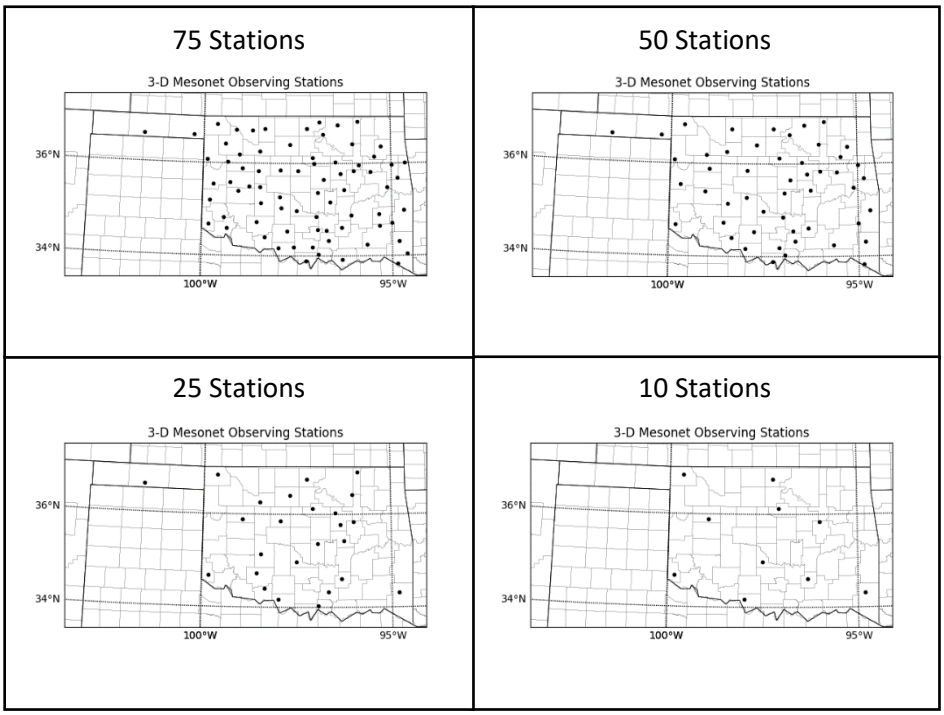

Figure 3.42: Four possible 3-D Mesonet configurations with varying station densities.

Since UAV flights up to 1 km provided reasonably good analyses of the Nature Run and initiated convection by 1900 UTC, this level was chosen as the UAV flight altitude for all network density experiments. This altitude represents a good balance between adding the benefits to the analysis and convective forecast that were observed with the 1-, 2-, and 3-km MFA experiments while maintaining reasonable operational flight parameters. The original 1-km MFA experiment represents an additional 110-station network (hereafter called 110-station network, see Fig. 2.1) to include in comparisons.

3.8.2.1 Composite Reflectivity Comparisons

As with the MFA experiments, composite reflectivity is employed here to highlight the differences among the network experiments and to best identify times of convective initiation, as seen in Figures 3.43 through 3.47 As with the MFA experiments, the most notable differences among the network experiments are found within the first few hours of the free forecast. After this point the differences between experiments are minimal. As expected, none of the reduced network configurations produce as robust convection by 1900 UTC as the original 110 station network. The only exception to this is the 10-station network. This interesting result is not considered to be realistic and is discussed further in subsequent sections. The 75, 50, and 25 station networks all show the initial stages of convective initiation at 1900 UTC with the 25-station network showing slightly more developed convective cells. By 2000 UTC all three experiments show similar convective cells in the same region as the original 110 station network. This result suggests that the lower density, 25-station network may perform as adequately as a 50 or

75 station network. However, compared to the No UAV experiment these appear to produce a drier solution with overall fewer regions of precipitation.

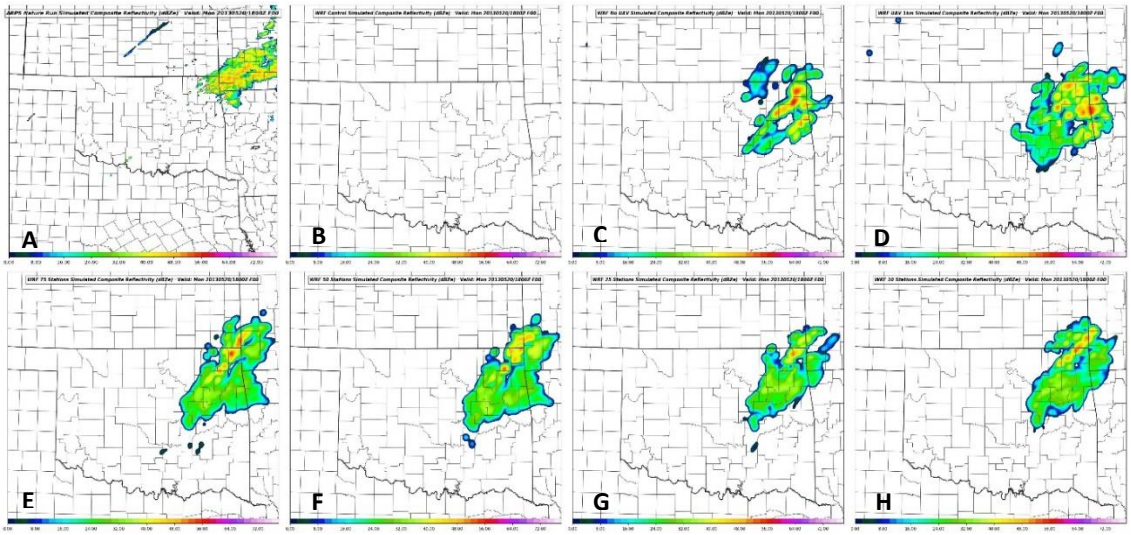

Figure 3.43: Composite Reflectivity forecast from the Nature Run (A) and WRF Control (B) and analysis fields from the No UAV (C), 110 Station (D), 75 Station (E), 50 Station (F), 25 Station (G), and 10 Station (H) experiments valid at 1800 UTC.

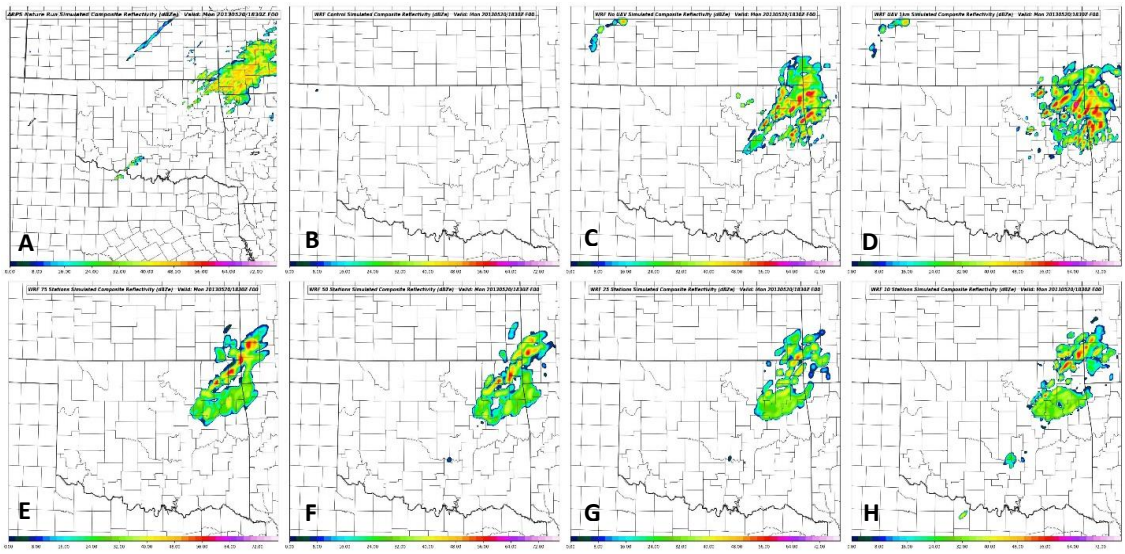

Figure 3.44: Composite Reflectivity forecasts from the Nature Run (A), WRF Control (B), No UAV (C), 110 Station (D), 75 Station (E), 50 Station (F), 25 Station (G), and 10 Station (H) experiments valid at 1830 UTC.

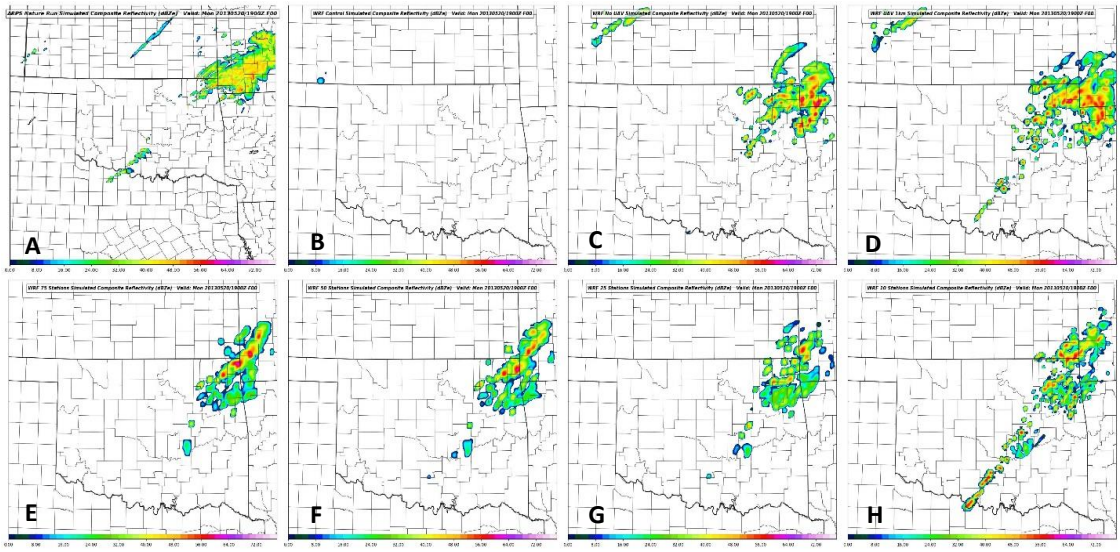

Figure 3.45: Composite Reflectivity forecasts from the Nature Run (A), WRF Control (B), No UAV (C), 110 Station (D), 75 Station (E), 50 Station (F), 25 Station (G), and 10 Station (H) experiments valid at 1900 UTC.

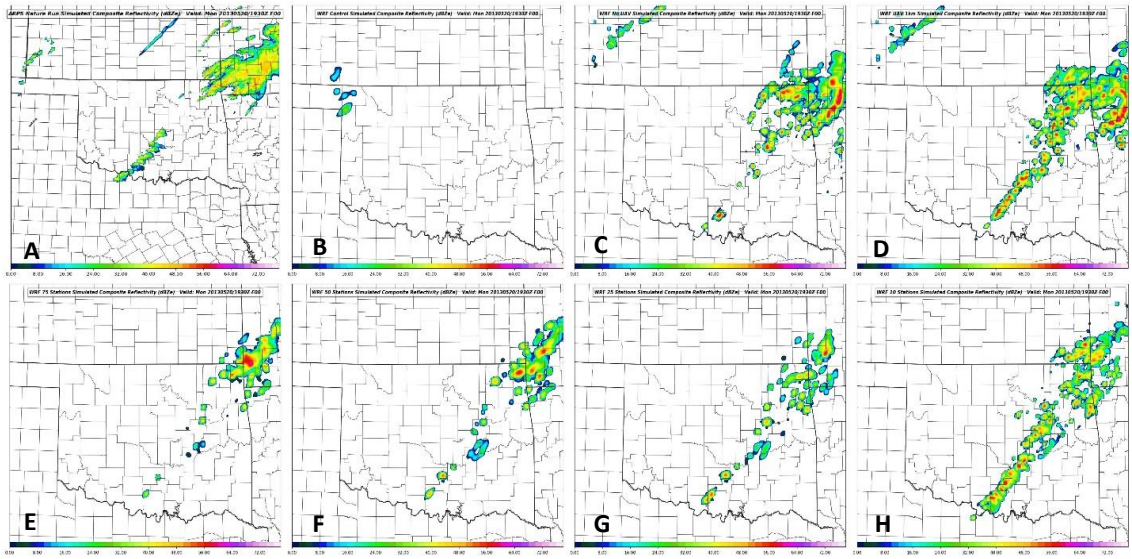

Figure 3.46: Composite Reflectivity forecasts from the Nature Run (A), WRF Control (B), No UAV (C), 110 Station (D), 75 Station (E), 50 Station (F), 25 Station (G), and 10 Station (H) experiments valid at 1930 UTC.

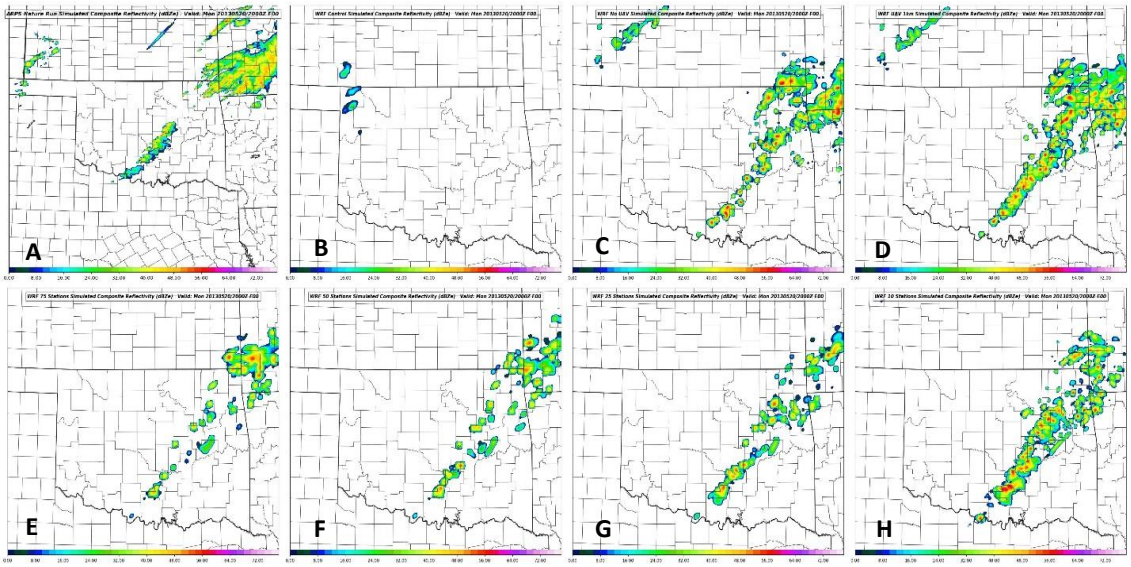

Figure 3.47: Composite Reflectivity forecasts from the Nature Run (A), WRF Control (B), No UAV (C), 110 Station (D), 75 Station (E), 50 Station (F), 25 Station (G), and 10 Station (H) experiments valid at 2000 UTC.

3.8.2.2 Surface RMSE Comparison

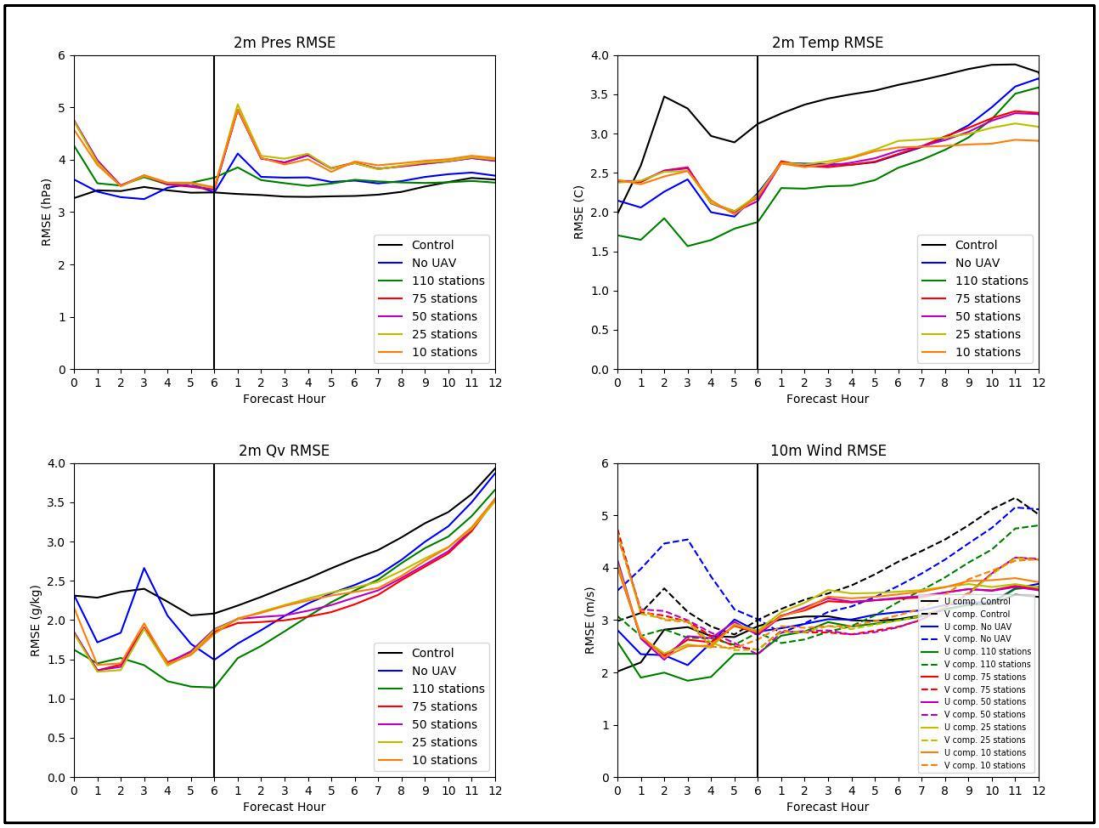

Figure 3.48: RMSE plots during the data assimilation cycling period (left of the vertical black line) and during the free forecast period (right of the black line) for surface pressure (upper left), 10 m U and V winds (upper right), 2 m mixing ratio (bottom left), and 2 m temperature (bottom right).

Similar to the MFA experiments, comparing surface RMSE values for MSL pressure, 2-meter mixing ratio, 2-meter temperature, and 10-meter U and V winds in Figure 42 may help reveal information about the optimal UAV network configuration and the DA system's dependence on horizontal resolution for producing the best analysis. While little impact to the surface fields were expected in the MFA tests where horizontal station spacing is held constant, the network density tests should demonstrate horizontal, as well as vertical, impacts to the analysis.

Comparing surface RMSE values from the network density experiments (Figure 3.48) immediately suggests a need for high-density networks. In every field the 110-station network contains lower RMSE values than the other network experiments. Interestingly, the remaining network analyses create similar analyses that compare well with the No UAV experiment in some fields (such as temperature and pressure). This is likely due to the network density differences between the FNL, Mesonet, and experimental UAV networks. While the FNL network inserts data at around 80 locations, the first UAV experiment only inserts data at 75 locations. Since the FNL network now has a higher spatial density than the UAV network, it is likely creating a greater influence than the UAV network at the surface. It should be noted that this effect may also be due to the choice of horizontal correlation lengths during the ADAS procedure.

Additionally, the higher RMSE values in the UAV experiments' pressure, mixing ratio, and temperature fields during the first two hours of the DA cycling (Figure 3.48) may be due to noise being sampled from the Nature Run itself. Even though the ARPS begins a warm-start free forecast at 12 UTC there may still be high-frequency noise in the surface fields that had not been smoothed out through the model integration. As this noise settles out through 18 UTC, more representative observations are taken at the "observation times" and allows for a better analysis by the end of the DA cycling period. This issue is addressed further in section 4.2.

3.8.2.3 Vertical Profile Comparison

Vertical profiles of temperature, dewpoint, wind speed, and wind direction were again sampled at OUN (Norman, Oklahoma) to compare how well each of the network experiments captured the Nature Run environment. Figures 3.49 and 3.50 show the

vertical analyses and errors for each experiment, including the WRF Control and No UAV experiments. Although the surface RMSE results suggest that there is no improvement to the analysis with lower density UAV networks, the vertical profiles counter this by showing improvements in the vertical moisture, temperature, and wind speed in the low to mid-levels.

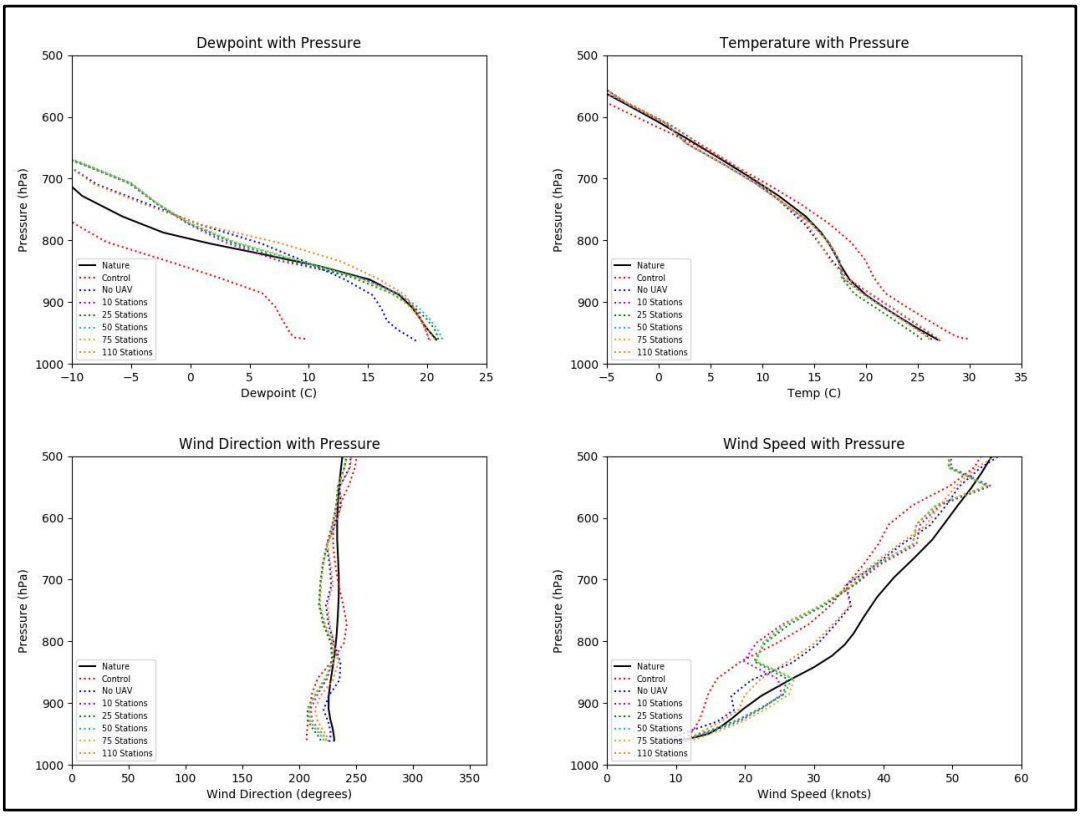

Figure 3.49: Vertical profiles of dewpoint (upper left), temperature (upper right), wind direction (bottom left), and wind speed (bottom right) analyses valid at 1800 UTC.

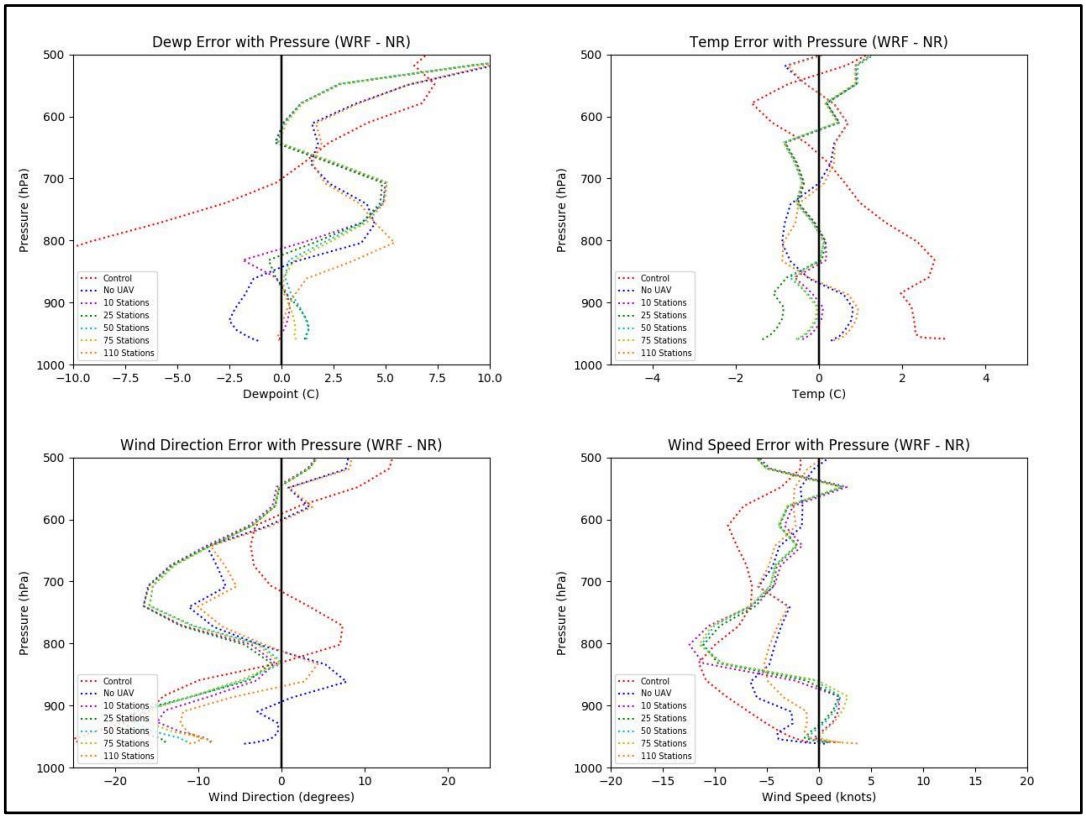

Figure 3.50: Vertical profiles of dewpoint (upper left), temperature (upper right), wind direction (bottom left), and wind speed (bottom right) analyses errors valid at 1800 UTC.

Improvements to the low- and mid-level moisture, low-level wind speed, and in the mid-level temperature profiles can be observed in Figures 3.49 and 3.50. These analysis at times match closer to the Nature Run than the 110-station network. One possible explanation for is similar to the high RMSE noted in some of the surface fields in section in 3.8.2.2. If excess noise from the Nature Run is being directly sampled by all 110 sites, then these errors may be accumulating through the DA cycle and manifesting as analysis errors at 1800 UTC. Likewise, with fewer observing sites less noise is being directly sampled and allows for a slightly improved analysis. While the surface RMSE data is a more robust measure of these errors, the single point profiles shown here may also be localized noise in the analyses themselves. This issue is discussed further in section 4.1.

3.8.2.4 Cross Section Comparison

Just as with the MFA experiments, analyzing cross sections of both mixing ratio and equivalent potential temperature provides beneficial information on the ability for each network density experiment to re-create the boundary layer structure of the Nature Run. Each cross section is taken from the same line across the domain depicted in Fig. 3.27. Additionally, each cross section inspects the lowest 4 km MSL of the atmosphere, which should be more than sufficient considering all UAV flights in the network density experiments only reach 1 km AGL. These cross sections are particularly important for the network density experiments as they show both the horizontal and vertical impacts of the various UAV networks on the analysis.

3.8.2.4.1 Mixing Ratio Cross Sections

Cross sections of mixing ratio at the 1800 UTC analysis time are given in Figure 3.51. One of the most notable observations is the excess moisture observed below 2 km MSL in the 10-station network experiment with mixing ratios between 18-20 g/kg. This is consistent with Fig. 3.54 that shows the extent of this moisture bias in the low levels as compared to the Nature Run. This also explains why this excess moisture was not observed in the OUN sample profile as this moisture plume is mainly confined to southern Oklahoma. Comparing this cross section to the No UAV and WRF Control cross sections suggests that the source of this excess moisture is not being artificially introduced by the WRF initial conditions, the GFS LBC (up to 1800 UTC), or the simulated FNL and Mesonet obs. The 925 hPa dewpoint analysis from the 10-station experiment at 1700 UTC (not shown) shows the early stages of a localized region of excess moisture. This suggests the possibility that a UAV observation with a particularly high moisture measurement was accepted in the analysis, unmodified due to the lack of nearby UAV

stations, and the error allowed to propagate through to the 1800 UTC analysis. Looking at the simulated UAV data from a UAV site nearest to the excessive moisture plume in Figure 3.54 shows that there appears to be a slight high bias in the simulated dewpoint data (Figure 3.55). The possible sources for this observation error are discussed further in section 4.1.2. Besides the high moisture bias, the 10-station network analysis shows a shallower plume of boundary layer moisture as well as a more diffuse moisture gradient on the western edge of the moist sector (roughly at -98.0 longitude).

Another noteworthy observation is the similarities among the 75, 50, and 25-station network experiments. Each experiment analyzes a plume of boundary layer moisture extending above 1 km MSL with mixing ratios of 16 – 18 g/kg, similar to the Nature Run. Although the longitudinal extent of this moist plume is somewhat stunted, especially when compared to the 110-station network (1km UAV) experiment, the overall shape of boundary layer moisture cross section is captured well by all three experiments and represents an improvement over the WRF Control and No UAV experiments.

One hour into the free forecast the similarities among the three experiments continue as each cross section continues to show identical boundary layer moisture features and compare well to the 110-station network forecast. Besides lacking breadth longitudinally, these experiments compare well to the Nature Run at 1900 UTC and show signs of broad lift ongoing as the moist plume increases in depth. The 10-station network continues to show a high moisture bias and diffuse western moisture gradient. The upward stretching of the moist plume at around -97.0 degrees longitude suggest a region of stronger lift, possibly due to an updraft from the developing convection that was observed at this time (Fig. 3.52).

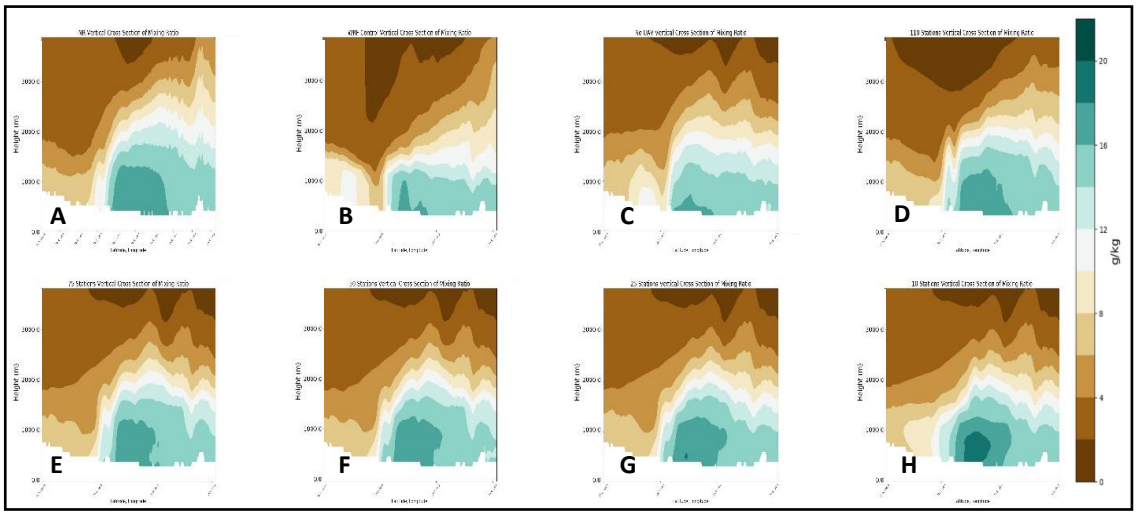

Figure 3.51: 1800 UTC analysis mixing ratio cross sections from 0 to 4 km above MSL for the Nature Run (A), WRF Control (B), No UAV (C), 110 stations (D), 75 stations (E), 50 stations (F), 25 stations (G), and 10 stations (H).

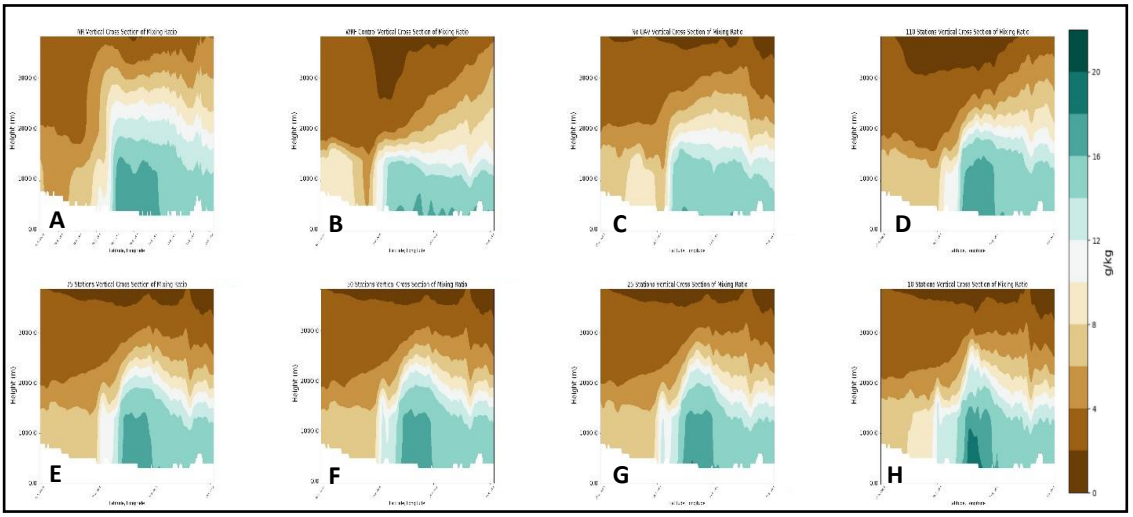

Figure 3.52: 1900 UTC forecast for mixing ratio cross sections from 0 to 4 km above MSL for the Nature Run (A), WRF Control (B), No UAV (C), 110 stations (D), 75 stations (E), 50 stations (F), 25 stations (G), and 10 stations (H).

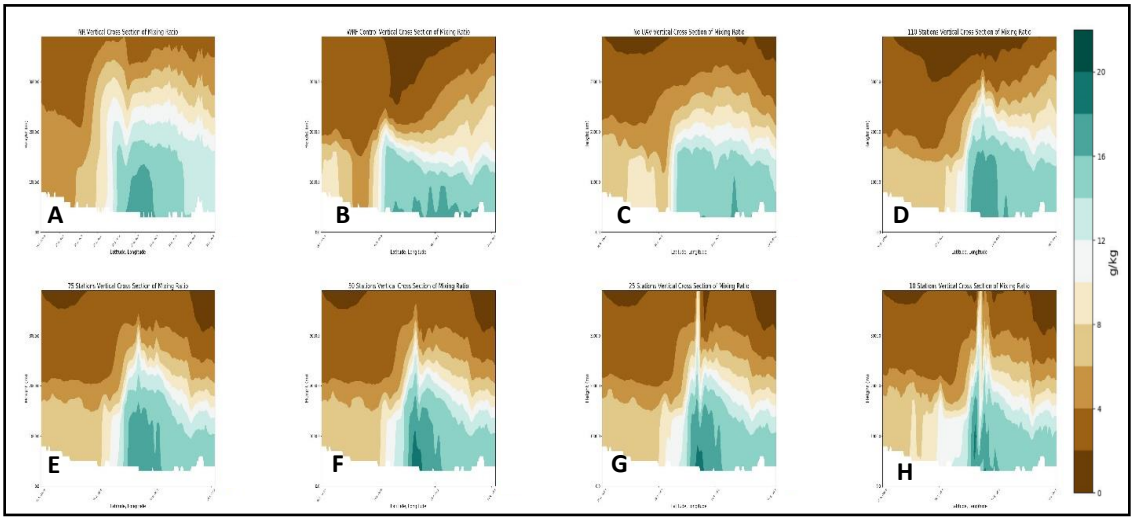

Figure 3.53: 1900 UTC forecast for mixing ratio cross sections for from 0 to 4 km above MSL the Nature Run (A), WRF Control (B), No UAV (C), 110 stations (D), 75 stations (E), 50 stations (F), 25 stations (G), and 10 stations (H).

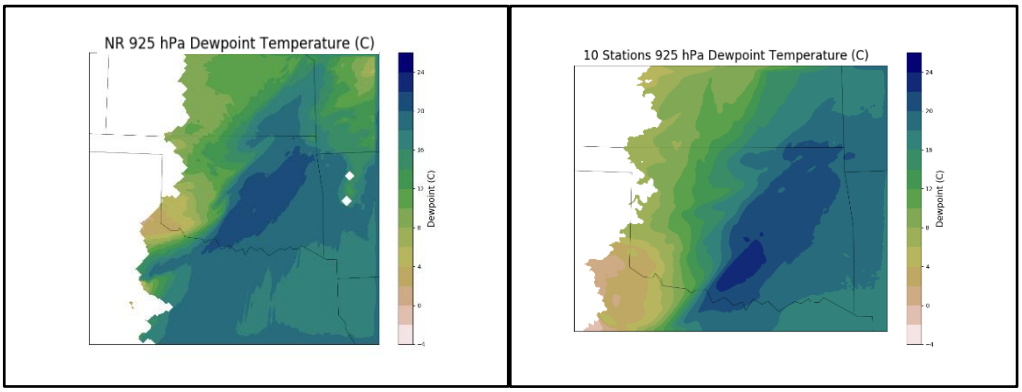

Figure 3.54: 925 hPa Dewpoint forecast and analysis for the Nature Run (left) and 10-station UAV test (right) respectively valid at 1800 UTC.

The updraft and downdraft region of a convective storm becomes more apparent in the cross section by 2000 UTC (Figure 3.53). Similar plumes of moist (ascending) and drier (descending) air, as well as the persistence of high (> 16 g/kg) boundary layer moisture are observed in the other UAV network experiments by this time but not in the WRF control and No UAV experiments. While the 50 and 25-station network forecasts

begin to show high moist biases below 1 km MSL, they continue to retain the shape and overall structure of the Nature Run boundary layer. However, this excess moisture may help explain the slightly more robust convection observed in the 50 and 25-station network composite reflectivity fields at this time (Figure 3.47).

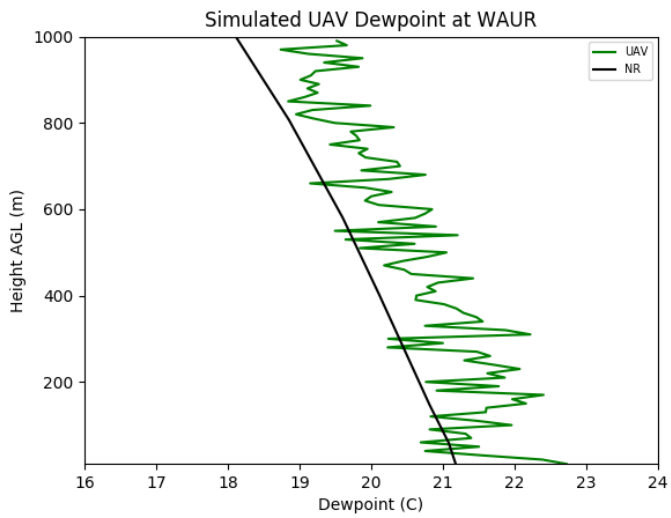

Figure 3.55: Comparison of the Nature Run (black) and simulated UAV (green) dewpoint profiles sampled at 1800 UTC at the Waurika, OK (WAUR) Mesonet site.

3.8.2.4.2 Equivalent Potential Temperature Cross Sections

Cross sections of theta-e are analyzed for the network density experiments in the same manner as the maximum flight altitude experiments. Cross sections of the theta-e analyses at 1800 UTC are given in Figure 49 and reveal similar trends as those observed in the mixing ratio cross sections. Looking at the 10-station network analysis it becomes clear how the excess moisture below 1 km MSL is contributing to high theta-e values up to 362 K, 6 K warmer than the maximum Nature Run value. As with the mixing ratio cross sections, the theta-e cross sections reveal a more diffuse gradient in temperature

along the western edge of the higher theta-e air mass in the 10-station network analysis as well as a shallower layer of warm air.

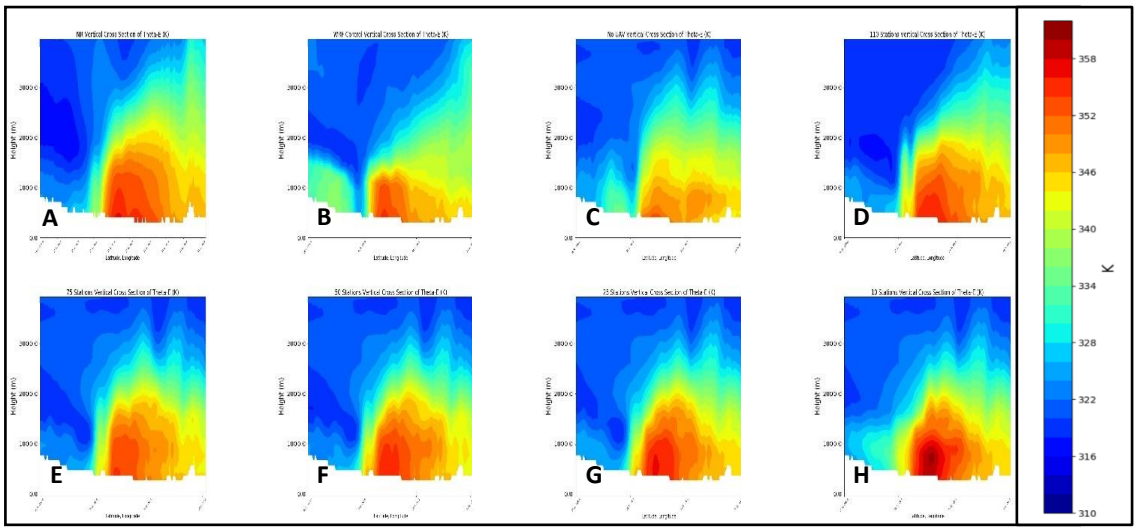

Figure 3.56: 1800 UTC analysis theta-e cross sections from 0 to 4 km above MSL for the Nature Run (A), WRF Control (B), No UAV (C), 110 stations (D), 75 stations (E), 50 stations (F), 25 stations (G), and 10 stations (H).

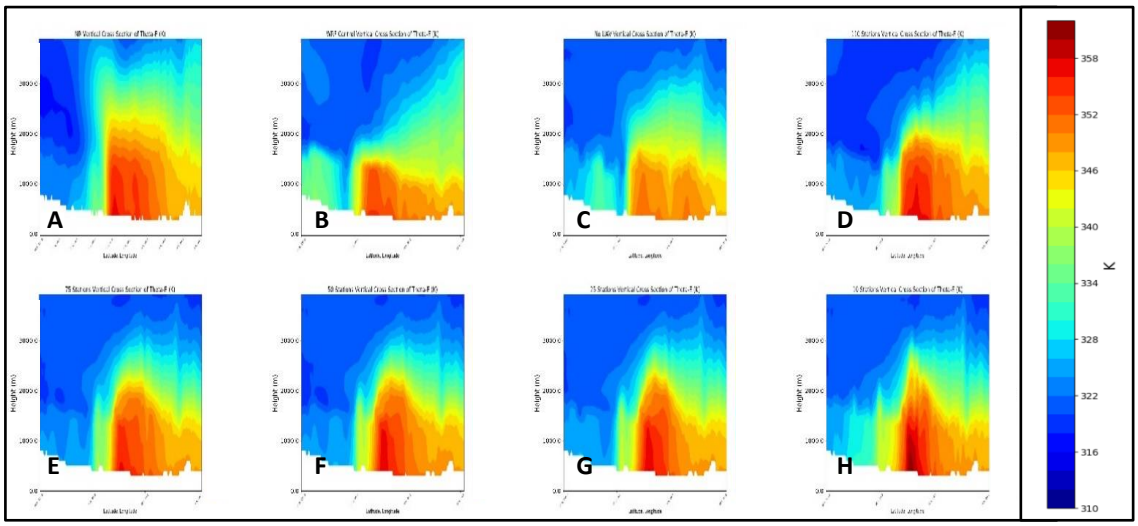

Figure 3.57: 1900 UTC forecast theta-e cross sections from 0 to 4 km above MSL for the Nature Run (A), WRF Control (B), No UAV (C), 110 stations (D), 75 stations (E), 50 stations (F), 25 stations (G), and 10 stations (H).

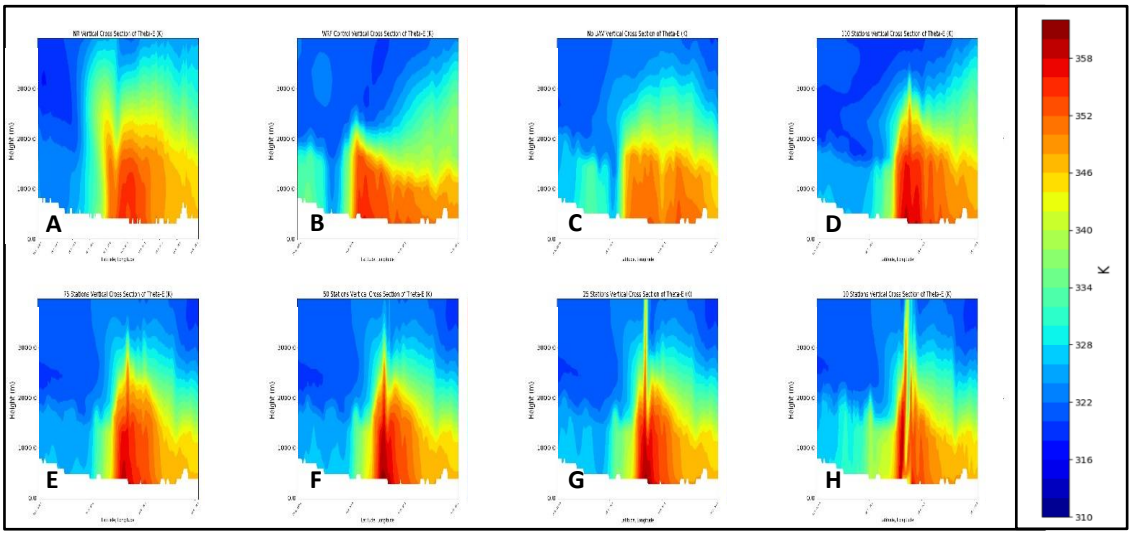

Figure 3.58: 2000 UTC forecast theta-e cross sections from 0 to 4 km above MSL for the Nature Run (A), WRF Control (B), No UAV (C), 110 stations (D), 75 stations (E), 50 stations (F), 25 stations (G), and 10 stations (H).

Such inconsistencies are not as readily observed in the other UAV network density analyses, which generally capture the thermal shape of the Nature Run's boundary layer fairly well. Although these analyses show improvements over the WRF Control 1800 UTC forecast and the No UAV analysis, the 75, 50, and 25-station network analyses struggle to consistently capture the higher theta-e values in the lowest 1 km MSL of the Nature Run boundary layer. Lower temperatures are also noted east of -95.0 degrees longitude where all of the UAV network analyses, with the exception of the 110-station network, struggle to accurately capture the temperatures observed in the Nature Run.

Trends observed in the mixing ratio cross sections for 1900 UTC are also evident in the theta-e cross sections (Figure 3.56. The 10-station network forecast continues to show a warm bias in the lower levels with a vertically stretched plume of higher theta-e air suggesting locally strong lift. The weak thermal gradient on the western edge continues to be evident as well as a poor overall shape to the boundary layer thermal

structure as compared to the Nature Run and other UAV forecasts. Despite struggling to accurately capture theta-e values near the surface, the 75, 50, and 25-station network forecasts show considerably good resemblance to the Nature Run, including capturing the low level thermal gradient. However, the value of all 110 stations can be observed here as the eastern extent of the 348-350 K temperatures and vertical extent of the > 328 K temperatures is captured better by the larger observing network. By 2000 UTC the higher moisture values in the 50 and 25-station network forecasts are likely contributing to the higher theta-e temperatures near the surface as seen in Figure 3.57. Despite this, the UAV network forecasts continue to show reasonably good comparison to the Nature Run's boundary layer thermal profile in terms of shape and vertical extent. At this point the impacts of convection on the boundary layer thermal profile are becoming clearer, especially in the 10-station network forecast. However, inspecting these cross sections reveals that while some detail is lost with a reduced number of stations, a reasonably good analysis and short term forecast of the boundary layer's thermal structure can be obtained with fewer than 110 stations.

3.8.2.5 Convective Available Potential Energy Comparisons

As with the MFA experiments, comparing MUCAPE and MLCAPE can help determining each network experiments' ability to recreate the convective environment observed in the Nature Run. Both MUCAPE and MLCAPE are computed in the same way as described in section 3.8.1.5. Similar to the cross sections, plots of MU/MLCAPE highlight thermodynamic differences between the WRF UAV experiments across the entire three-dimensional domain.

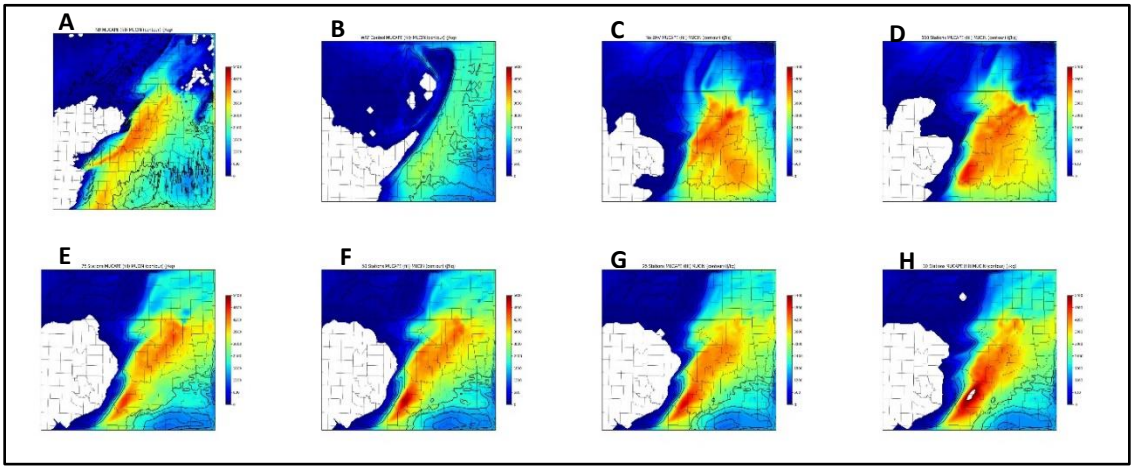

Figure 3.59: 1800 UTC analysis of MUCAPE (fill) and MUCIN (contours) for the Nature Run (A), WRF Control (B), No UAV (C), 110 stations (D), 75 stations (E), 50 stations (F), 25 stations (G), and 10 stations (H).

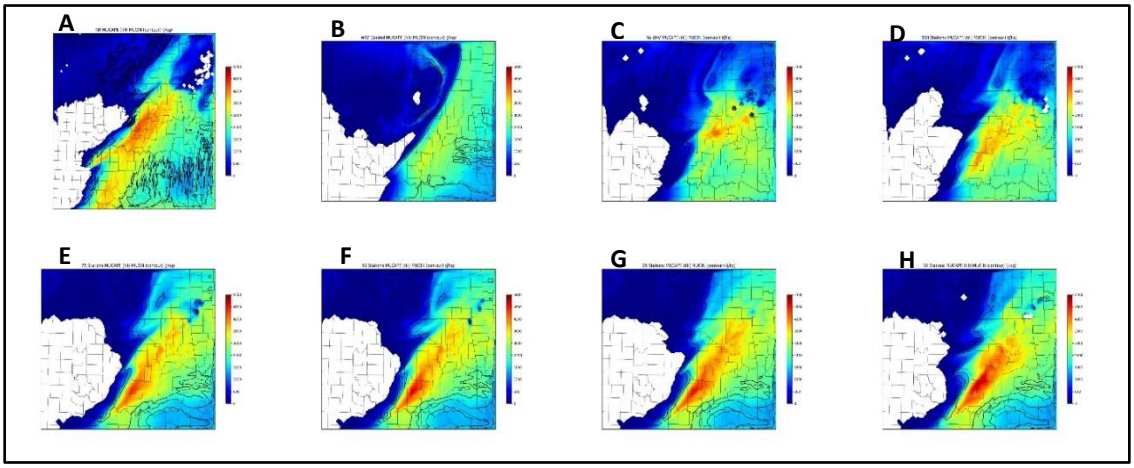

Figure 3.60: 1900 UTC forecast of MUCAPE (fill) and MUCIN (contours) for the Nature Run (A), WRF Control (B), No UAV (C), 110 stations (D), 75 stations (E), 50 stations (F), 25 stations (G), and 10 stations (H).

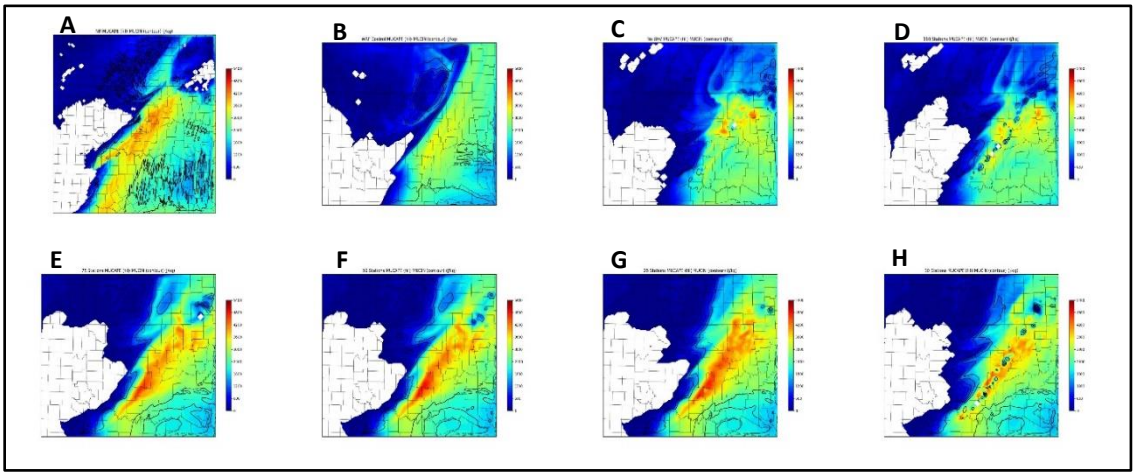

Figure 3.61: 2000 UTC forecast of MUCAPE (fill) and MUCIN (contours) for the Nature Run (A), WRF Control (B), No UAV (C), 110 stations (D), 75 stations (E), 50 stations (F), 25 stations (G), and 10 stations (H).

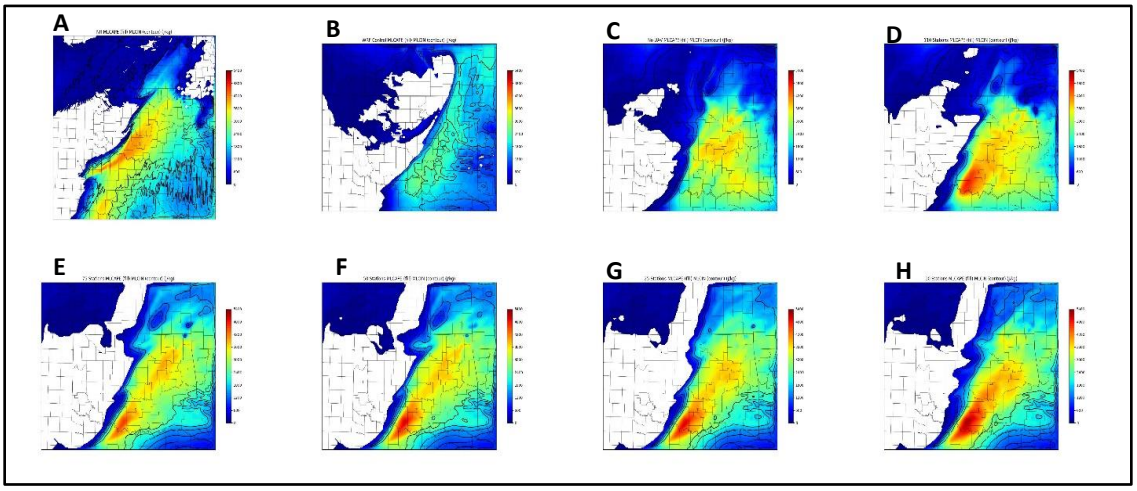

Figure 3.62: 1800 UTC analysis of MLCAPE (fill) and MULIN (contours) for the Nature Run (A), WRF Control (B), No UAV (C), 110 stations (D), 75 stations (E), 50 stations (F), 25 stations (G), and 10 stations (H).

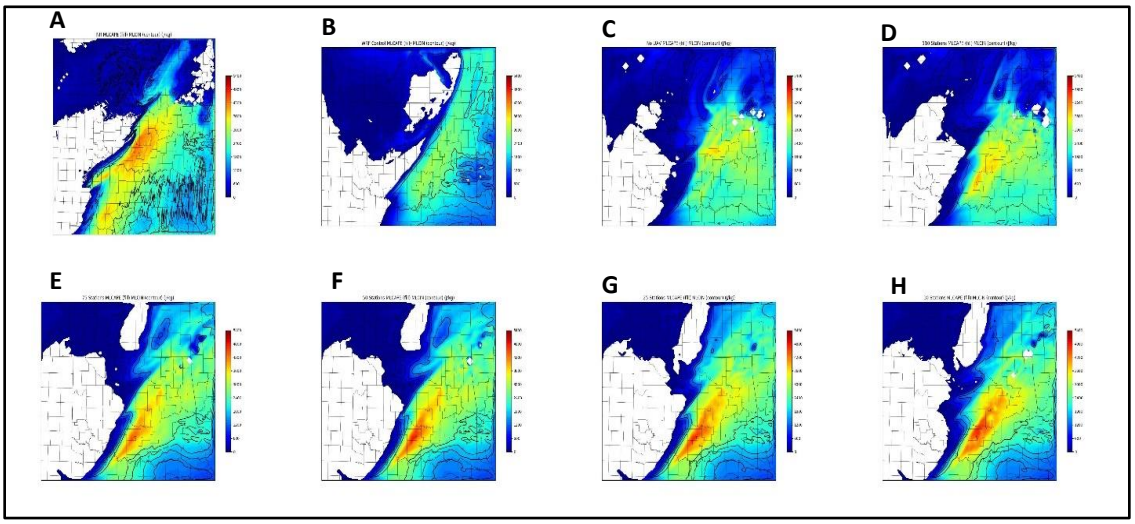

Figure 3.63: 1900 UTC forecast of MLCAPE (fill) and MULIN (contours) for the Nature Run (A), WRF Control (B), No UAV (C), 110 stations (D), 75 stations (E), 50 stations (F), 25 stations (G), and 10 stations (H).

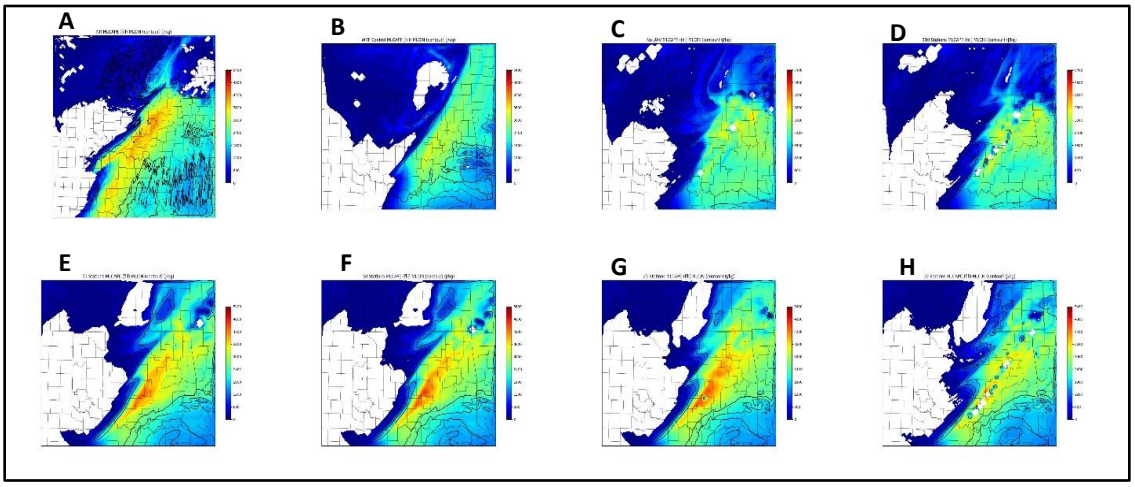

Figure 3.64: 2000 UTC forecast of MLCAPE (fill) and MULIN (contours) for the Nature Run (A), WRF Control (B), No UAV (C), 110 stations (D), 75 stations (E), 50 stations (F), 25 stations (G), and 10 stations (H).

Comparing MUCAPE analyses at 1800 UTC (Figure 3.59) the 10-station network contains MUCAPE values much greater than the Nature Run or any experiment. This additional instability is a side effect of the excess low-level moisture observed in the 10-

station analysis in the 925 hPa dewpoint analysis field (Figure 3.54) and the mixing ratio cross section (Figure 3.51). However, this helps explain why the 10-station network was able to produce convection prior to the other experiments. As with the 110-station network experiment, all station-density experiments were able to correct the region of low MUCAPE present in the WRF Control and No UAV experiments across southern Oklahoma and into northern Texas. As in the 110-station experiment, the network density experiments show a slight high bias in MUCAPE across far southern Oklahoma and northern Texas, though the smaller networks struggle to capture the higher MUCAPE values as observed in the Nature Run. Additionally, all the network experiments, with the exception of the 110-station experiment, introduce MUCIN across southeastern Oklahoma. While MUCIN is present in the Nature Run across portions of northern Texas, there is none across far southeast Oklahoma. This may be caused by the lower theta-e values across that part of the state as seen in the theta-e cross sections for each network experiment (Figure 3.56).

MUCAPE fields one and two hours into the free forecast period for each network density experiment are shown in Figures 3.60 and 3.61, respectively. At 1900 UTC the high bias in the 10-station network continues to be evident with the other network experiments containing only slightly higher MUCAPE values than the Nature Run. The placement of the greatest instability is shifted slightly southward in the network experiments as compared to the Nature Run as well as the 110-station experiment. By 2000 UTC the 75, 50, and 25-station experiments continue to show high MUCAPE values, though this is likely a consequence of their slightly delayed CI whereas the 110 and 10-station networks show MUCAPE reduction as convection continues to grow. This

suggests that these experiments are not generating convection due to a lack of instability or convective inhibition, but rather a weak or delayed forcing mechanism.

Analyzing MLCAPE values in a similar fashion reveals similar trends. The 1800 UTC analysis of MLCAPE show similar results to the MUCAPE with all UAV experiments filling in the instability gap present in the WRF Control and No UAV experiments and the 10-station network displaying considerably higher MLCAPE values than the Nature Run. Furthermore, just as MUCIN was present over southeastern Oklahoma, all UAV network experiments possess MLCIN over the same region. As mentioned, the likely culprit for the convective inhibition is reduced theta-e values, and hence a more stable airmass, over this region as evidenced by the 1800 theta-e cross sections (Fig. 3.56).

One hour into the free forecast, the trends in the MLCAPE fields mirror those observed in the MUCAPE fields (Figure 3.62). The 10-station network continues to show higher MLCAPE than any other experiment and the Nature Run and is also showing signs of ongoing convection. While the 110-site network (the 1 km UAV experiment) also has ongoing convection at 1900 UTC, the MLCAPE values are lower compared to the other network experiments, likely due to CI that began just prior to 19 UTC (Figure 3.63). Once again, the 75, 50, and 25-station networks show an unstable and uncapped environment with 3 – 4.5 kJ/kg of MLCAPE. This further supports the notion that CI is not being hindered by a lack of instability or inhibition. MLCAPE fields at 2000 UTC (Figure 3.64) continue to show trends similar to those observed in MUCAPE with the 75, 50, and 25-station networks showing the highest instability values compared to all other WRF experiments and the Nature Run. However, all experiments containing UAV observations

continue to show more representative MLCAPE fields in terms of magnitude and placement of the greatest instability when compared to the WRF Control and No UAV forecasts. Additionally, the 75, 50, and 25-station networks show similar MLCAPE and MLCIN fields even two hours into the free forecast, suggesting that all major features of the thermodynamic environment are captured even with the reduced network density.

Chapter 4

4.1 Discussion and Conclusions

4.1.1 Maximum Flight Altitude Summary

One of the main goals of this work was to investigate the impacts of assimilating simulated UAV observations on short term numerical forecasts on convective initiation and boundary layer structure as well as identify the ideal characteristics of a hypothetical UAV observing network, specifically the ideal maximum flight altitude and network density. While assimilating UAV observations, even up to 3 km AGL, did not recreate the Nature Run exactly, as seen in the vertical profile plots and cross sections, the additional information provided by the UAV observations helped recreate boundary layer thermal structure and force convective initiation at a similar time and location compared to the Nature Run as observed in the composite reflectivity Figures (Fig. 3.18). This convection takes on a similar convective mode compared to the Nature Run, though the grid resolution of the WRF forecasts prevents exact replication. The benefits of the UAV data are most evident within the first one to three hours of the free forecasts, after which point all forecasts begin to diverge from the Nature Run in a similar fashion. But studies such as Weiss et al. (2008) describe similar difficulties in forecasting the downstream evolution of convection.

It was also noted that for nearly all WRF analyses surface wind speeds showed a nearly 2.6 ms^{-1} (5 kt) high bias. This may be explained by differences in the PBL schemes used by both the ARPS and WRF-ARW models. While the ARPS used a non-local scheme for turbulent mixing, the WRF employed a local scheme. As described by Cohen et al. (2015), local and non-local PBL schemes can often explain differences in boundary

layer thermodynamic and dynamic structure. While it is possible that a small systematic high bias is present in all simulated observations, this difference in PBL schemes should be taken into consideration when evaluating low level wind results. Furthermore, it is not clear if such a high wind speed bias would present itself when compared to real-world observations instead of a numerical model.

However, this should not take away from the benefits added to the forecast by the UAV observations within the first few hours of the forecast. Not only did the addition of UAV observations help reduce surface RMSE during this time (Fig. 3.23), but they also contributed to the production of better analysis and forecast of the boundary layer (Figs. 3.28, 3.33), especially pertaining to boundary layer moisture. This better analysis and forecast in moisture and low-level theta-e helped create better analyses and subsequent forecasts of most unstable and mixed layer CAPE and CIN. The improved CI observed in the UAV forecasts is likely due to this improvement in the low level thermodynamic fields. Similar sensitivities between low level moisture and convective initiation have been observed in other mesoscale OSSEs such as Gasperoni et al. (2013). This asserts the idea that for CI forecasting purposes, frequent and accurate sampling of boundary layer moisture and temperature is critical.

While some of the best results were observed in the 3 km UAV experiment in the form of better wind speed, boundary layer moisture and structure analyses, it can be argued that the results from the 1-, 2-, and 3-km experiments show no significant differences in the convective initiation forecast. Surface RMSE values already demonstrate that the height of the UAV flight plays a secondary role in the surface analysis and short-term forecast, and both most unstable and mixed layer CAPE fields

were identical for the three higher UAV flight analyses and forecasts. These results indicate that while some skill is gained by the addition of 400 ft. of UAV observations, there is a considerable improvement in the CI forecast by adding at least 1 km of UAV observations.

4.1.2 Network Density Summary

One of the most important network configuration considerations is network density. In this work four different network densities were examined with 75, 50, 25, and 10 UAV observation sites (with station spacing of roughly 56, 70, 106, and 199 km respectively) with UAV flights up to 1 km AGL. Since the 1 km MFA test incorporated 110 UAV observing sites, it is used as a fifth network configuration for comparison purposes. In short, all UAV network density experiments were able to forecast CI by at least 1930 UTC (up to half an hour prior to the No UAV experiment). However, it is noted that much of this convection, especially for the 75, 50, and 25-station network tests, is much weaker than the 110-station network. Interestingly, the 10-station network experiment showed strong convection by 1900 UTC, though this is considered an unrealistic result due to a high bias in low level moisture as compared to the Nature Run.

The stronger convection associated with the 10-station experiment is not overly surprising given the higher moisture values. As mentioned, Gasperoni et al. 2013 noted sensitivity associated between low level moisture analyses and forecasts and convective initiation. Weisman et al. (2008), Schwartz et al. (2010), and Jankov and Gallus (2005) all mention strong sensitivities between the initial conditions and convective initiation with the WRF-ARW model. So not only did the excess moisture in the lowest 1 km MSL increase MUCAPE and MLCAPE, it is likely the culprit behind the stronger and earlier

convection. The reason why the excess moisture was placed in the 10-station network analysis but is not apparent in the other analyses is not as clear.

One possible explanation is that this moisture represents the accumulation of forecast errors during the 6-hour assimilation cycling process. In their investigation of the impact of simulated observation errors on OSSE analysis errors, Prive et al. (2013) concluded that many of the errors in the analysis were the summation of both model errors and small observational errors that were propagated through the forecast. The observation errors added during each cycle of the data assimilation process are likely small. Hence, it is possible that one or more stations in the 10-station network introduced small amounts of excess moisture during the data assimilation cycling, particularly during the 1700 UTC analysis, that were not filtered out due to the lack of nearby UAV observations and the high weight applied to UAV observations relative to the other observing networks. Under higher-density networks, or with different correlation lengths used in ADAS, these observations may be effectively filtered out.

Another possible explanation is that this extra moisture is a side effect of forcing by the GFS lateral boundary conditions. Since the 10-station network has fewer observations as input it is more susceptible to boundary condition influences. However, if this were the case then the addition of moisture should be noted in the WRF Control and No UAV forecasts as well. Looking at Figures 3.51, 3.52, and 3.53 show a slight increase in low level moisture during the 1800 to 2000 UTC time frame. While this is not as strong of a signal as in the 10-station network experiment, it may be a secondary contributing factor.

Regardless, the observation errors associated with both the proposed UAV network and the simulated current network as well as the ADAS correlation lengths may need further calibration for different network configurations to ensure realistic results are obtained. Despite this uncertainty, a general trend is noted that similar analyses and forecasts were produced by the 75, 50, and 25-station networks. Although the 110-station networks give the best boundary layer analysis and short-term forecast, the results presented here suggest that even a 25-station network might be able to provide some benefit to boundary layer analyses and short term convective forecasts. However, the impact of individual UAV stations may need to be considered here as all network density experiments contained a UAV site in south central Oklahoma (see Figs. 3.42) that may have allowed for both PBL moisture/theta-e cross sections as well as MU/MLCAPE fields that compared so well to the Nature Run by extending the higher CAPE values further south and east. It is not clear if the removal of this UAV station would allow for similar results to be presented and suggests analysis and forecast sensitivity to the placement of the UAV sites.

4.1.3 General Conclusions

The findings in the MFA and network density experiments both suggest that the addition of a network of in-situ observations taken by autonomous CopterSonde UAVs could provide benefits to both boundary layer analyses as well as short term convective forecasts. While these observations would likely not have a large impact on surface analyses, the real value would be obtained by sampling the low to mid-levels of the PBL. The sensitivity of the CI forecast on boundary layer moisture suggests that future

CopterSonde development should focus on high quality observations of boundary layer moisture.

Although these results appear promising for the use of UAV technology in numerical weather prediction, a few caveats must be considered. The first is the dependency of the results on the convective environment. This study does not investigate the impacts of UAV observations on different convective regimes and scenarios such as high CAPE/low shear environments or when dealing with a linear squall line rather than discrete convection. This is particularly true for elevated convective environments in which boundary layer processes below 1 km may or may not play as significant a role. Additionally, the fact that any significant convective forecasting skill is lost after the first few hours when comparing UAV vs. No UAV forecasts may be a deterrent for those seeking longer duration benefits. Secondly, the sensitivity of this OSSE system to both observation and background errors, different parameterization schemes, and various sources for lateral boundary conditions is relatively unknown. Previous studies employing the WRF-ARW have noted these sensitivities (Jankov and Gallus (2005), Weisman et al. (2008), Schwartz et al. (2010), Cohen et al. (2015)), and the results found here suggest that such sensitivities may be impacting the forecasts, especially the network density forecasts. Additional sensitivities have been noted between the MYNN boundary layer scheme used in this study, the height of the WRF model top, and convective initiation (E. Fedorovich, personal communication, June 22, 2018). Finally, a calibration OSE has not yet been performed for this study to determine if the results of this OSSE system produce realistic results.

4.2 Future Work

Much of the future work possible with this research is focused around the caveats mentioned above. Perhaps the most beneficial addition to this research is to perform a calibration OSE. This OSSE has been set up with this calibration step in mind by simulating observations from the Oklahoma Mesonet. This way, real Mesonet observations can be used in the calibration OSE and the results can be easily compared to check for OSSE validity. By verifying that the results and conclusions presented here are reasonable and realistic, researchers can have higher confidence that a real 3-D Mesonet network would yield similar results operationally.

Sensitivity studies of this OSSE system should also be conducted to gain confidence in the results presented here. As mentioned, it is unknown weather similar results will be obtained under different convective regimes and storm modes and using different configurations of physical parameterizations, lateral boundary condition inputs, and observation/background errors. Along with iteratively changing WRF configuration settings, sensitivity testing could also be performed by using the WRF-ARW to create the Nature Run, followed by OSSE experiments performed with the ARPS model. Ideally, similar impacts should be noted between this alternate OSSE design and the current configuration presented here.

Further testing of the 3-D Mesonet network can be performed with this OSSE. Beneficial information may be found by testing the impacts of CopterSonde flight frequency on the analysis and subsequent CI forecast. By identifying the optimal number of flights prior to CI, the real-world 3-D Mesonet may be able to save long term costs by reducing the wear-and-tear on hardware through a reduced number of flights.

Additionally, testing various configurations and placements of observing stations may reveal optimal placement of UAV site. For example, performing an experiment with UAV observation sites around the border of the domain in a “picket fence” arrangement may allow for an improved forecast by accurately capturing low level waves or plumes of moisture as they enter the domain. The station-density experiments could also be replicated using more appropriate correlation length scales during the data analysis step for the lower density networks. This will investigate if better analyses can be created using lower density networks such as the 25 or 10 station networks than what were found here. Additionally, tests can be performed to investigate how well the 3-D Mesonet and the CopterSonde can capture other meteorological phenomenon such as the nocturnal low level jet.

Future work will also investigate the impact of noise in the ARPS Nature Run on the simulated observations and, subsequently, the WRF analyses and forecasts. As mentioned in sections 3.8.2.2 and 3.8.2.4, errors in the surface fields and low-level moisture fields may be artificially introduced by sampling noise from the Nature Run itself. Real atmospheric noise and variations are already accounted for in the simulated observation production by inserting artificial instrumentation and representativeness errors so sampling noise from the Nature Run may be creating worse analyses than expected. It is possible to gauge the impact of this noise-sampling issue by performing an OSSE experiment that assumes “perfect observations” and does not add any additional error to the sampled observations. This way, the amount of noise introduced by sampling the Nature Run can be assessed. If the 10 station experiment is performed again and the excessive moisture bias remains present, then it can be inferred that inappropriate

sampling of the Nature Run may be causing the effect. Different numerical sampling methods of the Nature Run may help produce not only improved simulated observations, but more realistic analyses and forecasts as well.

Similarly, sensitivity tests should be performed to gauge the impacts of different magnitudes of observation errors assigned to the UAV observations. While previous OSSE studies have focused on this topic on a global scale (Prive et al. 2013), this OSSE set up may exhibit heightened sensitivity due to the high resolution of the models used and the known sensitivities of moisture on correct convective initiation forecasting. Identifying the allowable error limits may also influence future design and operation of the CopterSonde by setting observing error guidelines and goals.

Despite these caveats, the results from this OSSE indicate that a network of UAVs does have the potential to improve short-term numerical boundary layer structure and convective initiation forecasts. Although additional research is needed, this opens the door for further OSSE work with mesoscale in-situ observing networks but also widens the possible applications of UAV technology in the field of atmospheric science.

References

Aksoy, A., S. Lorsolo, T. Vukicevic, K. J. Sellwood, S. D. Aberson, and F. Zhang, 2012: The HWRF hurricane ensemble data assimilation system (HEDAS) for high-resolution data: the impact of airborne doppler radar observations in an OSSE. Mon. Wea. Rev., 140, 1843–1862

Arbizu-Barrena, C., Pozo-Vazquez, D., Ruiz-Arias, J., Tovar-Pescador, J., 2015: Macroscopic cloud properties in the WRF NWP model: an assessment using sky camera and ceilometer data. Journ. Geophy. Research: Atmospheres 120, 19, 10297-10311

Arnold, C., Dey, C. H., 1986: Observing-systems simulation experiments: past, present, and future. Bull. Amer. Meteor. Soc. 67, 678 - 695. (June 1986)

Atlas, R., Bloom, S. C., 1989: Global surface wind vectors resulting from the assimilation of satellite wind speed data in atmospheric general circulation models. Oceans 89 Proceedings, IEEE Publication 89CH2780-5 260-265

Atlas, R., E. Kalnay, J. Susskind, D. Reuter, W. E. Baker, M. Halem 1984: Simulation studies of the impact of advanced observing systems on numerical weather prediction, conference on satellite/remote sensing and applications, pp. 283–287 Am. Meteorol. Soc.

Atlas, R., Kalnay, E., Halem, M., 1985: Impact of satellite temperature sounding and wind data on numerical weather prediction. Optical Engineering 24(2). 341 - 346. (March/April 1985)

Atlas, R., 1997: Atmospheric observations and experiments to assess their usefulness in data assimilation. J. Met. Soc. Japan, 75, 111-130

Atlas, R., et al., 2015: Observing system simulation experiments (OSSEs) to evaluate the potential impact of an optical autocovariance wind lidar (OAWL) on numerical weather prediction, *J. Atmos. Oceanic Technol*, DOI:10.1175/JTECH-D-15-0038.1_ 2015

Bloom, S., Takacs, L., Da Silva, A., and Ledvina D., 1996: Data assimilation using incremental analysis updates. Mon. Wea. Rev. 124, 1256-1271

Bonin, T., Chilson, P., Zielke, B., Fedorovich, E., 2013a: Observations of the early evening boundary-layer transition using a small unmanned aerial system. Bound. Lay. Met. 146. 119-132, 2013

Bonin, T., Chilson, P., Zielke, B., Klein, P., Leeman, J., 2013b: Comparison and application of wind retrieval algorithms for small unmanned aerial systems. Geosci. Instrum. Data Syst. 2, 177-187, 2013

Bratseth, A. M., 1986: Statistical interpolation by means of successive corrections. Tellus A, 38A: 439-447. doi:10.1111/j.1600-0870.1986.tb00476.x

Brewster, K., 2002: Recent advances in the diabetic initialization of a non-hydrostatic numerical model. Preprints, 21st conference on severe and local storms and preprints 15th conference on numerical weather prediction and 19th conference on weather analysis and forecasting. San Antonio, TX, Amer. Met. Soc. 51-54

Brewster, K., 2003a: ADAS/ARPS Data assimilation using incremental analysis updating. [Available online at http://www.caps.ou.edu/ARPS/ARPS5DOC/ADASNudging.pdf]

Brewster, K., 2003b: Phase-correcting data assimilation and application to storm-scale numerical weather prediction. part II: application to a severe storm outbreak. Mon. Wea. Rev., 131, 493-507

Brewster, K., Carr, F., Stratman, T., 2015: Utilizing heterogenous radar systems in a real time high resolution analysis and short-term forecast system in the Dallas/Fort Worth testbed. 37th Conference on Radar Meteorology, Norman, OK.

Bristor, C. L., 1958: Effect of data coverage on the accuracy of 500mb forecasts. Mon. Wea. Rev., 86, 299-308

Brock, F., Crawford, K., Elliot, R., Cuperus, G., Stadler, S., Johnson, H., Eilts, M., 1995: The oklahoma mesonet: a technical overview. Jour. Atmos. And Ocean. Tech. 12, 5 - 19

Bruscantini, C., Grings, F., Perna, P., Karszenbaum, H., Crow, W., Jacobo, J. 2012: An observing system simulation (OSSE) for the aquarius/SAC-D soil moisture product. 12th Specialist Meeting on Microwave Radiometry and Remote Sensing of the Environment, IEEE, DOI: 10.1109/MicroRad.2012.6185237

Cane, M., Cardone, V., Halem, M., Halberstam, I., 1981: On the sensitivity of numerical weather prediction to remotely sensed marine surface wind data: a simulation study. J. Geophys. Res., 86, 8093-8106.

Case, J., Blottman, P., Hoeth, B., and Oram, T., 2006: An operational configuration of the ARPS data analysis system to initialize WRF in the NWS environmental modeling system. 2006 National Weather Association Meeting, Report Number KSC-2006-093

Charney, J., Halem, M., Jastrow, R., 1969: Use of incomplete historical data to infer the present state of the atmosphere. J. Atmos. Sci. 26, 1160 - 1163

Chilson, P., Gleason, A., and Coauthors 2009: SMARTSonde: A small UAS platform to support radar research 34th AMS Conf. on Radar Meteor. 12B.6

Chou, M., 1990: Parameterization for the absorption of solar radiation by O2 and CO2 with application to climate studies. Journ. Climate, 3, 209-217

Chou, M., 1992: A solar radiation model for climate studies. Journ. Atmos. Sci., 49, 762-772

Chou, M., Suarez, M., 1994: An efficient thermal infrared radiation parameterization for use in general circulation models, NASA Tech Memo 104606, 85pp.

Cohen, A., Cavallo, S., Coniglio, M., Brooks, H., 2015: A review of planetary boundary layer parameterization schemes and their sensitivity in simulating southeastern U.S. cold season severe weather environments, Wea. Forecasting, 30, 591 - 611

Dabberdt, W., Schlatter, T., Carr, F., and Coauthors 2005: Multifunctioning mesoscale observing networks. Bull. Amer. Meteor. Soc. 86 (7), 961-982

Dawson, I., Daniel, T., and Xue, M., 2006: Numerical forecasts of the 15-16 June 2002 southern plains mesoscale convective system: impact of mesoscale data and cloud analysis. Mon. Wea. Rev., 134, 1607-1629

Deardorff, J.W. 1980: Stratocumulus-capped mixed layers derived from a three-dimensional model boundary-Layer Met. 18, 495

Dias, N., Goncalves, J., Freire, L., et al. 2012: Obtaining potential virtual temperature profiles, entrainment fluxes, and spectra from mini unmanned aerial vehicle data. Boundary Layer Meteor, 145:93. https://doi.org/10.1007/s10546-011-9693-2

Dudhia, J. :1989: Numerical study of convection observed during the winter monsoon experiment using a mesoscale two-dimensional model. J. Atmos. Sci., 46, 3077 - 3107

Duthoit, S., et al., 2017: A new approach for in-situ antenna characterization, radome inspection and radar calibration, using an unmanned aircraft system (UAS), 2017 IEEE Radar Conference (RadarConf), Seattle, WA, 2017, pp. 0669-0674. doi: 10.1109/RADAR.2017.7944287

Elston, J., Argrow, B., Stachura, M., and Coauthors, 2015: Overview of small fixed-wing unmanned aircraft for meteorological sampling. Jour. of Atmos. And Ocean. Tech. 32. 97-115. 10.1175/JTECH-D-13

Emmitt, G. D. and S. A. Woods 1991: Simulating thin cirrus clouds in observing system simulation experiments (OSSE) for LAWS proc. AMS Seventh Symp. on Meteorol. Observa. and Instru., Special Session on Laser Atmospheric Studies, New Orleans, LA, January 14-18, 460-462

Federal Aviation Administration, 2005: Unmanned aircraft systems (UAS) systems operations in the U.S. national airspace system (NAS) – interim operational approval guidance, AFS-400 FAA Memorandum, Sept. 16, 2005

Federal Aviation Administration, 2016: FAA sUAS part 107: the small UAS rule, Unmanned Aircraft Systems, https://www.faa.gov/uas/media/faa-uas-part107-flyer.pdf, accessed June 17, 2018

Fedorovich, E., 2018: Interview by A. Moore, personal communication, University of Oklahoma, Norman, OK

Gao, J., Xue, M., Brewster, K., Droegemeier, K., 2004: A three-dimensional variation data analysis method with recursive filter for doppler radars. Jour. Atmos. Oceanic Tech. 21, 457-469

Gasperoni, N., Xue, M., et al. 2013: Sensitivity of convective initiation prediction to near-surface moisture when assimilating radar refractivity: impact tests using OSSEs. JTECH, 30, 2281-2302 (October 2013)

Geerts, B., and Coauthors, 2017: The 2015 plains elevated convection at night field project. Bul. Amer. Met. Soc. https://doi.org/10.1175/BAMS-D-15-00257.1

Guest, P., 2014: Quantifying the accuracy of a quad-rotor unmanned aerial vehicle as a platform for atmospheric pressure, temperature, and humidity measurements near the surface. Amer. Geophys. Union. Fall 2014 Abstract No. OS41A-1180

Halem, M., and Dlouhy, R., 1984: Observing system simulation experiments related to space-borne lidar wind profiling. Part 1: Forecast impact of highly idealized observing systems. Preprints, Conference on Satellite Meteorology/Remote Sensing and Applications, June 25-29, 1984, Amer. Met. Soc. Clearwater, FL, 272-279

Halem, M., and Jastrow, R., 1970: Analysis of GARP data requirements. J. Atmos. Sci., 27, 177

Hartung, D., Otkin, J., Petersen, R., Turner, D., Feltz, W., 2011: Assimilation of surface-based boundary layer profiler observations during a cool-season weather event using an observing system simulation experiment. Part 2: Forecast assessment. Mon. Wea. Rev. 139, 2327 - 2346

Hoffman, R., Grassotti, C., Isaacs, R., Louis, J. F., Nehrkorn, T., 1990: Assessment of the impact of simulated satellite lidar wind and retrieved 183 GHz water vapor observations on a global data assimilation system. Mon. Wea. Rev., 118, 2513 - 2542. (December 1990)

Hoffman, R., 1993: A preliminary study of the impact of the ERS-1 C band scatterometer wind data on the european centre for medium-range weather forecasts global data assimilation system. JGR, 98

Hong, S., Noh, Y., Duhia, J., 2006: A new vertical diffusion package with an explicit treatment of entrainment processes. Mon. Wea. Rev., 134, 2318 - 2341

Intermet Systems, iMet-XF: Atmospheric sensor package for UAS integration, www.intermetsystems.com/ee/pdf/202010_iMet-XF_161005.pdf, accessed January 25, 2018

Jankov, I., and Gallus, W., 2005: Influence of initial conditions on the WRF-ARW model QPF response to physical parametrization changes, Wea. Forecasting, 22, 501 - 519

Janjic, Z., 1994: The step-mountain eta coordinate model: Further developments of the convection, viscous sublayer, and turbulence closure schemes. Mon. Wea. Rev., 122, 927 - 945

Jastrow, R., Halem, M., 1970: Simulation studies relating to GARP. Bull. Amer. Met. Soc. 51, 940-513

Jastrow, R., Halem, M., 1973: Accuracy and coverage of temperature data retrieved from the IR radiometer on the NOAA 2 satellite. J. Atmos. Sci., 30, 958-963

Jones, T., Otkin, J., Stensrud, D., Knopfmeier, K., 2013: Assimilation of satellite infrared radiances and doppler radar observations during a cool season observing system simulation experiment. Mon. Wea. Rev., 141, 3273 - 3299. (October 2013)

Klemp, J., Wilhelmson, R., 1978: The simulation of three-dimensional convective storm dynamics. Jour. Atmos. Sci. 35, 1070-1096

Koch, S., Chilson, P., Argrow, B., 2017: EPIC calibration/validation experiment field campaign report. DOE/SC-ARM-17-012, March 2017

Kuo, Y., Shumanich M., Haagenson, P., Chang, J., 1985: The accuracy of trajectory models as revealed by the observing system simulation experiments. Mon. Wea. Rev., 113, 1852 - 1867 (November 1985)

Leidner, S., Nehrkorn, T., Henderson, J., Mountain, M., Yunck, T., Hoffman, R., 2016: A severe weather quick observing system simulation experiment (QuickOSSE) of global navigation satellite system (GNSS) radio occultation (RO) superconstellations. Mon. Wea. Rev. 145, 638-651

Lin, Y., Farley, R., Orville, H., 1983: Bulk parameterization of the snow sield in a cloud model. Journal of Climate and Applied Meteorology, 22, 1065 - 1092 (June 1983)

Liu, C., Xiao, Q., Wang, B., 2009: An ensemble-based four-dimensional variational data assimilation scheme Part 2: Observing system simulation experiments with advanced research WRF (ARW). Mon. Wea. Rev., 137, 1687 - 1704 (May 2009)

Lord, S., Masutani, M., Woollen, J., Kapoor, V., 2001: Observing system simulation experiments for NPOESS. 81st AMS Annual Meeting IOS5

Masutani, M., Woollen, J., et al. 2010: Observing system simulation experiments at the national centers for environmental prediction. Journal of Geophysical Research, 115, D07101 (April 2010)

McPherson, R., Fiebrich, C., Crawford, K., Kilby, J., Grimsley, D., Martinez, J., Basara, J., Illston, B., Morris, D., Kloesel, K., Melvin., A., Shrivastava, H., Wolfinbarger, J., Bostic, J., Demko, D., 2006: Statewide monitoring of the mesoscale environment: A technical update on the Oklhoma Mesonet. J. Atmos. Oceanic Technol., 24, 301 - 321

Milbrandt, J. A. and M. K. Yau 2005: A multi-moment bulk microphysics parameterization. Part I: Analysis of the role of the spectral shape parameter. J. Atmos. Sci., 62, 3051-3064.

Miller, T. L., and Coauthors, 2008: Simulation of the impact of new aircraft and space-based ocean surface wind measurements on H*Wind analyses. 12th Conf. on Integrated Observing and Assimilation Systems for the Atmosphere, Oceans, and Land Surface (IOAS-AOLS), New Orleans, LA, Amer. Meteor. Soc., P1.6.

Mlawer, E., Steven, J., Taubman, J., Brown, P., Iacono, M., Clough, S., 1997: Radiative transfer for inhomogeneous atmospheres: RRTM, a validated correlated-k model for the longwave. J. Geophys. Res., 102, 16663 - 16682

Moeng, C., 1984: A large-eddy-simulation model for the study of planetary boundary layer turbulence. Jour. Atmos. Sci. 41, 2052-2062

Nakanishi, M. and H., Niino, 2006 An improved Mellor–Yamada level-3 model: Its numerical stability and application to a regional prediction of advection fog. Bound.-Layer Meteor., 119, 397–407

National Centers for Environmental Prediction/National Weather Service/NOAA/U.S. Department of Commerce, 2000: NCEP FNL operational model global tropospheric analyses, continuing from July 1999, https://doi.org/10.5065/D6M043C6, Research Data Archive at the National Center for Atmospheric Research, Computational and Information Systems Laboratory, Boulder, Colo. (Updated daily.) (Accessed June 10, 2018).

National Research Council. 2009: Observing weather and climate from the ground up: A nationwide network of networks. Washington, DC: The National Academies Press. https://doi.org/10.17226/12540

Newton, C. W., 1954: Analysis and data problems in relation to numerical prediction. Bull. Amer. Meteor. Soc. 35, 287-294

Nolan, D. S., R. Atlas, K. T. Bhatia, and L. R. Bucci, 2013: Development and validation of a hurricane nature run using the joint OSSE nature run and the WRF model. J. Adv. Model. Earth Syst., 5, 382–405

Oklahoma Mesonet. "Instruments: air temperature and related measurements" mesonet.org, https://www.mesonet.org/index.php/site/about/air_temperature_and_related_measurements (accessed June 10, 2018)

Peng, G., 2014: What's the difference netween GFS and FNL?, NCAR Atmospheric and Geoscience Research Data Archive, 5 Dec. 2014, (accessed Jan. 20, 2018)

Prive, N., Errico, R., Tai, K., 2013: The influence of observation errors on analysis error and forecast skill investigated with an observing system simulation experiment, Jour. of Geophysical Research: Atmos., 118, 11

Rohaly, G. D., Krishnamurti, T. N., 1993: An observing system simulation experiment for the laser atmospheric wind sounder (LAWS). Mon. Wea. Rev., 32, 1453 - 1471. (January 1993)

Schwartz, C., Kain, J., Weiss, S., Xue, M., Bright, D., Kong, F., Thomas, K., Levit, J., Coniglio, M., and Wandishin, M., 2010: Toward improved convection-allowing ensembes: Model physics sensitivities and optimizing probabilistic guidance with small ensemble membership, Wea. Forecasting, 25, 263-280

Shen, R., Reiter, E., and Bresch, J., 1986: Vertical interpolation of meteorological variables. Mon. Wea. Rev., 114, 123-133

Skamarock, W., Klemp, J., Duhia, J., Gill, D., Barker, D., Wang, W., Powers, J., 2005: A description of the advanced research WRF Version 2. NCAR Technical Note

Smith, S., Chilson, P., Houston, A., Jacob, J., 2017: Catalyzing collaboration for multi-disciplinary UAS development with a flight campaign focused on meteorology and atmospheric physics. AIAA Sci. Tech. Forum January 2017

Stalker, J., Lasley, J., Frederick, G., McPherson, R., Campbell, P., Phillips, B., Pasken, B., 2013: A nationwide network of networks. Bul. Amer. Met. Soc. 1602-1605, October 2013

Sun, W., Chang, C., 1986: Diffusion model for a convective layer Part 1: Numerical simulation of convective boundary layer. Jour. of Climate and App. Meteor. 25, 1445 - 1453

Thompson, G., Field, P., Rasmussen, R., Hall, W., 2008: Explicit forecasts of winter precipitation using an improved bulk microphysics scheme. Part 2: Implementation of a new snow parameterization. Monthly Weather Review, 136, 5095 - 5115

Tong, M., Xue, M., 2004: Ensemble kalman filter assimilation of doppler radar data with a compressible nonhydrostatic model: OSS experiments. Mon. Wea. Rev., 133, 1789 - 1807

Vaisala, 2013: Vaisala radiosonde RS92-SGP, www.vaisala.com, https://www.vaisala.com/sites/default/files/documents/RS92SGP-Datasheet-B210358EN-F-LOW.pdf (accessed June 10, 2018)

Villa, Tommaso Francesco and coauthors, 2016: An overview of small unmanned aerial vehicles for air quality measurements: Present applications and future prospectives. Ed. Assefa M. Melesse. *Sensors (Basel, Switzerland)* 16.7 (2016): 1072. *PMC*. Web. 10 Jan. 2018.

Wainwright, C., Bonin, T., Chilson, P., Gibbs, J., Fedorovich, E., Palmer, R., 2015: Methods for evaluating the temperature structure-function parameter using unmanned aerial systems and large-eddy simulation. Boundary-Layer Meteorology 155, 189-208

Wang, X., Barker, D., Snyder, C., Hamill, T., 2008: A hybrid ETKF-3DVAR assimilation scheme for the WRF model. Part 1: Observing system simulation experiment. Mon. Wea. Rev., 136, 5116-5131, (December 2008)

Walker, M., Miller, D., 2013: Effects of tether on rotor UAS flight. 9th Conf. on Field and Service Robotics

Watson, L., 2010: ADAS update and maintainability. NASA Technical Note, NASA/CR-2010-216290

Weisman, M., Davis, C., Wang, W., Manning, K., Klemp, J., 2008: Experiences with 0-36h explicit convective forecasts with the WRF-ARW model, Wea. Forecasting, 23, 407-437

Weiss, S., Pyle, M., Janjic, Zavisa, Bright, David, Kain, S., John, DiMego, J., Geoffrey, 2008: The operational high-resolution window WRF model runs at NCEP: Advantages of multiple model runs for severe convective weather forecasting, Preprints, 24th Conf. on Severe Local Storms, Savannah, GA, Amer. Meteor. Soc., P10.8 [Available online at: https://ams.confex.com/ams/24SLS/techprogram/paper_142192.html]

Williamson, D., 1973: The effects of forecast error accumulation on four-dimensional data assimilation. J. Atmos. Sci., 30, 537-543.

Williamson, D., Kasahara, A., 1971: Adaptation of meteorological variables forced by updating. J. Atmos. Sci. 28, 1313 - 1324.

Woods, S. A., G. D. Emmitt, and L. S. Wood, 1991: Global three-dimensional distribution of LAWS observations based upon aerosols, water vapor and clouds. Optical Remote Sensing of the Atmosphere, Fifth Topical Meeting, Williamsburg, VA, November 18-21

Xue, M., Droegemeier, K., Wong, V., 2000a: The advanced regional prediction system (ARPS) - A multi-scale nonhydrostatic atmospheric simulation and prediction model. Part 1: model dynamics and verification. Meteor. And Atmos. Physics, 75, 161-193

Xue, M., Droegemeier, K., Wong, V., Shapiro, A., Brewster, K., Carr, F., Weber, D., Liu, Y., Wang, D., 2000b: The advanced regional prediction system (ARPS) - A multi-scale nonhydrostatic atmospheric simulation and prediction tool. Part 2: Model physics and applications. Meteor. And Atmos. Physics, 76, 143 - 165

Xue, M., Tong, M., Droegemeier, K., 2005 An OSSE framework based on ensemble square root kalman filter for evaluating the impact of data from radar networks on thunderstorm analysis and forecasting. JTECH, 23, 46-66 (January 2006)

Yussouf, N., Stensrud, D., 2010: Impact of phased-array radar observations over a short assimilation period: Observing system simulation experiments using an ensemble kalman filter. Mon. Wea. Rev., 138, 517 - 538, (February 2010)

Zack, J., Natenberg, E. J., Knowe, G. V., Waight, K., Manobianco, J., Hanley, D., Kamath C., 2011: Observing system simulation experiments (OSSEs) for the mid-columbia basin. Lawrenece Livermore National Laboratory (September 2014)

Zhang, J., Carr, F., Brewster, K., 1998: ADAS cloud analysis. Preprints 12th conference on numerical weather prediction, Phoenix, AZ. Amer. Met. Soc. Boston 185-188

Zhang, L., and Z. Pu, 2010: An observing system simulation experiment (OSSE) to assess the impact of doppler wind lidar (DWL) measurements on the numerical simulation of a tropical cyclone. Adv. Meteor., 2010, 743863

Zhang, Y., Dong, T., Liu, Y., 2017: Design of meteorological element detection platform for atmospheric boundary layer based on UAV. Inter. Jour. of Aero. Engin. 2017, Article ID 1831676

Zhao, K., and Xue, M., 2009: Assimilation of coastal doppler radar data with the ARPS3DVAR and cloud analysis for the prediction of hurricane Ike. Geophys. Res. Lett., 36, (12)

Appendix

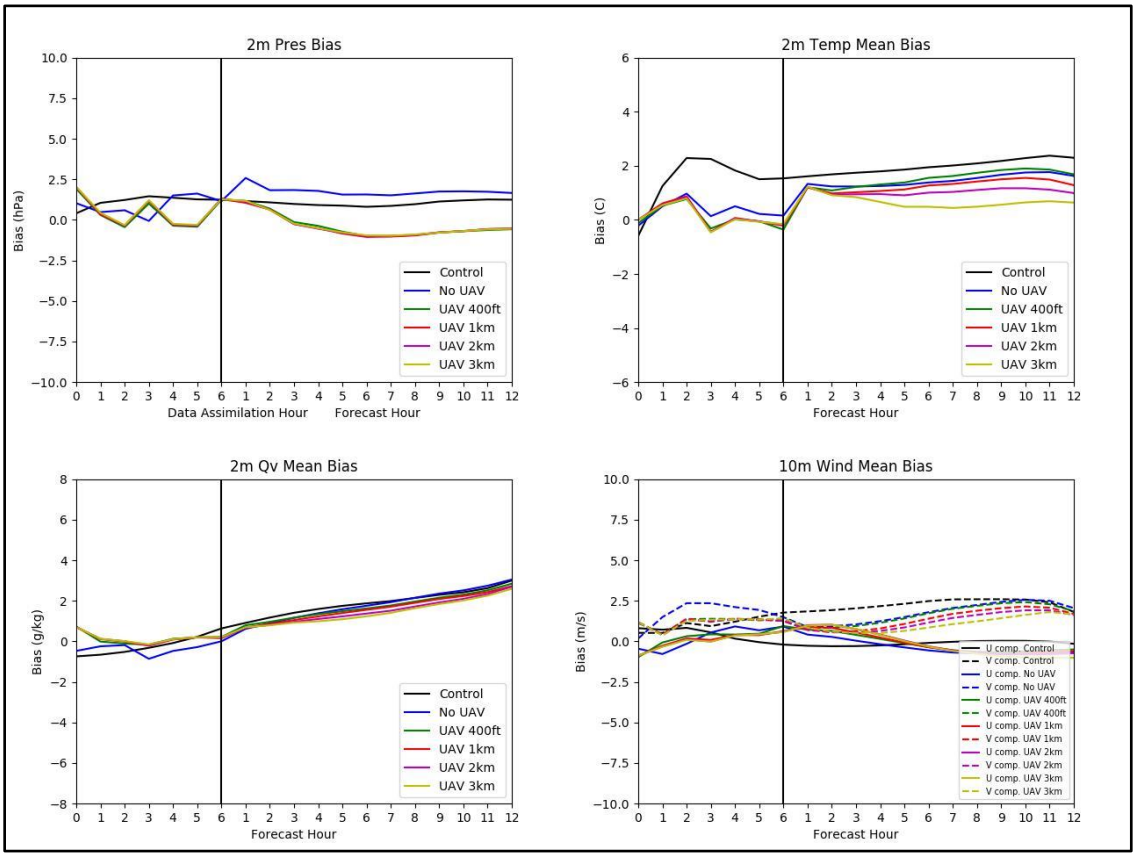

Figure A.1: Mean bias plots during the data assimilation cycling period (left of the vertical black line) and during the free forecast period (right of the black line) for surface pressure (upper left), 10 m U and V winds (upper right), 2 m mixing ratio (bottom left), and 2 m temperature (bottom right).

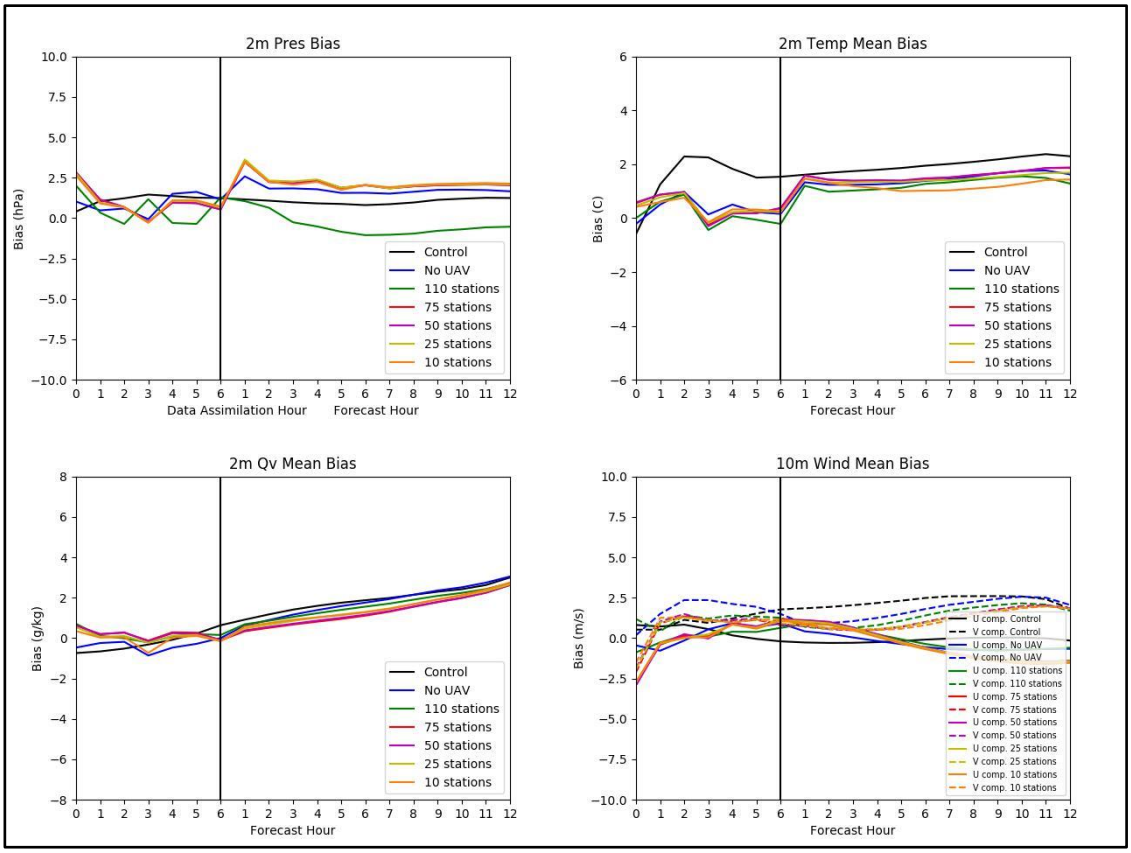

Figure A.2: Mean bias plots during the data assimilation cycling period (left of the vertical black line) and during the free forecast period (right of the black line) for surface pressure (upper left), 10 m U and V winds (upper right), 2 m mixing ratio (bottom left), and 2 m temperature (bottom right).